

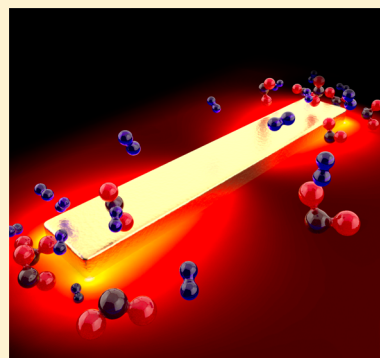
## Surface-Enhanced Infrared Spectroscopy Using Resonant Nanoantennas

Frank Neubrech,<sup>\*,†,‡</sup> Christian Huck,<sup>‡</sup> Ksenia Weber,<sup>†</sup> Annemarie Pucci,<sup>‡</sup> and Harald Giessen<sup>†</sup>

<sup>†</sup>4th Physics Institute and Research Center SCoPE, University of Stuttgart, Pfaffenwaldring 57, Stuttgart 70569, Germany

<sup>‡</sup>Kirchhoff Institute for Physics, Heidelberg University, Im Neuenheimer Feld 227, Heidelberg 69120, Germany

**ABSTRACT:** Infrared spectroscopy is a powerful tool widely used in research and industry for a label-free and unambiguous identification of molecular species. Inconveniently, its application to spectroscopic analysis of minute amounts of materials, for example, in sensing applications, is hampered by the low infrared absorption cross-sections. Surface-enhanced infrared spectroscopy using resonant metal nanoantennas, or short “resonant SEIRA”, overcomes this limitation. Resonantly excited, such metal nanostructures feature collective oscillations of electrons (plasmons), providing huge electromagnetic fields on the nanometer scale. Infrared vibrations of molecules located in these fields are enhanced by orders of magnitude enabling a spectroscopic characterization with unprecedented sensitivity. In this Review, we introduce the concept of resonant SEIRA and discuss the underlying physics, particularly, the resonant coupling between molecular and antenna excitations as well as the spatial extent of the enhancement and its scaling with frequency. On the basis of these fundamentals, different routes to maximize the SEIRA enhancement are reviewed including the choice of nanostructures geometries, arrangements, and materials. Furthermore, first applications such as the detection of proteins, the monitoring of dynamic processes, and hyperspectral infrared chemical imaging are discussed, demonstrating the sensitivity and broad applicability of resonant SEIRA.



### CONTENTS

1. Introduction	5111
2. Nonresonant Surface-Enhanced Infrared Absorption	5112
2.1. Electromagnetic Effect	5112
2.2. Chemical Effect	5113
3. Fundamentals of Resonant SEIRA	5114
3.1. Resonant Infrared Nanoantennas	5114
3.2. Experimental Observation	5115
3.3. Theory and Modeling	5116
3.3.1. Fano-Formalism	5116
3.3.2. Coupled Harmonic Oscillators	5117
3.3.3. Temporal Coupled Mode Theory	5117
3.3.4. Numerical Calculations	5118
3.4. Vibrational Signal Enhancement	5118
3.4.1. Spectral Tuning	5118
3.4.2. Spatial Extent and Scaling with Plasmonic Near-Field Enhancement	5119
3.4.3. Sensitivity	5119
3.4.4. Wavelength Scaling	5121
4. Optimization of Vibrational Signal Enhancement	5121
4.1. Geometrical Properties	5121
4.1.1. Nanoantenna Shape	5121
4.1.2. Antennas Supported by Metal Films	5122
4.1.3. Antennas on Pedestals	5123
4.1.4. Babinet's Principle: Nanoslits	5123
4.2. Material Properties	5124
4.3. Nanoscopic Properties	5125

4.4. Interaction between Resonant Nanoantennas	5126
4.4.1. Near-Field Interaction	5126
4.4.2. Far-Field Interaction	5126
4.5. Broadband Signal Enhancement	5127
4.5.1. Dual- and Multiband Nanostructures	5127
4.5.2. Post-Fabrication Tuning	5128
4.6. Pushing the Detection Limit	5129
4.6.1. Brilliant Light of Advanced Light Sources	5129
4.6.2. Scattering Near-Field Optical Microscopy	5130
5. From SEIRA to Strong Coupling: Phonon Polaritons	5131
6. Applications of Resonant SEIRA	5132
6.1. Assessing Plasmonic Near-Fields	5132
6.1.1. Nanometer-Scale	5133
6.1.2. Ångström-Scale	5133
6.1.3. 3D Mapping of Buried Nanostructures	5133
6.2. Hyperspectral Infrared Chemical Imaging	5133
6.3. Sensing of Proteins	5135
6.3.1. Detection of Proteins	5135
6.3.2. Fano-Resonant Asymmetric Metamaterials	5136

### Special Issue: Vibrational Nanoscopy

Received: November 3, 2016

Published: March 30, 2017

6.3.3. In Situ Monitoring of Protein Binding Dynamics	5137
6.4. Real-Time Monitoring of Lipid Membranes	5137
7. Conclusion and Outlook	5138
Author Information	5139
Corresponding Author	5139
ORCID	5139
Notes	5139
Biographies	5139
Acknowledgments	5139
References	5139

## 1. INTRODUCTION

Infrared (IR) fingerprint vibrations contain valuable molecular information because the vibrational properties are directly linked to the molecular constituents, their chemical bonds, as well as their configuration.<sup>1</sup> Consequently, an unambiguous, nondestructive, and label-free detection of substances is possible (see Figure 1a), making infrared spectroscopy a

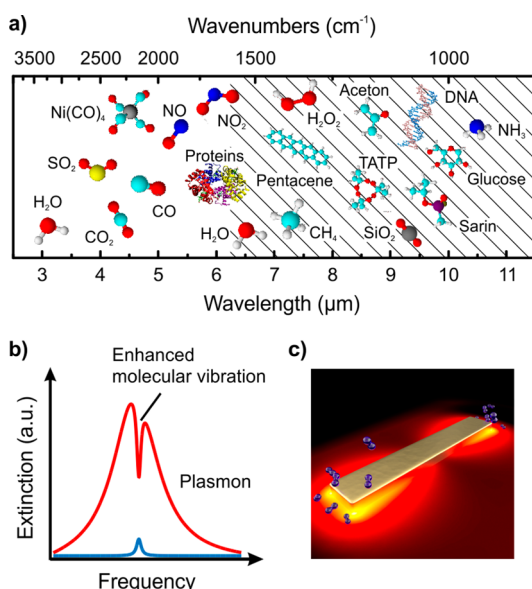


**Figure 1.** (a) Characteristic infrared vibrations of selected molecular species. The fingerprint region containing skeletal vibrations is hatched. (b,c) Principle of resonant surface-enhanced infrared spectroscopy (SEIRA): Infrared vibrations of molecules located in the enhanced electromagnetic near-field of a plasmonic nanostructure (nanoantenna) are enhanced if the plasmon (red) is resonantly matched to the molecular vibration (blue).

powerful and indispensable tool. Particularly, Fourier transform infrared (FTIR) spectroscopy is widely used in various fields of research, in industry, and in other applications for fast and routine structural investigations of chemical compounds, monitoring of processes, and identification of substances.<sup>1,2</sup>

In basic research, for instance, transport properties in organic electronic devices are characterized,<sup>3</sup> or small dust particles and samples from meteorites are identified.<sup>4</sup> Applied to process monitoring, pollutants are detected, or components in industrial production processes are inspected for defects.<sup>2</sup> Moreover, infrared spectroscopy is routinely applied in health, pharmacy, safety, food, and forensic sciences to identify substances.<sup>1</sup> It is possible to identify counterfeit paintings<sup>5</sup> or to discriminate between healthy tissue sections and tumors,

employing infrared chemical imaging.<sup>6</sup> Additionally, structural information can be obtained, for example, on conformational states of proteins, which is of paramount importance for biological and medical applications.<sup>7</sup>

However, due to the low molecular absorption cross-sections of mid-infrared vibrations ( $\sigma_{\text{abs}} \approx 10^{-20} \text{ cm}^2$ ), a considerably large amount of material is needed. Consequently, a spectroscopic characterization of minute amounts of analytes, as required for sensing applications, is hampered. One possibility to overcome this limitation is the use of collective electronic oscillations at surfaces of metal nanostructures (nanoantennas). Such localized surface plasmon polariton resonances (LSPRs), often called particle plasmon resonances, strongly depend on the nanostructures' geometry and material but can also be understood as propagating surface plasmon polaritons (SPPs).<sup>8,9</sup> On the nanometer scale, the resonant excitation is accompanied by highly confined and enhanced electromagnetic near-fields, which nowadays are commonly used to enhance light–matter interaction, for example, in surface-enhanced Raman scattering (SERS),<sup>10</sup> enhanced fluorescence,<sup>11</sup> or surface-enhanced infrared absorption (SEIRA).

Already in 1980, Hartstein et al. applied this concept to infrared spectroscopy, which was later named surface-enhanced infrared absorption.<sup>12–14</sup> Employing a thin film of randomly arranged Ag nanoparticles with plasmonic resonances located in the visible spectral range (not resonantly tuned to the infrared vibrations), he found that the infrared vibrations of a molecular film beneath the nanoparticles were enhanced by a factor of 20. A significantly stronger enhancement by approximately 5 orders of magnitude is obtained if especially sharp LSPRs or particle plasmons (sometimes termed antenna resonances in the IR and THz region) are resonantly tuned to the respective infrared vibration (see Figure 1b). In contrast to the very broad excitation spectra of random metallic nanostructure ensembles as, for example, metal-island layers, sharp plasmonic resonances need certain prerequisites that we will explain later. This approach of SEIRA based on sharp plasmonic resonances for which we introduce the term “resonant” SEIRA was first demonstrated by Neubrech et al. in 2008 and enabled the detection of approximately 50 attograms of analytes located in the plasmonic hot-spots of a single nanoantenna (see Figure 1c).<sup>15</sup> In the following years, numerous studies were dedicated to the fundamental processes underlying resonant SEIRA as well as the optimization of the signal enhancement. Furthermore, advanced preparation techniques of metal nanostructures, enabling the fabrication of homogeneous SEIRA substrates on large areas at low costs for routine applications, were developed. Beyond the detection and characterization of molecular substances with unprecedented sensitivity, numerous applications of resonant SEIRA were demonstrated, for example, hyperspectral infrared chemical imaging<sup>16,17</sup> probing plasmonic near-fields,<sup>18–20</sup> or monitoring of dynamical processes.<sup>21,22</sup> Whereas this Review mainly focuses on the mid-IR spectral range, the presented concept is also applicable to other wavelength ranges, for example, the THz spectral range.<sup>23–25</sup>

The main objective of this Review is to provide a profound understanding of the physics underlying resonant SEIRA and to discuss early applications. First, a short historical perspective of SEIRA with large areas of more or less random arrangements of metallic particles is given. Because of the very broad plasmonic absorption, the importance of resonance tuning for SEIRA

enhancement is low, and so we will use the term “nonresonant” SEIRA also in relation to earlier work that was intended to exploit plasmonic resonances but could not clarify a benefit.<sup>26–31</sup> Further information about this topic, including biological applications, can be found, for example, in ref 32. In the following section, the prerequisites for resonant SEIRA as well as its fundamental properties of this approach including details on the resonant coupling mechanism and the signal enhancement are discussed. With this background, different ways to optimize the signal enhancement are presented ranging from the design of nanostructures to postfabricational tuning. As discussed in the subsequent section, also strong coupling of molecular and plasmonic excitations may occur if phononic excitations are enhanced. The potential of resonant SEIRA for applications is discussed in the last section of this Review.

## 2. NONRESONANT SURFACE-ENHANCED INFRARED ABSORPTION

Only three years after the discovery of surface-enhanced Raman scattering,<sup>33,34</sup> SEIRA with rough metal island films was identified.<sup>12</sup> Interestingly, a kind of SEIRA of gas molecules on small metal particles was already measured as the so-called anomalous transmittance in experiments much earlier, but had not been put into context with the plasmonic behavior of metal films originating from their granular morphology.<sup>35</sup> In fact, the optical properties of molecules adsorbed on metal island films, but also on continuous metal films with various degrees of roughness, are dramatically changed, leading to effects such as SEIRA. SEIRA was found to be strongly dependent on the metal surface morphology that is the result of specific preparation conditions, such as substrate temperature, deposition rate, substrate material, and surface morphology.<sup>36–42</sup> Enhancement factors, defined as the ratio of enhanced vibrational signal and an unenhanced reference measurement (see section 3.4), of 1–3 orders of magnitude have been reported often in the literature.<sup>12,37,38,41,43</sup> Furthermore, the SEIRA effect has been observed on island films of the noble metals but also on other metals, such as Pt,<sup>44</sup> Sn,<sup>32</sup> Ru,<sup>45,46</sup> Pd,<sup>38</sup> and Fe.<sup>47,48</sup> Similar to surface-enhanced Raman scattering, at least two different mechanisms are supposed to contribute to the total SEIRA enhancement,<sup>14,49</sup> that is, an electromagnetic effect (plasmonic effect, related to the free-electron optical response and its near-field) and a chemical effect (related to charge transfer upon adsorption, which has consequences for the frequencies and infrared activity of molecular vibrations).

### 2.1. Electromagnetic Effect

In the infrared, below the onset of interband transitions, the optical properties of metals are determined by collective oscillations of free charge carriers. These plasmonic oscillations give rise to the high metallic reflection up to the plasma edge,<sup>50</sup> because electromagnetic waves with frequencies below the plasma edge are attenuated inside the metal. However, surface-plasmon polaritons as mixed excitations of plasmonic and photonic nature can also exist in the IR range.<sup>51,52</sup> The SPPs consist of a plasmonic excitation within the penetration depth of a few tens of nanometers in the metal and of an electromagnetic near-field that exponentially decays with the distance from the metal surface.<sup>8</sup> Vibrational dipoles of molecules located inside the near-field might show enhanced vibrational signals because plasmonic excitations are accompanied by enhanced near-fields. This near-field enhancement is

larger the closer the frequency is to the resonance and can be further increased by a kind of lightning rod effect that occurs at sharp apexes.<sup>31</sup> Thinking in terms of IR absorption, SEIRA enhancement is proportional to the ratio of the near-field intensity to the intensity of the external (or average) field.<sup>53</sup>

Usually, the plasmonic response of a material with free charge carriers can be reasonably described by the Drude dielectric function with only two parameters (plasma frequency and relaxation rate of free charge carriers).<sup>54,55</sup> For almost all metals, the dielectric function has a very strong negative real part in the IR. Especially in the mid-IR, for most metals the absolute value of the real part is larger than that of the imaginary part, which describes electronic damping of plasmonic excitations. For such low electronic damping, it seems to be surprising that metal films consisting of small particles interact with IR light, because small metal particles are known to have resonances in the visible range. Indeed, individual particles with a geometrical aspect ratio of the order of one have their plasmonic resonances in the visible range.<sup>8</sup> The resonance position shifts to lower frequencies if the particles have other aspect ratios, for example, are very flat or are very elongated, respectively (see section 3.1). Yet also almost spherical particles can have resonances in the infrared due to the interaction with other particles in a layer.

For randomly grown island films, the distribution of particle size and distance broadens the infrared spectrum significantly; thus it looks like a smooth background in infrared transmittance.<sup>56–59</sup> The slope of that background is determined by the density of the particles and changes its sign at the percolation threshold; see Figure 2.

This optical behavior can be exploited for contact-free measurement of electrical percolation, for example. However, very close to the percolation threshold, distances between metal islands are extremely small,<sup>56,60</sup> which is beneficial for near-field enhancement and consequently for the enhancement of the

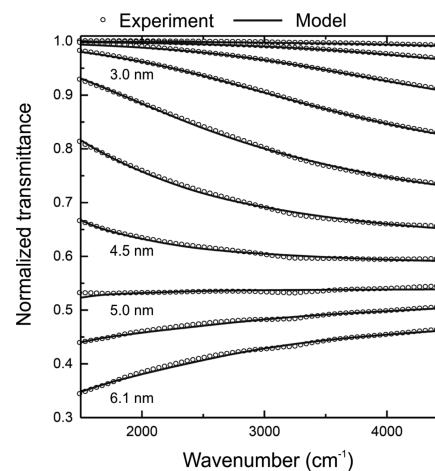


**Figure 2.** IR transmittance at normal incidence of light for copper films grown on MgO(111) at 300 K under ultrahigh vacuum conditions. The spectra are shown for various average thicknesses as indicated for steps of about 0.5 nm (open symbols). The model spectra (solid lines) were obtained with the two-dimensional Bruggeman model for a mixture of vacuum and copper for which the electron scattering was adjusted for surface scattering. The free parameter for the spectral fits was the filling factor. The transmittance is normalized to that of the bare substrate before deposition. Percolation is observed at about 5 nm where the filling factor of the fit is 50%.

molecular vibrations. The normal-incidence IR transmittance at percolation is nearly frequency independent, which can be attributed to a balancing overlap of two contributions, one from separate islands and the second one from the fully coalesced area.<sup>61</sup> Because of the random nature of the metal island film, the local field enhancement spatially varies on the layer in relation to morphology.<sup>62</sup> Interestingly, the signal enhancement appears already for metal island layers that have only absorption tails in the infrared and the main absorption in the near-infrared.<sup>53</sup> Figure 3 shows such a case for carbon monoxide

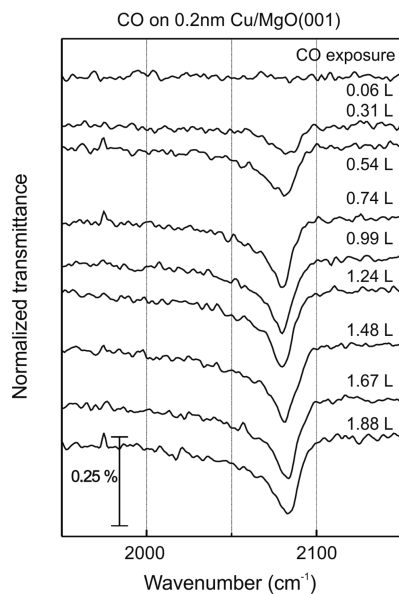


**Figure 3.** IR transmittance at normal incidence of light for carbon monoxide (CO) adsorbed on a copper island film with an average thickness of only 0.2 nm. The transmittance is normalized to that of the bare copper film before deposition. The copper film has been grown at 300 K (see Figure 2), but the CO exposure (at  $2 \times 10^{-8}$  mbar and given in Langmuir  $L = 1$  Torr  $\mu\text{m}$ ) is done at 100 K. At 100 K, CO adsorbs only in the first layer on Cu and not on MgO(001). The CO signals correspond to the C–O stretching vibration of CO on Cu(111) facets and show a signal enhancement of about 10. Nevertheless, the copper islands do not show infrared absorption as can be concluded from Figure 2.

(CO) adsorbed on copper islands grown on magnesium oxide (MgO(001)). Because metal-island films can be produced much easier and cheaper than by nanolithographic methods, they are still interesting structures for surface-enhanced vibrational spectroscopy even though the vibrational signal enhancement is small as compared to resonant SEIRA.

Especially for a strong SEIRA enhancement, the vibrational line shape looks asymmetric.<sup>44</sup> First attempts to explain nonresonant SEIRA spectra including the line shape and frequency of the molecular vibration as well as the plasmonic part with the Maxwell–Garnett effective medium approach failed.<sup>49</sup> Later, it turned out that the packing density of metal islands in SEIRA-active layers is too large to be described by this model. However, the Bergman theory (as the more elaborated approach<sup>44</sup>) and the Bruggeman approach (as the easiest description valid for small particles and packing densities close to the percolation threshold) give a qualitative explanation of the observed line shape.<sup>47</sup> With the Bruggeman model, it was shown that the largest SEIRA signal is obtained at the percolation threshold and that electronic damping should

be as low as possible for high SEIRA signals.<sup>47</sup> In this study, a mixture of a metal dielectric function with a Lorentzian vibrational oscillator was used to model the experimental results. This kind of mixture corresponds to the coupling between the vibrational and plasmonic dipoles, which can be interpreted in analogy to Fano-type interaction (see section 3.3). So, there is not only the influence of the plasmonic excitation on the vibrational one (i.e., the SEIRA enhancement proportional to the near-field intensity), there is also the feedback of the vibrational excitation on the plasmonic one, which becomes important for plasmonically resonant objects that not only absorb radiation but also scatter it in a similar amount<sup>63</sup> (see section 3.3.4). In all kinds of SEIRA, the coupling is mediated by the plasmonic near-field and increases with the near-field strength. This is corroborated also by experiments with dense packing of particles.<sup>64</sup> The dense packing also means small gaps in which the near-field is especially enhanced.<sup>53</sup>

A very interesting controlled approach to SEIRA-active substrates is the application of dense two-dimensional hexagonal arrays of identical particles, for example, core–shell spheres, whose resonance is governed by the shell thickness and particle diameter.<sup>65,66</sup> As the next more sophisticated structure, nanoparticles, with metal shells and a nonmetal core, with a nonlinear optical material coating have been introduced recently. With such engineered nanoparticles, nonlinear process can be selectively supported, for example, the generation of the difference-frequency in the infrared, as shown in ref 67. Further developments based on artificial hybrid nanostructures with metallic components have been suggested as tunable infrared absorbers.<sup>68</sup>

Nonresonant SEIRA spectra usually are measured in transmittance geometry on a transparent substrate or as attenuated total reflectance (ATR) with the metal particles on the ATR prism. The ATR geometry is beneficial for sensing, especially if multiple reflections are realized.<sup>69,70</sup> This method has been successfully applied to biomolecular sensing and monitoring molecular reactions on a microsecond time scale.<sup>71</sup> Using a tailored functionalization, sensing via SEIRA of the vibrations of a certain atomic group in a catcher molecule becomes even more specific so that molecular changes due to pollution can be detected.<sup>72</sup>

For certain applications, for instance, in bioscience, a well-defined and perfect functionalization of the metal surface is desired. Unfortunately, metal roughness hampers the formation of such ordered layers of functional molecules, potentially leading to a loss of their functional properties. A small roughness may be beneficial even though the SEIRA enhancement is low as compared to rougher surfaces and an especially high photometric accuracy is needed. The success of this approach utilizing high-quality and smooth gold surfaces has been demonstrated in various studies, for example, in studies of interactions of membrane proteins that have been immobilized on a strongly reflecting gold surface via self-assembled monolayers.<sup>70</sup>

## 2.2. Chemical Effect

On smooth metal surfaces, the chemical effect might enhance infrared vibrational signals. For example, it is known that molecules adsorbed on an electrode surface change their infrared response with the applied voltage, which allows for monitoring chemical reactions in relation to the applied potential.<sup>13,73,74</sup> Furthermore, a chemical effect is also observed

on metal surfaces that are smooth on the micrometer scale, but rough on the atomic scale. By comparing ethylene adsorbed at low temperature on copper films with different surface roughnesses, chemical enhancement of almost infrared inactive modes was demonstrated.<sup>75</sup> Also, on layers consisting of nanoparticles with a sufficient surface roughness (meaning the existence of atomic steps and high-index surface orientations), a chemical enhancement of certain vibrational modes of molecules directly adsorbed on the metal was observed additionally to the electromagnetic enhancement.<sup>47,76–78</sup> Both the electromagnetic and the chemical enhancement change the vibrational line shape, but in contrast to the electromagnetic effect in SEIRA, the chemical enhancement concerns only selected vibrational modes. For these modes, the coupling between vibrational and electron–hole pair excitations is not negligible.<sup>79–81</sup> Because chemical effects are unwanted in studies in which precise information on the number of molecules is searched for, functionalized surfaces could be beneficial to suppress coupling between electron–hole pairs and vibrational excitations of the target molecules. In this respect, approaches utilizing layers of metal nanoparticles that have been produced with a functionalizing shell before arranging them in a certain pattern are promising also for SEIRA applications. Furthermore, such approaches provide the additional benefit to arrange nanoparticles in an ordered pattern in a plane or on curved surfaces of larger particles, which allows for tuning of the plasmonic spectrum.<sup>82</sup>

### 3. FUNDAMENTALS OF RESONANT SEIRA

In the following section, the prerequisite for resonant SEIRA, the underlying physics, and the key parameters for applications will be discussed.

#### 3.1. Resonant Infrared Nanoantennas

Resonant surface-enhanced infrared spectroscopy benefits from confined electromagnetic near-fields of tailored nanostructures. For the preparation of such structures, a variety of nanofabrication methods are available including electron beam lithography (EBL),<sup>83</sup> direct laser writing (DLW),<sup>84</sup> colloidal hole mask lithography,<sup>85</sup> interference lithography,<sup>86</sup> nanostencil lithography,<sup>87,88</sup> chemical preparation methods,<sup>89,90</sup> nanosphere lithography,<sup>91–93</sup> photolithography,<sup>94</sup> as well as combinations of these methods.<sup>95</sup> In many studies, simple linear nanorods with micrometer lengths and nanometer cross-sectional geometries are used as model systems. Such linear antennas feature pronounced plasmonic resonances in the infrared spectral region caused by collective oscillations of electrons.<sup>90,96</sup> Please note that the terms plasmonic resonance and antenna resonance (or combinations of it) are used synonymously within this Review. In our opinion, it is not necessary to distinguish between them for our nanostructures with resonances in the infrared. Both terms describe the identical physical phenomena, which is a mixed state of collective electronic excitations and photons localized at a metallic surface (localized or propagating surface plasmon polariton). The term plasmonic emphasizes the electronic nature, while the term antenna represents the photonic one. In the infrared, the antenna-like resonances along the symmetry axis with length  $L$  can be considered as a standing wave phenomenon in analogy to radio frequency (RF) antennas. However, the main difference is the nonzero penetration depth of the electromagnetic radiation into the material, resulting in a compressed effective wavelength as compared to the wave-

length of external infrared radiation as explained by Novotny.<sup>97</sup> For a half-wave dipole antenna, the resonance frequency is then given by

$$\lambda = \frac{2L}{m}na_1 + a_2 \quad (1)$$

where  $m$  is the mode number and  $n$  is the refractive index of the surrounding medium. The constant  $a_2$  accounts for the phase associated with the reflection at the antenna end, and the parameter  $a_1$  depends on the antennas geometry and its material. Both parameters become more important for smaller nanoparticles with resonances in the near-infrared and visible spectral region.<sup>97,98</sup> In these spectral regions, electronic damping within the metal caused by optical absorption in the metal dominates over radiation damping, and retardation becomes less important. In the mid-IR, however, both damping mechanisms significantly influence the antenna resonances and require a careful design to achieve an optimum SEIRA enhancement.<sup>63</sup> Considering eq 1 again, the resonance wavelength scales linearly with antenna length  $L$  (see also Figure 4a) and the refractive index of the surrounding medium.

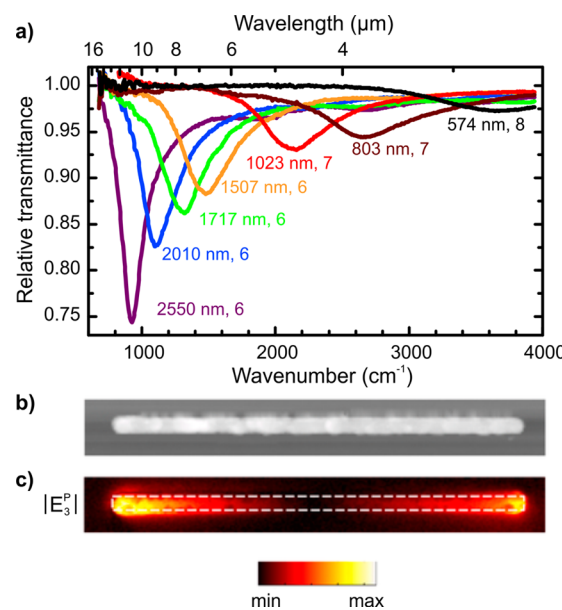


**Figure 4.** (a) Relative transmittance (parallel polarization) for nanowires ( $w = 58 \pm 10$  nm,  $h = 60$  nm as known from preparation, and 5  $\mu\text{m}$  wire–wire distance) with different  $L$  as given ( $\pm 73$  nm). Because all of the IR spectra were taken with an aperture of 16.67  $\mu\text{m}$  in diameter, a different number of nanowires (an approximate value is indicated together with the length  $L$ ) contribute to the IR signal for different  $L$ . Adapted from ref 99. Copyright 2008 AIP Publishing. Topography (b) and experimental s-SNOM images of a single Au nanoantenna obtained with p-polarized detection (c). Antenna length is 3.8  $\mu\text{m}$ . For details, see ref 100. Reprinted with kind permission from ref 100. Copyright 2015 Wiley-VCH Verlag GmbH & Co. KGaA.

Both effects need to be taken into account for an optimized design of tailored nanostructures for resonant SEIRA. Especially the dependence on the length offers a simple access to the nanofabrication of structures with desired resonance frequencies. In contrast, the change of the refractive index caused by adsorbed analyte is often difficult to predict, because it depends on the adsorbate itself and its layer thickness.<sup>83,101</sup> Hence, elaborated simulation approaches such as finite different

time domain (FDTD), finite element simulations, or boundary element methods<sup>102</sup> are required.

From the transmittance spectra in Figure 4a, the ratio of extinction cross-section and geometric cross-section can be calculated. Close to the fundamental resonance, it is much larger than 1, indicating the capability of plasmonic nanoantenna to harvest light.<sup>96</sup> On the nanometer scale, infrared scattering near-field optical microscopy (s-SNOM) reveals that the electromagnetic fields of such a resonantly excited nanoantenna are highly confined within a few tens of nanometers around the tip ends (Figure 4c).<sup>63,103,104</sup> Consequently, the near-fields are strongly enhanced as compared to the incident infrared radiation. Typical near-field enhancements, defined as the ratio of electromagnetic field with and without plasmonic structures, found in numerical simulations are of the order of 10–100 depending on the nanostructure.<sup>15,95</sup> As demonstrated in several studies, such enhancements significantly improve the light–matter interaction on the nanoscale. For example, electromagnetic near-fields have been applied to sensing applications such as refractive index sensing,<sup>105</sup> enhanced fluorescence,<sup>11</sup> SERS,<sup>10</sup> and resonant SEIRA. To achieve the maximum enhancement in these field-enhanced spectroscopic methods, detailed knowledge of the spectral dependence of the near-field is required. When comparing the maxima of the far-field extinction and near-field intensity, a slight spectral red shift is found for the near-field.<sup>104</sup> It results from damping and can be deduced from a driven harmonic oscillator model.<sup>106</sup> In addition to the fundamental resonance, higher order modes are observed in near- and far-field studies of nanoantennas.<sup>16,107</sup> For SEIRA applications, they are of minor interest due to their lower dipole moment and consequently lower field enhancement. A further increase of the field enhancement is obtained if interacting nanoparticles are used instead of single or noninteracting nanoantennas.<sup>100,103</sup> The impact of the interaction between nanoantennas on the SEIRA enhancement will be discussed in section 4.4.

### 3.2. Experimental Observation

In 2008, Neubrech et al. demonstrated the benefit of resonant nanostructures for surface-enhanced infrared absorption.<sup>15</sup> In their experiments, single gold nanostructures with different lengths were prepared by electrochemical deposition in etched ion-track membranes, transferred to an infrared transparent substrate, and covered with a 2.8 nm thick self-assembled monolayer of octadecanethiol (ODT) acting as a model analyte (see Figure 5a). ODT is an alkanethiol, which selectively chemisorbs on gold surfaces via a sulfur–gold binding and thus ensures a localization of the molecules in the confined and strongly enhanced electromagnetic near-fields of the nanostructures (see Figure 5b).

Relative transmittance spectra (transmittance measured at the position of the nanoantenna divided by the transmission of the bare substrate) were recorded with a diffraction-limited infrared microscope (IR microspectroscopy) connected to a synchrotron light source enabling SEIRA studies of single nanostructures. As seen in Figure 5c, the extinction spectra are dominated by the fundamental plasmonic excitations of the nanoantennas around  $3000\text{ cm}^{-1}$  if light polarized parallel to the long antenna axis is used ( $E_{\text{par}}$ ). According to eq 1, a shift of the plasmonic resonance is found with varying length. In addition to the broadband antenna resonance, narrowband spectral signatures appear at  $2855$  and  $2927\text{ cm}^{-1}$ , which are

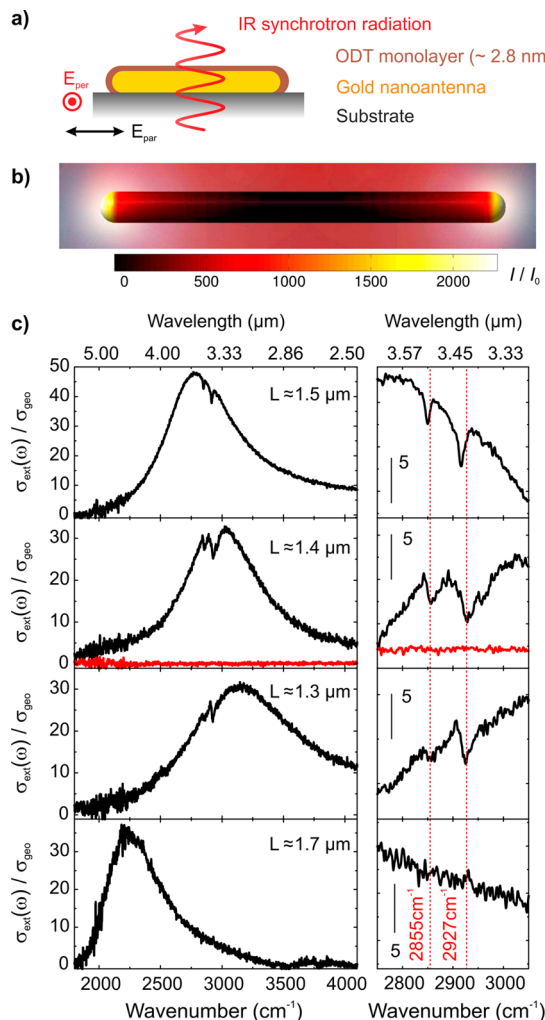


**Figure 5.** (a) Schematic drawing of the measurement geometry. (b) Calculation of the near-field intensity 1 nm above the surface of a gold nanowire (in vacuum,  $L = 1.31\text{ }\mu\text{m}$ , diameter  $D = 100\text{ nm}$ ) at the fundamental antenna resonance ( $\lambda_{\text{res}} = 3.41\text{ }\mu\text{m}$ ). The color scale (shading) indicates the magnitude of the enhancement. (c) Experimental extinction cross-sections  $\sigma_{\text{ext}}$  (normalized to the geometrical cross-section  $\sigma_{\text{geo}}$ ) for four octadecanethiol (ODT)-coated wires with different  $L$  as indicated and  $D = 100\text{ nm}$  on  $\text{CaF}_2$ . The electrical field is polarized parallel ( $E_{\text{par}}$ , black curves) and perpendicular ( $E_{\text{per}}$ , red lines) to the long antenna axis. The noise level slightly varied depending on the incoming IR intensity. The right panels display magnifications of the vibrational signals. Dotted lines: ODT vibration frequencies. Figure adapted with permission from ref 15. Copyright 2008 The American Physical Society.

assigned to symmetric and asymmetric  $\text{CH}_2$  vibrational modes of ODT. If perpendicularly polarized light ( $E_{\text{per}}$ ) is used, no plasmon is excited in the infrared spectral range, and no enhanced near-fields are present. Consequently, no enhanced vibrational bands are found, which clearly prove the enhancement effect by the plasmonic antennas (red line in second panel in Figure 5c). As further proof of principle, the plasmonic resonance frequency (defined as the frequency of maximum extinction or minimum transmittance) is varied with respect to the molecular vibrations. The strongest signal enhancement is observed close to the best match of the plasmonic and vibrational frequency. If the antenna is completely detuned (lower panel), no vibrational signals are observed, demonstrating the resonant nature of the enhancement effect. Moreover,

the line shapes of the enhanced vibrations clearly differ from Lorentzian absorptions bands and additionally change with tuning as a consequence of the phase-dependent electromagnetic interaction between both excitations. Depending whether the broadband plasmonic and narrowband molecular vibrations are matching or not, dips or asymmetric profiles are observed. This situation can be treated analogous to coupled harmonic oscillators with strongly differing widths<sup>108</sup> or the quantum mechanical interaction between a continuum and a discrete state (Fano-resonances),<sup>109,110</sup> both producing asymmetric line-shapes as discussed in section 3.3. The variation of enhancement and line-shape with tuning is in good agreement with full electromagnetic simulations (boundary element method) and clearly demonstrates the resonant nature of the SEIRA approach under consideration.

### 3.3. Theory and Modeling

The key to understanding the enhancement mechanism in resonant SEIRA is the interaction between plasmonic and molecular excitations, which require a model accounting for resonant coupling. Often, modified functional forms of Fano-resonances<sup>109–111</sup> or coupled harmonic oscillators<sup>108</sup> are used to derive an intuitive understanding or to fit experimental SEIRA spectra. From these fits, the individual properties of the molecular and the plasmonic excitation are extracted, but a detailed understanding of the coupling is not possible. Hence, more elaborated ab initio models are required, for example, a generalized Fano-formula including molecular losses.<sup>112</sup> Nevertheless, the model of coupled harmonic oscillators,<sup>108</sup> the temporal coupled mode theory (TCMT),<sup>22</sup> the analogy to Fano-resonances,<sup>109,110</sup> and a recently developed coupled point-dipole model<sup>113</sup> provide intuitive understanding of the processes underlying resonant SEIRA.

As a typical signature of resonant coupling, resonances with asymmetric line shapes are observed. In SEIRA studies, the narrowband asymmetric vibration profiles appear as modulations on the broadband plasmonic background as shown exemplarily in Figure 6a. In the corresponding experiments, nanoantenna arrays with different lengths were covered with a 5.4 nm thick layer of the organic molecule 4,4'-bis(*N*-carbazolyl)-1,1'-biphenyl (CBP) featuring several IR active vibrational bands in the fingerprint region (500–1500 cm<sup>−1</sup>).<sup>111</sup> In contrast to the studies described in section 3.2, the molecules were deposited from the gas phase, resulting in a homogeneous molecular layer, which covers the antennas as well as the bare substrate. Depending on the antenna length, plasmonic resonances with different resonance frequencies and enhanced molecular vibrations with different line shapes are found in the infrared spectra (Figure 6a). To characterize the impact of resonance position on the vibrational line shape, a baseline-correction was performed. Here, an adapted version of the asymmetric least-squares smoothing algorithm proposed by Eilers was applied to remove the plasmonic background.<sup>111,114</sup> As a result, enhanced molecular vibrations with asymmetric line shapes varying with tuning are obtained (see Figure 6b). Their origin will be discussed below.

**3.3.1. Fano-Formalism.** In another context, a quantum mechanical study of the autoionizing states of atoms, resonances with asymmetric line shapes were discovered by Ugo Fano in 1961.<sup>115</sup> In contrast to Lorentzian-type line shapes, Fano-resonances feature an asymmetric profile (Fano-profile) given by the following expression:

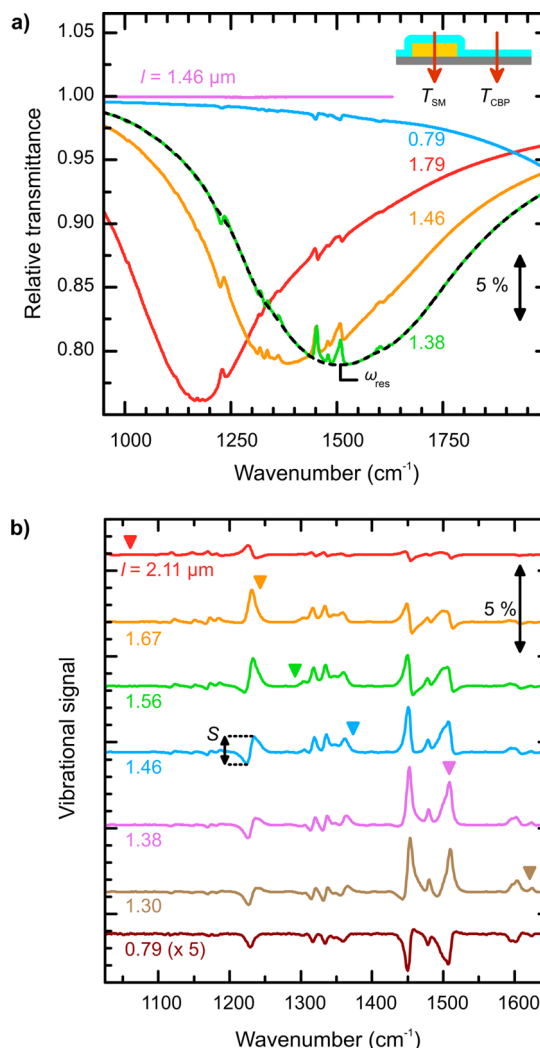


**Figure 6.** (a) Relative transmittance spectra  $T_{\text{rel}}$  of four selected nanoantenna arrays with different antenna length  $l$  (see legend) resonant in the fingerprint region of CBP. All arrays (sample positions  $T_{\text{SM}}$ ) and the background positions ( $T_{\text{CBP}}$ ) were covered with an evaporated 5.4 nm film of CBP. Thus, only enhanced signals appear in the relative transmission spectra  $T_{\text{rel}} = T_{\text{SM}}/T_{\text{CBP}}$ . The purple curve indicates perpendicular polarization, with respect to the long antenna axis. To extract the enhanced CBP vibrational signals, a baseline (dashed black curve) was determined iteratively with an adaption of an algorithm proposed by Eilers. The plasmonic far-field resonance frequency  $\omega_{\text{res}}$  is defined as the minimum of the baseline. (b) Baseline corrected relative transmittance spectra of selected nanoantenna arrays in the fingerprint spectral region of CBP. The plasmonic resonance positions  $\omega_{\text{res}}$  of respective antenna (length is given on the left) are marked with triangles. The signal strengths of the enhanced molecular vibrational modes are obtained as peak-to-peak value  $S$ , shown exemplarily in the figure. Both signal strength as well as line shape vary with the spectral position of the plasmonic resonance. The spectra are shifted, and the data for  $l = 0.79 \mu\text{m}$  are multiplied by 5 for better visibility. Adapted from ref 111 with permission. Copyright 2015 The PCCP Owner Societies.

$$I \propto \frac{(q\gamma + \omega - \omega_0)^2}{(\omega - \omega_0)^2 + \gamma^2} \quad (2)$$

where  $\omega_0$  is the resonance frequency,  $\gamma$  is the width of the resonance, and  $q$  is the Fano-parameter describing the asymmetry of the vibration. In a microscopic picture, the

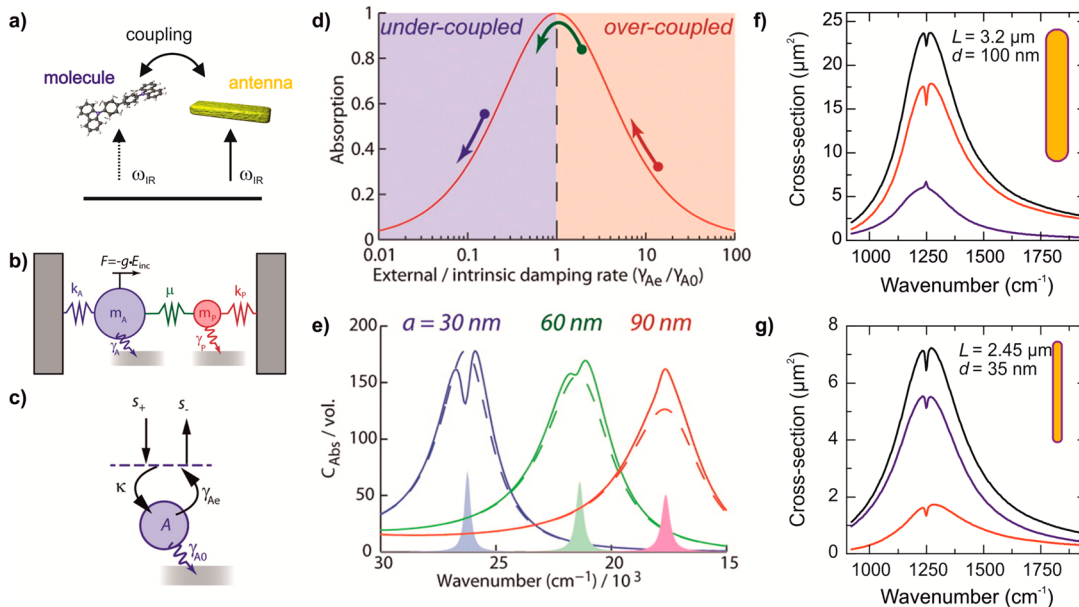


**Figure 7.** (a) Schematic illustration of excitation paths in Fano-resonances. Incident IR radiation with frequency  $\omega_{\text{IR}}$  excites a quasi-continuum state (plasmonic resonance). The discrete state (molecular vibration) is only weakly excited via IR light (dotted arrow) and driven by the coupling with the plasmonic state. (b) Traditional, damped harmonic oscillator conception of a coupled bright (A) and dark (P) mode. Mode A is driven by external radiation, via  $g \cdot E_{\text{inc}}$ , and experiences damping at a rate  $\gamma_A$ . Mode P is dark, and hence does not interact directly with external radiation or the driving field. Its damping rate,  $\gamma_P$ , is typically much smaller than  $\gamma_A$ . The two modes are coupled by some rate,  $\mu$ . (c) Schematic of generalized cavity model used in temporal coupling mode theory (without the absorber present). (d) Peak absorption for the generalized cavity shown in (c), as calculated from eq 3 evaluated at  $\omega = \omega_A$ , as a function of external to intrinsic damping rate. The colored arrows indicate the relevant movements along the curve for the three different ellipsoids in (e). (e) Critical coupling effects in scattering by an absorber-coated nanoparticle. Absorption cross-sections ( $C_{\text{abs}}$ , normalized to particle volume) for three different length (semiaxis  $a$ ) Ag prolate spheroidal particles (dashed curves). The solid curves show the same, but where the Ag particles are coated with a 5 nm thick shell of a model material exhibiting an absorption band aligned with the particle resonance (colored regions at the bottom of the panel). (f,g) Absorption (blue), scattering (red), and extinction cross-section (black) spectra of a dominantly absorbing antenna (g) and an antenna that dominantly scatters (f). The resonance frequency of the hosting antennas is kept at approximately  $1250 \text{ cm}^{-1}$ . (a) The sample is a dielectric layer homogeneously covering the antenna surface (thickness  $t = 10 \text{ nm}$ ). For more details, see ref 63. Adapted with permission from refs 118 and 63. Copyright 2013 American Chemical Society and 2015 American Chemical Society.

asymmetry arises from the constructive and destructive interference of two excitation pathways. In particular, one excitation path is a broad spectral line or continuum, and the other one a narrow or discrete resonance. However, because interference is a general wave phenomenon, Fano-resonances are not only found in quantum mechanical systems, but also in classical optics.<sup>116,117</sup>

In line with this, the concept of Fano-resonances can also be applied to resonant SEIRA. Here, the plasmonic excitation corresponds to the continuum or broad resonance and the discrete excitation or narrow resonance to the molecular vibration (see Figure 7a). Consequently, the asymmetric line shape of the vibrational signal results from constructive and destructive interference of the electromagnetic field from the plasmonic resonance and the spectrally much narrower field associated with the vibrational dipoles of the molecules.<sup>109,110</sup> Depending on the phase of the electromagnetic interaction, which is described by the parameter  $q$  in the Fano-model, different kinds of line shapes are observed as shown in Figure 6b for different vibrational bands of CBP. For a perfect match corresponding to an antiphase interaction, an antiabsorption (induced transmission) peak appears in the spectrum. As the antenna is detuned with respect to the vibrations, progressively decreasing vibrational signals with clearly asymmetric profiles are observed.

**3.3.2. Coupled Harmonic Oscillators.** From a classical point of view, the resonant coupling can also be understood in terms of two coupled harmonic oscillators (see Figure 7b),

which provide an intuitive description of the main features of Fano-resonances. Hence, the model was applied to describe numerous coupled systems and physical effects such as the classical analogues of electromagnetic induced transparency (EIT).<sup>116</sup> With respect to SEIRA,<sup>108</sup> the plasmonic mode is strongly driven by incident infrared light and therefore called “bright” mode. In contrast, the far-field radiation only weakly interacts with the molecular vibration due to the low molecular cross-section and is referred to as approximately “dark”. Enabled by the coupling (parameter  $\mu$  in Figure 7b) to the bright antenna mode, the molecular vibration can also be excited. Consequently, the vibration is not directly observed as an absorption feature in the spectrum, but appears as a modulation on top of the plasmonic resonance. Also, in this model, line-shapes ranging from antiabsorption to asymmetric Fano-profiles appear with dependence of resonance tuning.

**3.3.3. Temporal Coupled Mode Theory.** An important extension to the coupled oscillator model is the temporal coupled mode theory (TCMT).<sup>119–121</sup> It provides further insights into Fano-resonant systems and reveals important parameters for an optimized design of resonant nanostructures used for SEIRA as shown by Adato et al.<sup>108</sup> In particular, it illustrates how intrinsic (material absorption) and external losses (radiation) of plasmonic antennas influence the enhanced vibrational signals and their line-shapes in the absorption spectra. In the coupled mode theory, the response of a single cavity coupled to input and output traveling waves

( $s_+$  and  $s_-$ ) through one port is described by the coupled mode equations (see also Figure 7c):

$$\frac{dA}{dt} = j\omega_A A - (\gamma_{A0} + \gamma_{Ae})A + \kappa s_+ \quad (3)$$

and

$$s_- = -s_+ + \kappa A \quad (4)$$

Equation 3 describes the dynamic evolution of the amplitude  $A$  of the resonance ( $|A|^2$  is the energy stored in the system) and eq 4 the propagation of the traveling waves. In this expression, the driving term is given as  $\kappa A$  depending on the amplitude of the traveling wave  $A$  and the fraction  $\kappa$ , which is coupled into the resonant mode. The mode frequency is denoted as  $\omega_A$ , and the net sum of losses is given as  $\gamma$ . It consists of a nonradiative part  $\gamma_{A0}$  accounting for the intrinsic material losses and  $\gamma_{Ae}$  describing the external losses due to radiation into the far-field. In contrast to a driven harmonic oscillator, the driving term described by the rate  $\kappa$  is constrained and related to the damping rate. This is a consequence of the time reversal symmetry and energy conservation and one of the key features of TCMT.<sup>120–122</sup>

Using scattering theory, the absorption  $C_{\text{abs}}$  of the cavity can be calculated from the coupled mode equations:

$$C_{\text{abs}} = \frac{4\gamma_{A0}\gamma_{Ae}}{(\omega - \omega_A)^2 + (\gamma_{A0} + \gamma_{Ae})^2} \quad (5)$$

On resonance ( $\omega = \omega_A$ ), the absorption depends on the ratio of external to internal damping rates. It is maximum for  $\gamma_{A0} = \gamma_{Ae}$ , which is known as critical coupling, and smaller than 1 for the undercoupled ( $\gamma_{A0} > \gamma_{Ae}$ ) and overcoupled ( $\gamma_{A0} < \gamma_{Ae}$ ) regimes (see Figure 7d).

This behavior has an important impact if a second oscillator (e.g., a molecule) is added to the system (plasmonic resonance) as discussed by Adato et al.<sup>108</sup> The molecular vibration is not directly driven by the incident wave but coupled to the bright cavity mode. In the TCMT, the coupling of a weak infrared vibration can be thought of as adding an additional amount of damping to the internal plasmonic losses, which changes the ratio of external to internal damping rate. Applied to SEIRA, this coupling leads to different kinds of lineshapes, even though the tuning between the plasmonic and molecular resonance remains unchanged. Figure 7e illustrates this situation. Here, absorption spectra for coated and uncoated silver prolate spheroidal particles with different lengths are depicted. The plasmonic resonances are perfectly matched to the respective molecular vibrational bands, but show significantly different line shapes ranging from dips (EIT-like) to peaks (analogue of electromagnetic induced absorption, EIA)<sup>123</sup> depending on the ratio of external to internal losses. Also, intermediate line shapes with nearly vanishing signal enhancements are observed.

Consequently, a careful nanostructure design for an optimum SEIRA enhancement is required. In addition to the plasmonic near-field enhancement and spectral tuning, the ratio of external and internal losses needs to be considered. In the nanofabrication process, the radiative losses can be engineered via the particle geometries and the internal losses via the choice of different materials or material of different crystalline quality. Additionally, the optical properties of the adsorbed molecular species itself influence the ratio of damping rates, which is a minor effect for low loss molecular vibrations, but impacts the

design if spectrally broader vibrations, such as phonons, are enhanced.<sup>63</sup>

**3.3.4. Numerical Calculations.** Even though the above-mentioned results enable intuitive understanding and provide helpful design rules for loss engineering, the picture is still incomplete. So far, only absorption properties of the coupled system are discussed. In the infrared, however, also scattering significantly contributes to the plasmonic extinction, particularly for thicker antennas. Hence, to gain a full understanding, the scattering cross-section of the coupled molecular plasmonic system needs to be included. This has been done exemplarily for linear antennas in a numerical study by Neuman et al.<sup>100</sup> Utilizing the total field scattered field approach in FDTD simulations, the scattering, extinction, and absorption cross-sections of gold nanoantennas coated with an artificial molecule are numerically calculated. By changing the diameter of the nanoantenna, the radiative losses are changed, and consequently the ratio to the internal ones as well. This results in increased or decreased absorption cross-sections (see Figure 7f and g) at the molecular vibration in accordance with the TCMT. However, the molecular feature still appears as a dip in the scattering cross-section independent of the external loss (which is related to the nanoantenna diameter). For a certain diameter, this behavior may result in decreased vibrational signal strength in the extinction cross-section, which is the experimentally accessible quantity in SEIRA studies. As shown by more detailed simulations,<sup>63</sup> the best SEIRA performance is found for a ratio of scattering to absorption cross-section of approximately 1. Hence, the results again emphasize the need for a detailed engineering of external and internal losses of nanostructures for resonant SEIRA.

### 3.4. Vibrational Signal Enhancement

With respect to applications of resonant SEIRA, the enhancement of the molecular vibration is the key parameter because it defines the sensitivity. Following its definition, its spatial extent and its dependence on the spectral tuning with respect to the plasmonic resonance will be discussed. Furthermore, its scaling with wavelength and plasmonic near-field enhancement will be considered.

**3.4.1. Spectral Tuning.** Because of the resonant nature of the molecule–plasmon coupling, the enhanced vibrational signal strengths strongly depend on the plasmonic resonance frequency with respect to the vibrational one. This fact requires a tailored design of antenna resonances for an optimized SEIRA performance. To detail this behavior, an enhancement factor for each vibration shown in Figure 6 is estimated and plotted versus the tuning ratio  $\omega_{\text{vib}}/\omega_{\text{res}}$  in Figure 8.

The enhancement factor is calculated by normalizing the enhanced vibrational signal strength  $S$  to the respective nonenhanced vibration signal strength and the number of molecules actively contributing to the signal. The latter is discussed in detail in section 3.4.3. The tuning ratio  $\omega_{\text{vib}}/\omega_{\text{res}}$ , however, relates the plasmonic resonance frequency  $\omega_{\text{res}}$  (indicated by triangles in Figure 6b) to the respective vibrational frequency  $\omega_{\text{vib}}$ . A tuning ratio of 1 describes a perfect match of the far-field extinction maximum to the vibrational resonance; any other value smaller or larger than 1 indicates detuning. Interestingly, the highest enhancement is found at a ratio slightly smaller than 1 and not at exactly 1. This fact is in agreement with experimental and theoretical investigations where a spectral shift between near- and far-field response was observed and discussed in terms of a driven

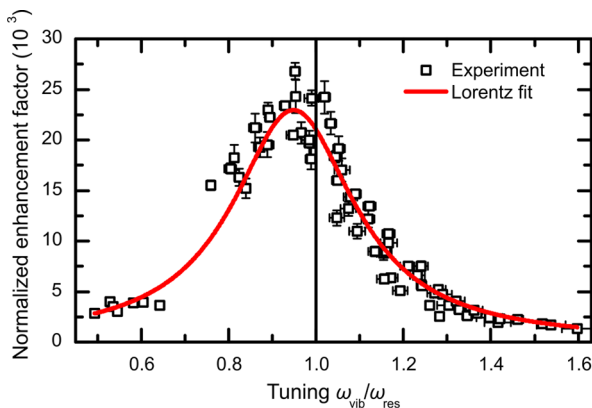


**Figure 8.** Normalized enhancement factor of the seven strongest modes of CBP in the considered spectral fingerprint range versus the ratio of molecular and plasmonic resonance frequencies  $\omega_{\text{vib}}/\omega_{\text{res}}$ . As a guide to the eye, a Lorentzian was fitted to the measured data (red curve). The vibrational signal enhancement peaks at  $\omega_{\text{vib}}/\omega_{\text{res}} = 0.95$  revealing a red shift of the maximum plasmonic near-field intensity with respect to the far-field antenna resonance ( $\omega_{\text{vib}}/\omega_{\text{res}} = 1$ , black line). Adapted from ref 111 with permission. Copyright 2015 The PCCP Owner Societies.

damped harmonic oscillator.<sup>104,106</sup> Because the probed molecules are located in the antennas near-fields and the vibrational signal enhancement scales with the near-field intensity,<sup>18</sup> a red shift of the enhancement with respect to the plasmonic far-field extinction is found. For the investigated configuration, a shift of  $50 \text{ cm}^{-1}$  is extracted, which increases if highly damped systems are used.<sup>104,106</sup> However, for SEIRA applications, the shift is of minor importance, particularly if broad vibrational absorptions are investigated, for example, amide vibrations of proteins with line widths of about  $50 \text{ cm}^{-1}$ . Hence, a good rule of thumb for most SEIRA applications is that the antenna resonance frequency should be matched to the molecular vibration of interest.

**3.4.2. Spatial Extent and Scaling with Plasmonic Near-Field Enhancement.** As a matter of fact, the molecular infrared absorption is proportional to the change of the dipole moment, the orientation of the molecule with respect to the incident radiation, and the square of the applied electric field  $E$  at the side of the molecule.<sup>1</sup> This dependency was also proven to be correct for nonresonant SEIRA.<sup>14</sup> For resonant surface-enhanced light–matter interaction, also including resonant SEIRA, the relation requires a more detailed consideration. In a s-SNOM measurement, the recorded light intensity elastically scattered from an individual object located in the hot-spots of a resonantly excited plasmonic nanoantenna scales with the fourth power of the local near-field.<sup>104</sup> Furthermore, the electromagnetic enhancement in SERS also scales with the fourth power of the local plasmonic fields.<sup>124,125</sup>

For resonant SEIRA, Dregely et al. investigated the relation between enhanced vibrational signal and plasmonic near-field intensity by evaluating the SEIRA enhancement of selectively positioned nanometer-sized molecular probes.<sup>18</sup> First, employing EBL, arrays of gold nanoantennas with lengths matching a vibrational band of the molecular probe hydrogen silsesquioxane (HSQ) at  $2252 \text{ cm}^{-1}$  were fabricated. In a second electron beam step, patches of HSQ were placed at different distinct positions with respect to the antennas; see Figure 9a. Subsequent SEIRA spectroscopy of the respective samples reveals the strongest vibrational signals for molecular patches

located at the antenna tips. Shifting the molecular patch toward the center of the antenna or to the bare substrate yields reduced signal strengths (see Figure 9b). Such behavior is quantitatively expected from simulated near-field distributions of resonantly excited nanoantennas, where the electric fields are also confined around the tips (see Figure 9d). For a quantitative analysis, the enhanced vibrational signal strengths are extracted and plotted versus lateral patch positions in Figure 9c. Additionally, the integrated near-field intensity ( $E/E_0$ )<sup>2</sup> in the patch volume as a function of patch position is shown. A very good agreement between the integrated near-field intensity and the enhanced vibrations probed in the far-field is observed. On one hand, this result proves that the enhanced vibrational signal scales with the electrical field squared. Additionally, local fields may slightly alter the enhancement as derived from a coupled dipole–dipole model introduced by Rezus et al.<sup>113</sup> On the other hand, this demonstrates that the enhanced vibrational signal is highly confined around the tip ends.

In fact, the field and signal localization depend on the antenna geometry and arrangement. Nanoantennas arranged in a cross geometry provide higher near-fields in the junction than at the outer ends of the rods due to near-field interaction between different arms as demonstrated by Brown et al. (see Figure 9e and f).<sup>126</sup> Consequently, the enhanced vibrational signals are strongest for molecules located in the gap as was experimentally demonstrated for  $50 \text{ nm}$  thick  $\text{SiO}_2$  patches deposited in the respective areas. In agreement with FDTD simulations, a significantly stronger  $\text{SiO}_2$  vibration is found for material placed in the junction even though 4 times less material is used (see Figure 9e and f).

While in the above-mentioned studies, arrays of plasmonic nanostructures were employed to study the localized SEIRA enhancement, single nanoobjects were used in a recent work by Vogt et al.<sup>19</sup> Utilizing advanced nanomanipulation techniques, single  $\text{SiO}_2$  spheres (diameter approximately  $200 \text{ nm}$ ) were placed on distinct positions in resonantly tuned single nanoslits prepared in a continuous gold film. The plasmonic resonance was tuned to the  $\text{SiO}_2$  vibration, which is in fact a localized surface phonon polariton. In analogy to the work by Dregely et al., the enhanced vibrational strength is extracted from relative reflectance measurements and plotted versus the lateral  $\text{SiO}_2$  sphere position in the slit. As expected from near-field simulations, the highest signal enhancement is observed if the nanoparticles are localized in the slits center.<sup>19</sup> It decreases if the particle is moved toward the slit ends, demonstrating once more the localization of field and signal enhancement (see Figure 9 g and h).

From a different point of view, the molecules act as a probe for the near-field and thus provide an elegant way to obtain information on the near-field distributions of plasmonic particles as will be detailed in section 6.1.

**3.4.3. Sensitivity.** To quantify the sensitivity of SEIRA, a common benchmark parameter is needed. In some studies, it is the number of molecules from which the enhanced vibrational signal arises.<sup>15,127</sup> Commonly, this value is given per nanoantenna even though arrays of nanoantennas are measured. The definition is exact for single particle measurements but may be misleading for arrays. In array measurements, a much larger number of molecules contribute to the measured vibrational signal, and single particle studies would result in a drastically reduced signal-to-noise ratio, hampering the detection of the enhanced signal. Furthermore, the use of the number of molecules as a figure of merit also has its limitations. It is more

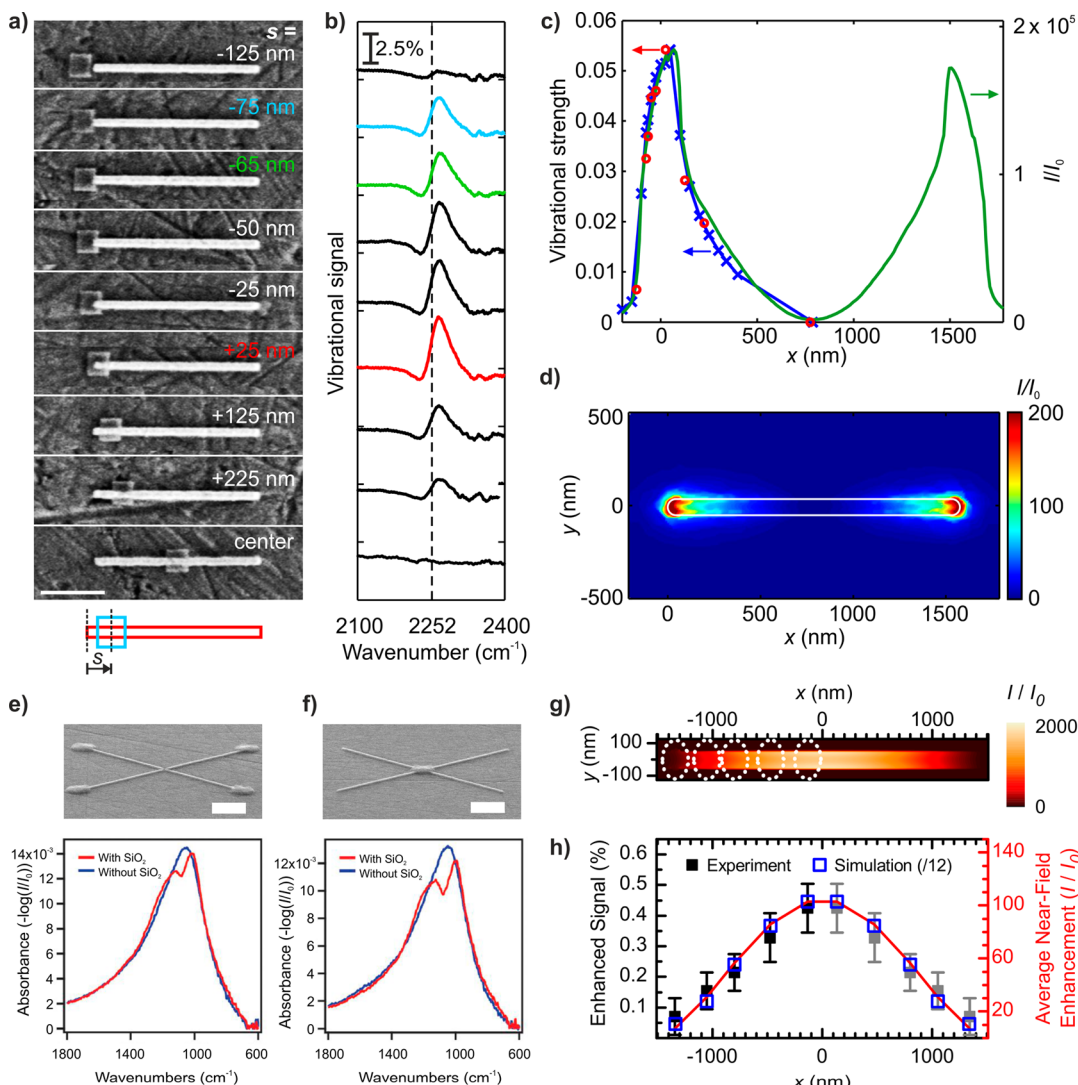


**Figure 9.** (a) The scanning electron micrographs show nine samples with different HSQ patch positions and a fixed antenna length (scale bar 500 nm). (b) Measured vibrational signals for the nine samples (spectra shifted vertically) with the black dashed line indicating the vibrational band of HSQ at  $2252\text{ cm}^{-1}$ . The scanning electron micrographs with colored labels and the colored spectra correspond to the patch positions of Figure 3. (c) The red circles are the strength of the measured vibrational signal in (b) as a function of the patch position. The blue curve is the simulated vibrational strength for 19 different patch positions normalized to the experiment (multiplied by a factor 0.85). The green curve is the simulated near-field intensity enhancement  $I/I_0$  summed in the volume of the HSQ patch shifted in 10 nm steps along the  $x$  axis.  $I$  and  $I_0$  are the near-field intensities with and without antenna, respectively ( $I = |E_x|^2 + |E_y|^2 + |E_z|^2$ ). (d) The numerical calculated top view of  $I/I_0$  in the plane 10 nm above the antenna is shown for the dipole antenna. (e,f) SEM images at a  $75^\circ$  tilt showing silica patches deposited in the junction (f) and on the ends of the rods (e) for gold antennas with  $L = 1800$  nm. Corresponding FTIR absorbance spectra for  $3 \times 3$  arrays of antennas with silica patches (red) and without silica patches (blue) for the spatial arrangements shown in (e) and (f). (g) Simulated electric near-field intensity of a nanoslit at resonance when excited with light polarized with the magnetic field component parallel and electric one perpendicular to the slit. Fields recorded in a plane parallel to the substrate at half height of the slit. The positions where the silica spheres have been placed are indicated. (h) Measured (black, mirrored copies in gray) and simulated (blue) enhanced phononic signal of single silica spheres (nominal diameter 237 nm) positioned at various sites of plasmonic nanoslits, and simulated average near-field intensity (red) at the sites, where the silica spheres are located. (a–d) Adapted with permission from ref 18. Copyright 2013 Macmillan Publishers Ltd.: Nature Communications. (e and f) Reprinted with permission from ref 126. Copyright 2013 American Chemical Society. (g and h) Adapted with permission from ref 19. Copyright 2017 American Chemical Society.

demanding to detect a single diatomic species as compared to a single protein. Hence, the molecular weight or, more precisely, the number of bonds contributing to the enhanced signal should be a more suitable quantity, even though the oscillator strength varies also from bond to bond.

Sometimes, the sensitivity is characterized in terms of concentration (molar) calculated from the number of detected molecules adsorbed in the hotspots multiplied by their weight.<sup>126,128</sup> This definition comes along with its own limitations, because it may suggest that the quantity can be

detected outside of a solution. This, however, requires a targeted delivery of the solute to the nanometer-scale near-fields, which is a challenging task in microfluidics and nanofluidics. Nevertheless, a first approach utilizing superhydrophobic surfaces was already applied to resonant SEIRA.<sup>129</sup>

A further commonly used definition of SEIRA sensitivity is the enhancement factor (EF), which relates the enhanced signal strengths to standard IR techniques (transmission, reflection).<sup>15,83,130,131</sup> It is defined as

$$EF = \frac{I_{SEIRA}}{I_0} \frac{A_0}{A_{SEIRA}}$$

where  $I_{SEIRA}$  is the enhanced and  $I_0$  the unenhanced signal strength. Furthermore,  $A_{SEIRA}$  and  $A_0$  denote the areas (volumes) covered (filled) with molecules in SEIRA or reference measurements, respectively.<sup>130,131</sup> Particularly, the active area (volume)  $A_{SEIRA}$  in SEIRA spectroscopy is not well-defined and requires a detailed consideration. As seen in Figure 9c, the enhanced SEIRA signal mainly originates from the molecules located in the antenna hot-spots, for example, the tip ends for a linear antenna. On the basis of this finding, a commonly used approximation for the active area is the surface of the tip ends.<sup>130</sup> This is an admittedly rough approximation, in particular if the entire sample including nanoantennas and underlying wafer is covered with a homogeneous thin film of analytes and not exclusively the surface of the nanostructure.

However, following this definition, an enhancement factor of 500 000 as compared to standard IR transmittance spectroscopy is found for the ODT covered cylindrical nanoantenna with hemispherical tips as discussed in section 3.2. This corresponds to the detection of about 100 000 ODT molecules adsorbed on this single antenna, or approximately 50 attograms of ODT. Typical enhancement factors found in other studies range from 1000 to 100 000 depending on the antenna shape, material, and arrangement as discussed in section 4.

**3.4.4. Wavelength Scaling.** From both experiments and numerical calculations, it is known that the plasmonic near-field intensity of a resonantly excited nanostructure tends to increase with its size.<sup>132,133</sup> As was discussed in section 3.4, the sensitivity of SEIRA is directly linked to the near-field intensity of the plasmonic structure. Consequently, by increasing the antenna length and hence decreasing its resonance frequency, a higher SEIRA enhancement is expected. In a recent study by Weber et al., this dependence was detailed for linear nanorods.<sup>134</sup> The authors performed resonant SEIRA studies with fullerenes C<sub>60</sub> and C<sub>70</sub> as probe molecules, which exhibit characteristic absorption bands over a broad spectral region from 500 to 1500 cm<sup>-1</sup>. Antennas of varying lengths were used to match the plasmonic resonances to the vibrational bands of interest, and the enhanced vibrational signal was determined. With respect to signal enhancement, an increase of 1 order of magnitude was found going from mid-infrared frequencies (1500 cm<sup>-1</sup>) to the far-infrared (500 cm<sup>-1</sup>). This result is in good agreement with numerical FDTD simulations of the integrated near-field intensity, as illustrated in Figure 10.

Additionally, antenna theory<sup>135,136</sup> was used to obtain an analytical expression for the scaling of the SEIRA enhancement with wavelength. A proportionality to  $\lambda^3$  of the SEIRA enhancement is found, which is in good agreement with numerical simulations as well as experimental data (see Figure 10). This behavior is expected to remain valid down to single-digit THz frequencies but will break down eventually due to the influence of the material dispersion.

This result also suggests a large potential for the use of plasmonic enhancement in THz spectroscopy as demonstrated in several studies.<sup>23–25</sup>

#### 4. OPTIMIZATION OF VIBRATIONAL SIGNAL ENHANCEMENT

The enhancement of IR vibrational signals is highly dependent on geometrical and spectral properties of the near-fields of the nanostructures. Therefore, over the last 10 years, researchers

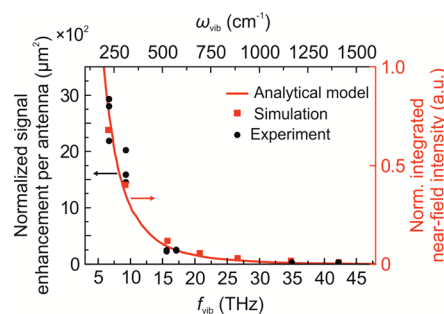


**Figure 10.** Experimentally determined normalized signal enhancement in SEIRA (●) and normalized integrated near-field intensities of nanoantennas obtained from numerical FDTD simulations (red ■) and classical antenna theory (red line) as a function of the vibrational frequency  $f_{\text{vib}}$ . More details are found in ref 134. Adapted with permission from ref 134. Copyright 2016 American Chemical Society.

strived to optimize geometries and materials of nanostructures, their arrangements, the underlying substrates, and experimental measurement configurations as reviewed in the following.

##### 4.1. Geometrical Properties

Enabled by the rapidly growing progress in micro- and nanostructure fabrication, a variety of differently shaped nanostructures arranged in various geometries have been explored to optimize the SEIRA enhancement or a certain antenna functionality as discussed in the following.

**4.1.1. Nanoantenna Shape.** The first experiments using resonantly excited nanostructures for SEIRA were carried out using linear rod shaped nanoantennas (see section 3.2).<sup>15</sup> Although the linear antenna represents one of the simplest nanostructures, it is still commonly used, due to its high performance and its simplicity. Besides the well-known half-wave dipole antenna, several other concepts have been transferred from radio frequency antenna design. One example, extensively used in the RF frequency range, is the quarter-wave monopole antenna. Typically, the antenna element is arranged perpendicular to a semi-infinite ground plate, which requires advanced nanofabrication methods for three-dimensional structures. However, Adato et al. have shown that the semi-infinite ground plate can be replaced by using a small nanorod as a wire reflector.<sup>137</sup> The proposed structure is shown in Figure 11a together with the current density illustrating the operation principle. Additional advantages are the compact geometry and the possibility to combine two monopole antennas within a single nanoparticle. In such a configuration, the wire reflector isolates the two monopoles, enabling an independent tuning of each element, which can be exploited for dual-band resonant SEIRA also (see section 4.5). The inset of Figure 11a shows the near-field excitation at the resonance frequency of such a monopole antenna, where a single hot-spot is observed. Moreover, resonant SEIRA was also reported for nanocross geometries.<sup>138</sup>

Another geometry established for resonant SEIRA is represented by split-ring resonators (SRRs); see Figure 11b. Essentially, an SRR is an optical antenna, which is excited resonantly if the perimeter of the SRR is equal to a half integer multiple of the wavelength.<sup>127</sup> Consequently, the SRR resonance can be tuned from the terahertz to the visible spectral range by varying the radius of the SRR. As compared to linear nanorods, SRRs are compact nanostructures with a nanometer-sized gap, offering potentially larger near-field enhancement inside the gap region, which will in turn lead to

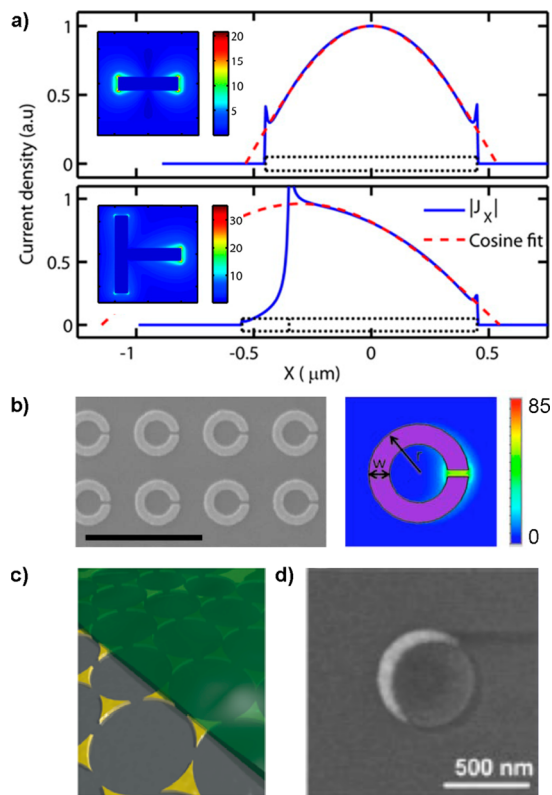


**Figure 11.** Selected nanoparticle geometries used for resonant SEIRA. (a) Simulated current density of a monopole antenna (lower panel) as compared to a dipolar antenna (upper panel). One-half of the monopole antenna is formed by an image, rather than a physical structure. The near-field enhancement normalized to the incident electromagnetic field (insets) of the monopole antenna shows a single hot-spot in contrast to the dipolar antenna providing two hot-spots. (b) SEM and simulated electromagnetic near-field distribution (normalized to incident field) of a split-ring resonator. Scale bar is 1  $\mu\text{m}$ . (c) Triangular shaped nanostructures and (d) nanocrescents, both fabricated by nanosphere template lithography allowing for large-area and low-cost nanostructure fabrication. (a, c, and d) Adapted with permission from refs 137, 92, and 139. Copyright 2011 American Chemical Society, 2011 American Chemical Society, and 2009 American Chemical Society. (b) Adapted with permission from ref 127. Copyright 2009 AIP Publishing.

higher signal enhancements. In 2009, such structures have been used by Cubukcu et al. to detect minute amounts of ODT with zeptomolar sensitivity.<sup>127</sup> Moreover, asymmetric SRRs<sup>140</sup> were employed as SEIRA substrates to sense a monolayer of bovine serum albumin (BSA) proteins.<sup>141</sup> Asymmetric SRRs are plasmonic structures consisting of two arcs with the same center of curvature but different arm lengths. This asymmetric configuration results in a symmetric (bright) and an antisymmetric (dark) mode, whose interference leads to the formation of Fano-shaped peaks, with a high Q-factor and, consequently, a higher local optical field intensity.<sup>142</sup> As shown recently, the enhancement of such structures is further increased if metal–dielectric–metal stacked structures are used, where a thin dielectric layer is sandwiched between two metals. Chae et al. have shown that such asymmetric SRRs composed of two silver layers separated by a silver oxide layer provide 44% larger enhancement as compared to the same structure made from pure silver.<sup>127</sup> In the experiments, both kinds of structures were covered with a PMMA layer and

characterized using a photothermally induced resonance technique. The authors claim that the additional enhancement is caused by the dielectric layer, which provides an extreme field confinement and enables the synergistic excitation of the plasmonic modes of the two metal layers. Besides their capability for resonant SEIRA, SRRs offer the additional advantage of a low-cost and large-area nanofabrication as shown by Cataldo et al. employing hole-mask colloidal nanolithography.<sup>85</sup>

Another low-cost lithography technique, employed for the fabrication of SEIRA substrates, is nanosphere lithography. The technique relies on the use of self-assembled spherical particles as a shadow mask for subsequent metal evaporation and can be used to fabricate hexagonally arranged triangular nanoparticles on a large scale (see Figure 11c).<sup>143,144</sup> Hoffmann et al. demonstrated that the plasmonic resonance of such triangular shaped particles is tunable from 3 to 13  $\mu\text{m}$  by varying the diameter of the spheres and the refractive index of the underlying substrate. Furthermore, they sensed enhanced absorption bands of a PMMA layer spin coated on top of the nanostructures. The highest enhancement of the vibrational bands was found for low refractive index substrates as a result of the reduced image charges induced inside the substrate.<sup>92</sup>

A further development of nanosphere lithography is the nanosphere template lithography. This technique uses an oblique deposition angle and an additional argon ion milling step to fabricate nanocrescents (Figure 11d).<sup>145</sup> The structures benefit from the lightning rod effect originating from the tapered ends of the crescents, and therefore show SEIRA enhancements factors of up to 50 000.<sup>139</sup>

**4.1.2. Antennas Supported by Metal Films.** Nanostructures supported by a metallic layer, also known as perfect absorbers, are another kind of nanostructure for resonant SEIRA. In general, perfect absorbers can be understood as layers that have zero-transmission and reflection coefficients:  $R = T = 0$ .<sup>146</sup> Typical designs of perfect absorbers in the infrared spectral range consist of nanostructures on top of a metallic sheet, separated by an isolating spacer layer. The metallic sheet guarantees the zero-transmission, whereas the layer thickness of the spacer layer is used to tailor the reflectance of the system. To ensure zero reflection, the thickness of the layer is adjusted to create a reflected plane wave that interferes destructively with the wave radiated by the nanostructures itself. This concept has been applied to resonant SEIRA, for example, by Chen et al.,<sup>147</sup> by placing a monopole antenna on top of a gold sheet separated by a magnesium fluoride ( $\text{MgF}_2$ ) spacer layer. By varying the layer thickness of the  $\text{MgF}_2$  spacer layer, the authors optimized the optical path difference to reach destructive interference and therefore minimum reflectance. With this configuration, more than 90% peak plasmonic absorption combined with very narrow resonances are achievable. Similar systems employing nanocrosses<sup>148</sup> or nanodiscs<sup>149</sup> have been used for resonant SEIRA. Depending on the kind of nanoantenna and adsorbed molecule, enhancement factors of up to  $2.2 \times 10^6$  are observed.<sup>149</sup>

To detail the benefit of antennas supported by metal films for SEIRA, systematic numerical and experimental studies have been carried out by Brown et al. using fan-shaped antennas on top of a reflective gold layer separated by a silicon dioxide spacer.<sup>150</sup> The fan-shaped antennas consist of two rods with semicircular ends (see Figure 12a) separated by a nanometer-sized gap. As compared to linear antennas, the fan-shaped geometry offers two additional advantages, high spatial near-

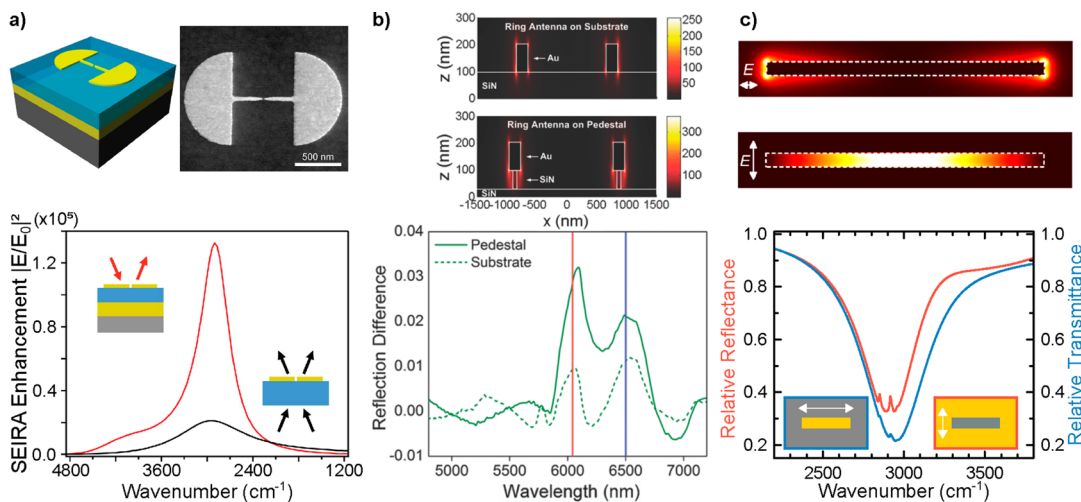


**Figure 12.** (a) Fan-shaped nanostructure on top of a reflective substrate. The upper panel shows a schematic illustration as well as a SEM image, and the lower panel shows the near-field enhancement of a fan-shaped antenna directly placed on the substrate (black curve) as compared to a structure placed on top of a gold mirror, separated by a spacer layer (red curve). Reprinted with permission from ref 150. Copyright 2015 American Chemical Society. (b) Nanoantennas on pedestals: The upper panel shows the near-field distribution of planar nanostructures and nanostructures placed on a pedestal. The benefits for resonant SEIRA are seen in the lower panel, which shows the SEIRA signal of protein layers adsorbed on both geometries. Reprinted with kind permission from ref 152. Copyright 2014 Wiley-VCH Verlag GmbH & Co. KGaA. (c) Nanoslit geometry: Near-field amplitude (normalized to incident IR radiation) of a nanoantenna and a nanoslit. Whereas the nanoantenna features two hot-spots, a nanoslit features only one extended hot-spot at the center of the slit. The lower panel shows the SEIRA signal of a monolayer ODT adsorbed on a nanoantenna/nanoslit array with the very same geometry. Much bigger SEIRA signals are obtained for the slit geometry. Reprinted with permission from ref 151. Copyright 2015 American Chemical Society.

field confinement within the nanogap and an expansive electron reservoir in the semicircular ends. To optimize the structure with respect to the vibrational enhancement, the spacer layer was varied, and the influence on the electromagnetic near-field was evaluated. Supported by numerical calculations, the authors found that the thickness of the spacer layer has to be adjusted carefully to the incident wavelength. The optimum enhancement was achieved for a layer thickness slightly smaller than a quarter of the wavelength. Following this approach, the near-field intensity can be increased by nearly an order of magnitude (see Figure 12a).<sup>150</sup> The additional enhancement above the reflective plane is provided through constructive interference of scattered electromagnetic waves and therefore is strongly dependent on the scattering cross-section of the nanostructure in use. Consequently, large nanostructures with high volumes and hence large scattering cross-sections, such as fan-shaped or bowtie antennas, benefit more from this effect than low-volume structures such as thin rods.<sup>150</sup>

**4.1.3. Antennas on Pedestals.** A further step toward maximum SEIRA sensitivity can be achieved by elevating nanostructures from the substrate, for example, by placing them on pedestals. As compared to nanostructures located directly on the substrate, this geometry features two main advantages. First, the overlap between plasmonic near-field and molecular layer and therefore the sensing area is increased if the cross-section of the pedestal beneath the nanostructure is slightly smaller than that of the nanostructure itself (see Figure 12b). Second, the effective refractive index of the advanced substrate is further diminished, leading to a blue shift of the resonant wavelength.<sup>151</sup> Consequently, for a desired resonance frequency, the length of the nanostructures can be increased as compared to nanostructures directly located on top of the substrate. Hence, more electrons contribute to the plasmon oscillation, and therefore an increased near-field intensity is generated (see also section 3.4). Following this approach, Cetin

et al. demonstrated that the sensing area of nanorings placed on pedestals is nearly doubled and that the SEIRA signal is nearly tripled as compared to nanoantennas directly placed on the substrate (see Figure 12b).<sup>152</sup> In a more detailed study, Huck et al. revealed that the height of the pedestal also plays a crucial role and can be used to maximize the near-field intensity by exploiting interference effects as discussed previously.<sup>151</sup> Improvements of the SEIRA enhancement of 1 order of magnitude and more are feasible following this approach.

**4.1.4. Babinet's Principle: Nanoslits.** So far, only SEIRA sensing platforms based on solid metal nanoparticles are discussed. However, according to Babinet's principle, so-called inverse nanostructures, consisting of nanoapertures in a continuous metallic film, also feature plasmonic resonances.<sup>153–156</sup> Recently, the use of these structures for resonant SEIRA has been studied by comparing their optical properties with those of their particle counterparts. As a direct consequence of Babinet's principle, only minor differences in the far-field responses of a nanoantenna and the corresponding counterpart, a nanoslit, are visible (see Figure 12c). Importantly, several quantities exchange their respective roles in the inverse nanoslit system, for example, reflectance and transmittance or perpendicular and parallel polarization of the incident light.<sup>151</sup> In contrast to the similar far-field response, the comparison of the near-field of a nanoantenna and a nanoslit brings forward major differences, as depicted in Figure 12c. Following Babinet's principle, these differences can be understood as a consequence of the commutation of electric and magnetic field components. The well-known dipolar pattern of the electric hot-spot of a nanoantenna transforms into a single hot-spot in the center of a nanoslit, reminiscent of the magnetic field component. Huck et al. demonstrated that this single, extended hot-spot is beneficial for resonant SEIRA as it produces a signal of molecules adsorbed on the sidewalls of the slit, which is approximately 3 times higher as compared to

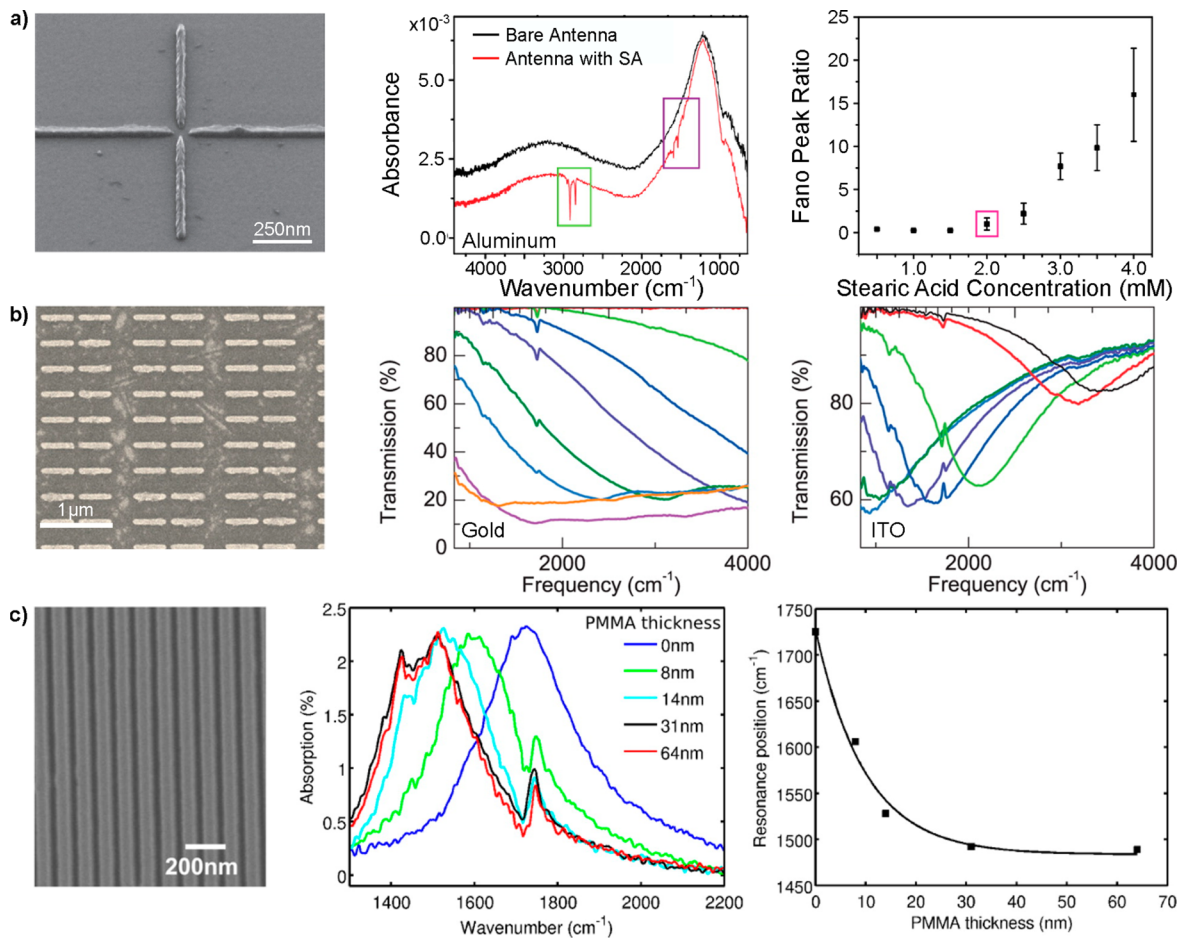


**Figure 13.** Different materials employed for resonant SEIRA: (a) Aluminum cross-antennas for self-calibrating SEIRA. SEM image recorded under an angle of 75° (left panel), spectra before and after functionalization with stearic acid (middle panel), and Fano peak ratio between the enhanced signal of the C–H peak (marked in green in the middle panel) normalized to the Fano peak intensity of the  $\text{Al}_2\text{O}_3$  resonance at  $900 \text{ cm}^{-1}$  for different stearic acid concentrations (right panel). (b) Left panel shows an SEM image of ITO antennas; the middle and right panels show IR spectra of Au and ITO antennas with very high antenna densities for different antenna lengths. (c) SEIRA utilizing graphene nanoribbons. SEM image (left panel), SEIRA spectra for different PMMA layers covering the graphene nanoribbons (middle panel), and resonance position in dependence of the layer thickness (right panel). Reprinted with permission from refs 163–165. Copyright 2016 American Chemical Society, 2013 American Chemical Society, and 2014 American Chemical Society.

the SEIRA signal generated by the corresponding particle structure (linear nanoantenna; see Figure 12c).<sup>151</sup> Interestingly, the increase in SEIRA signal strength is a consequence of the larger hot-spot volume (more molecules) and of the higher near-field intensity. However, the SEIRA enhancement also crucially depends on the slit width. For small widths, an increased SEIRA signal was observed.<sup>151</sup> An additional gain of the near-field intensity is obtained by squeezing the light in a point-like hot-spot,<sup>157</sup> for example, by using inverse bowtie antennas as shown by Cetin et al.<sup>158</sup> In this study, the fabrication of bowtie shaped apertures with gap-sizes in the sub-10 nm regime was demonstrated, and a corresponding near-field intensity of  $|E|^2 > 65\,000$  was calculated. This extremely high near-field intensity is promising for resonant SEIRA, but has not been demonstrated yet.

In other studies, more complex geometries of inverse nanostructures, for example, nanocrosses,<sup>110</sup> H-shaped nanoapertures,<sup>152</sup> and Jerusalem cross-shaped nanoapertures,<sup>159</sup> have been utilized for SEIRA. Furthermore, inverse nanostructures have also been combined with reflective metallic layers to exploit interference effects,<sup>160</sup> as discussed in section 4.1.2.

#### 4.2. Material Properties

The choice of the plasmonic material strongly influences the absorption cross-section of nanoparticles and hence the SEIRA enhancement (see section 3.3). As shown by Neuman et al. for a linear gold antenna, the ratio of absorption (mainly determined by the plasmonic material) and scattering (mainly given by the antenna geometry) cross-sections crucially impacts the SEIRA enhancement.<sup>63</sup> Consequently, an optimized SEIRA structure requires a tailored adjustment of material and geometry. Typical materials used for resonant SEIRA include “classical” metals (e.g., Au, Al, or Ag), highly doped semiconductors, and graphene as reviewed in the following.

So far, the majority of resonant SEIRA studies are carried out using gold nanostructures, as gold combines several advantages.<sup>15,161</sup> First, the dielectric function of gold follows a nearly perfect Drude-type behavior in the infrared spectral range with a low damping rate,<sup>162</sup> leading to sharp plasmonic resonances. Second, gold is stable under ambient conditions and biocompatible and therefore promising for SEIRA applications in biology and medicine.

Another metal suited for SEIRA is aluminum as was recently demonstrated by Cerjan et al. In contrast to gold, aluminum

forms a thin self-passivating oxide layer of about 2–4 nm thickness, which is ideally suited for a variety of attachment chemistries with numerous functional groups,<sup>163</sup> enabling the localization of molecules in the plasmonic hot-spots. In the above-mentioned studies, aluminum cross-antennas (see Figure 13a, left panel) providing two polarization-dependent plasmonic resonances are investigated with respect to SEIRA.

One plasmonic resonance is tuned to the phononic excitation of an  $\text{Al}_2\text{O}_3$  layer (see also section 5), whereas the other one is tuned to the vibrational band of molecules adsorbed on the antennas (see Figure 13a, middle panel). By calculating the ratio between the enhanced signal strength of the molecular and phononic vibrations, the authors introduce a measure for the molecular coverage. This concept was demonstrated by immersing aluminum nanoantennas in different concentrations of steric acid. As the concentration is increased, the coverage of molecules attached to the aluminum also increases. Consequently, the enhanced molecular signal strength increases, whereas the phononic remains almost constant (see Figure 13a, right panel). This approach utilizing oxide layers of plasmonic materials as a reference offers an elegant way to determine the number of molecules present on the nanoantennas and is therefore called self-calibrating SEIRA.

A further interesting type of material for SEIRA is doped semiconductors, which feature several interesting advantages. First, access to a wide range of semiconductor fabrication techniques is available, enabling high material quality. Second, doped semiconductors promise on-chip integration of plasmonic antennas, detector, and read-out electronics. Third, the plasmonic resonance is tunable via the doping level. However, to obtain plasmonic resonance in the infrared spectral region, very high doping concentrations are needed. So far, the use of this material type has only been demonstrated for a restricted spectral region below  $1500 \text{ cm}^{-1}$  using heavily doped indium arsenide, indium antimonide, zinc oxide, or germanium nanostructures.<sup>166–169</sup> Furthermore, the enhancement is much lower as compared to gold nanostructures for two reasons: First, the relatively low bulk plasma frequency of the material (typically located in the IR) leads to a high penetration depth (in the order of the geometrical dimensions, or even higher), causing high electromagnetic fields inside the material, which are therefore not available for sensing. Second, due to the operation at frequencies close to the plasma frequency, the optical properties of the nanoparticles are dominated by internal damping (electronic losses), whereas external losses (radiation damping) are comparably small. However, as discussed in section 3.3.4, the highest enhancement is expected if both damping mechanisms contribute equally.

SEIRA experiments employing indium tin oxide (ITO) nanostructures have been reported by Abb et al.<sup>164</sup> ITO is a transparent (in the visible) conducting oxide with a large bandgap and a free charge carrier density between those of doped semiconductors and noble metals. In contrast to metal nanostructures, ITO structures are dominated by plasmonic absorption, whereas plasmonic scattering can be completely neglected. This fact was exploited to create high density ITO arrays shown in Figure 13b. In contrast to gold nanostructure arrays, the ITO antennas do not couple to neighboring antennas due to the negligible light scattering, which is a consequence of the lower electron density and the smaller volume of ITO nanostructures. Whereas a shift of the resonance frequency and a broadening of the resonance are

observed for high density metal nanostructure arrays, the response of ITO nanoantennas is nearly unaffected even for very high densities (see Figure 13b middle and right panels for a comparison of Au and ITO antennas). Therefore, the lower enhancement provided by a single ITO antenna is counterbalanced by the density of ITO nanoantenna arrays.

Graphene is also considered as a promising candidate for resonant SEIRA.<sup>148,170–172</sup> First experiments were carried out with graphene nanoribbons as depicted in the left panel of Figure 13c. Outstanding properties of graphene are very strong light confinement and the possibility of postfabrication tuning by electrostatic gating. The latter is discussed in more detail in section 4.5. The strong light confinement has been investigated by Li et al.,<sup>165</sup> whose results are shown in the middle and right panels of Figure 13c. By investigating graphene nanoribbons coated with PMMA layers of different thicknesses, the authors found a plasmonic red-shift and a saturation of the SEIRA signal for very thin PMMA layers of approximately 20 nm thickness. In contrast, the confinement for Au antennas is much lower, as, for example, shown by Neubrech et al. (see also section 3.4 and section 6.1).<sup>101</sup> Furthermore, Rodrigo et al. have shown that SEIRA signals of graphene nanoribbons can outperform that of gold nanoantennas by a factor of 3.<sup>171</sup> Additionally, the resonances of graphene nanoribbons can be tuned electrically,<sup>171</sup> allowing for shifting of the resonance over several vibrational bands.

### 4.3. Nanoscopic Properties

An aspect of resonant SEIRA that is only rarely considered up to now is the impact of nanoscopic properties, such as antenna morphology or analyte adsorption, on the signal enhancement. As known from surface science, the infrared absorption (vibrational frequency, line width, and strength) of molecules adsorbed on metal surfaces crucially depends on the orientation of the molecular dipole moment with respect to the surface normal and incident radiation, the type of adsorption (chemisorption or physisorption), the adsorption sites, and the crystalline orientation of the surface itself.<sup>173</sup> Even though the effects are of fundamental nature, they have a tremendous impact in applications, for example, when molecular vibrations of proteins in the presence of gold surfaces are investigated.<sup>174</sup>

For SEIRA spectroscopy using resonantly excited nanoantennas, the situation is even more complex due to the resonant and highly nonuniform nature of the confined near-fields. Recently, Iwasa et al. developed a model for molecules interacting with such arbitrary nonuniform electric fields as present in SEIRA.<sup>175</sup> Utilizing a multipolar Hamiltonian, the light–matter interaction is treated by a spatial integral of the inner product of molecular polarization and spatial field distribution. As a result, the authors find that the electric field lines as well as the intensity gradients of the nonuniform fields significantly impact the enhanced molecular vibration. This allows an assessment of the orientation of the respective vibrational groups in the plasmonic fields if the metal surface is well-defined, for example, atomically flat.

However, the experimental realization of tailored nanostructures with such well-defined surface properties is a challenging task. On one hand, approaches of chemical syntheses providing high crystalline quality and high aspect ratios (which are necessary for the formation of high-quality IR resonances) are rarely available.<sup>176</sup> On the other hand, lithographically prepared nanostructures often consist of evaporated materials with low crystalline quality.<sup>99</sup> Furthermore, a certain surface roughness is

inherent to the evaporation process in standard nanofabrication, which also impacts the SEIRA enhancement as demonstrated by Aksu et al.<sup>87</sup> In another study, where porous gold nanoantennas as a 3D extension of surface roughness were investigated, SEIRA enhancements comparable to those of solid nanostructures were found.<sup>89</sup> Additionally, single nanostructures should be investigated instead of nanoobjects arranged in arrays to avoid averaging effects caused by fabrication inhomogeneities. Together, these factors make studies of nanoscopic properties highly demanding.

As an initial study in this field, individual linear nanoantennas were tailored by focused ion beam milling from monocrystalline gold platelets and covered with a self-assembled monolayer of ODT. As compared to nanoantennas of lower crystalline quality prepared by EBL and thermal evaporation of gold, a significantly higher SEIRA enhancement factor of  $3.6 \times 10^6$  was obtained. The factor corresponds to the detection of approximately 15 000 molecules or 7 attograms of chemically bound ODT, which is to our knowledge the best value reported so far. We attribute the increased enhancement to an improved formation of the chemisorbed ODT self-assembled monolayer on the high crystalline quality surface of the nanoantenna and a reduced plasmonic damping.

The above-mentioned examples demonstrate the impact of nanoscopic properties on the enhancement in resonant SEIRA, particularly if molecular species are chemically bound to SEIRA substrates. In sensing applications, this effect might be of significant importance for the chemical functionalization of nanoantennas to selectively bind certain biomolecules.<sup>177</sup> A detailed study of the role of molecular adsorption in resonant field-enhanced spectroscopy techniques including SEIRA, however, requires sophisticated approaches in analogy to surface science.

#### 4.4. Interaction between Resonant Nanoantennas

The sensitivity of resonant SEIRA is further increased if interacting nanoparticles are used. Commonly, one distinguishes between near-field interaction of pairs of nanoantennas separated by nanometer sized gaps (dimers) and the excitation of collective plasmonic oscillations in arrays of periodically arranged nanostructures. While near-field coupling offers high field intensities, preparing such structures with small gaps as well as subsequently filling those gaps with molecules remains challenging, especially on large areas. In arrays of plasmonic structures, however, a different type of interaction mediated by the far-field can arise. In contrast to the near-field interactions, fabricating SEIRA structures that benefit from far-field interactions is simple and straightforward with standard fabrication techniques. This makes those structures more promising for use in practical applications, unless one is interested in very small detection volumes, where extremely high field intensities are necessary.

**4.4.1. Near-Field Interaction.** As is known from numerical calculations (see Figure 14a), the near-field intensity is enhanced by several orders of magnitude in nanometer sized gaps of resonantly excited antenna dimers.<sup>95</sup>

This effect is attributed to the attractive electromagnetic force between both dimer arms and was first reported for SEIRA by Dregely et al.<sup>18</sup> Using the approach described in section 3.4, the authors found that the enhanced vibrational signal of a molecular patch (size  $200 \times 200 \times 30 \text{ nm}^3$ ) increases by roughly a factor of 6 when placing it in the 55 nm gap of an antenna dimer instead of on one of its ends.<sup>18</sup> Similar results

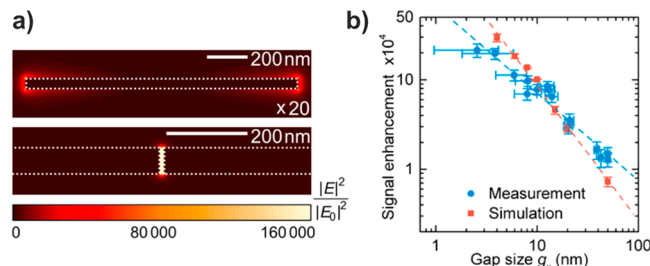


**Figure 14.** (a) Near-field distributions of a single antenna and an antenna dimer with a gap size of 10 nm at respective resonance frequencies obtained from FDTD simulations. The intensity of the single antenna was multiplied by a factor of 20. (b) Signal enhancement of molecules located in the gap of an antenna dimer (blue ●, experiment; red ■, simulation) as a function of gap size  $g_x$ . Dashed lines are fits to the data. Reprinted with permission from ref 95. Copyright 2014 American Chemical Society.

were observed for other geometries.<sup>91,126</sup> The possibilities of using such nanogaps in SEIRA were studied in detail by Huck et al.<sup>95</sup> The authors fabricated antenna dimers with gap sizes down to 3 nm by standard EBL and subsequent photochemical metal deposition.<sup>178</sup> The SEIRA enhancement was then probed with a molecular layer of CBP. Figure 14b illustrates the scaling of the SEIRA enhancement as a function of gap size. An increase of 1 order of magnitude was found when decreasing the gap size from 50 to 3 nm corresponding to enhancement factors on the order of  $10^5$ . Similar values could be achieved using buried nanocavities in metal films, which were fabricated via atomic layer deposition in combination with template stripping.<sup>179</sup>

**4.4.2. Far-Field Interaction.** For a single resonantly excited nanoantenna, the local electric field intensity is determined by the incident field and the excited LSPR. For an array of periodically arranged antennas, however, this local field intensity also depends on the electric fields created by all other antennas in the array. As the near-field is confined to tens of nanometers around the antenna,<sup>101</sup> for separations larger than 100 nm this contribution is dominated by the scattered far-fields of the antenna. The strength of the contribution depends on the phase shift, which in periodic arrangements, as illustrated in Figure 15a, is determined by the spacing between antennas.

As demonstrated by Adato et al.,<sup>83,180</sup> there is a critical periodicity

$$d_c = \frac{\sqrt{i^2 + j^2}}{n} \cdot \lambda_{\text{inc}} \quad (6)$$

where  $n$  is the refractive index of the substrate and  $\lambda_{\text{inc}}$  is the wavelength of the incident electric field, the constructive interference condition is met, and collective excitations arise. Here,  $i$  and  $j$  denote the order of the collective excitation parallel and perpendicular to the long antenna axis. The benefit of such collective excitations was first demonstrated in ref 83, where a SEIRA enhancement of  $10^8$  was achieved by combining collective and individual antenna resonances. In ref 84, the authors investigate the coupling for both directions for a longitudinal excitation of the antennas arranged in arrays with rectangular periodicity. These excitations are known as Rayleigh anomalies or grating orders and due to their radiative nature suffer from damping upon propagation through the substrate.<sup>83</sup> As confirmed by several studies, this damping leads to a

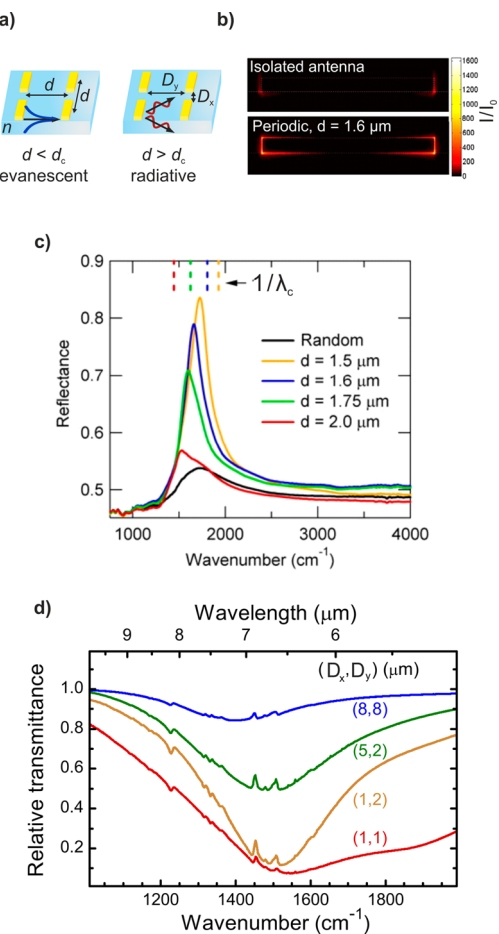


**Figure 15.** (a) Illustration of evanescent (left) and radiative (right) coupling in periodic nanoantenna arrays. The type of coupling changes at the critical periodicity  $d_c$ . (b) Numerically calculated distribution of near-field intensity for an isolated antenna and a periodic antenna array ( $d = 1.6 \mu\text{m}$ ). (c) Reflectance spectra (measured with an IR microscope (NA 0.4)) of periodic antenna arrays and a randomized antenna distribution with antennas of the length  $1.1 \mu\text{m}$ . The spectral position  $1/\lambda_c$  of the collective mode of the order ( $i = 1, j = 0$ ) for each periodicity  $d$  is indicated by the dashed lines at the top. (d) Relative transmittance spectra of antenna arrays ( $2.6 \mu\text{m}$  length,  $140 \text{ nm}$  width, antenna spacings along the short antenna axis ( $D_y$ ) and the long antenna axis ( $D_x$ ) in  $\mu\text{m}$  are indicated by the colored numbers in the plot) covered with a  $5 \text{ nm}$  thick layer of CBP. The SEIRA enhancement of the molecular vibrations of the CBP depends critically on the spacing  $D_y$ . Reprinted with permission from refs 86 and 83. Copyright 2016 American Chemical Society and 2009 National Academy of Sciences.

broadening of the far-field response and a drop of the plasmonic near-field intensity.<sup>84,164,180–183</sup> However, as demonstrated by Adato et al., periodicities slightly smaller than the critical periodicity  $d_c$  result in a significant narrowing of the plasmonic far-field response, as well as an increase of the near-field intensity. This originates because the phase shift between two antennas is close to a multiple of  $2\pi$ , resulting in a large contribution to the local field intensity, while the radiative grating order has not formed yet and therefore the antenna resonance does not suffer from damping. These effects are illustrated in Figure 15b and c, while Figure 15d shows the impact on the SEIRA enhancement. When analyzing the enhanced vibrational signal strength as a function of the antenna spacing, it is obvious that the highest density of

antennas does not result in the strongest signal. Small spacings between antennas can lead to the excitation of several grating modes of different orders, which are spectrally close to the antenna resonance (see eq 6). Because of radiation damping, those modes are broadened and overlap, which results in a dramatic loss of near-field intensity.<sup>84</sup> As discussed in several studies,<sup>84,142,180</sup> due to the radiation pattern of a dipole antenna this effect is more prominent for the transversal spacing  $D_y$ . The highest SEIRA enhancement was consequently found for distances just below the critical transversal spacing. Additionally, it is also possible to tune the spectral position of the grating order without any modification of the SEIRA substrate by varying the angle of incidence in the experiment.<sup>184</sup>

The far-field coupling has also been investigated for plasmonic nanoslits in metal films.<sup>95,160</sup> Interestingly, the influence of the transversal spacing  $D_y$  remains dominant for these inverse antenna structures, because the directional radiation characteristic remains unchanged according to Babinet's principle. In contrast to antennas, where the strongest field enhancement was found close to the first transversal grating order at  $\lambda_{\text{inc}}/n$  (see eq 6), the first grating order for slits appears at  $\lambda_{\text{inc}}/2$ .<sup>95</sup> In addition, Huck et al. discovered stronger coupling for nanoslits when compared to nanoantennas. Both effects are caused by the fact that slits couple via surface plasmon polaritons (SPPs) at the gold–air interface, whereas rod antennas couple via dipolar fields propagating within the substrate. The wavelength of these SPPs is independent of the refractive index of the substrate and close to the vacuum wavelength in the infrared. Examples of other geometries that exhibit far-field coupling include gratings<sup>94,185</sup> and microarrays.<sup>186</sup> As compared to the preparation of nanoantennas commonly used for SEIRA, such geometries provide the benefit of a simple fabrication on large areas, which is desirable for practicable applications.

#### 4.5. Broadband Signal Enhancement

Usually molecules provide several vibrational bands most often located within the fingerprint region in the mid infrared spectral range (see Figure 1a). However, the enhancement of those vibrations is only possible within a limited bandwidth provided by the plasmonic resonance, usually covering only one or few absorption lines. Although the plasmonic resonance can be tuned to any of these vibrational lines, this may not be sufficient for a characterization and unambiguous identification of molecular species. To minimize the number of false positive results, or to characterize unknown substances, an adequate enhancement of the whole fingerprint region is desirable. In some cases, for example, for organic semiconductors, the fingerprint region can be covered by the plasmonic response of a single nanoantenna.<sup>151</sup> Other molecules, however, with spectrally separated vibrations, require other solutions. One solution to overcome this problem is the use of several nanostructures with different lengths and hence resonances tuned over the whole spectral range of interest. However, this approach is time-consuming and requires a large amount of nanostructures to be covered with molecules, which might be not available in sufficient quantity. Other solutions that address this problem are dual- or multiband plasmonic structures or nanostructures, which can be tuned after the fabrication process (postfabrication tuning). Both approaches will be discussed in the following section.

**4.5.1. Dual- and Multiband Nanostructures.** One approach for a dual-band plasmonic nanostructure is the

combination of two monopole antennas. A design of monopole antennas, which consists of an antenna element and a long bar oriented perpendicular to the antenna, acting as a nanoreflector, has already been introduced in section 4.1. Adato et al. have demonstrated that two of these monopole antennas can be combined within a single nanostructure, yet still operating independently.<sup>137,187,188</sup> The system in use in combination with the near- and far-field spectral response is depicted in Figure 16a and b.

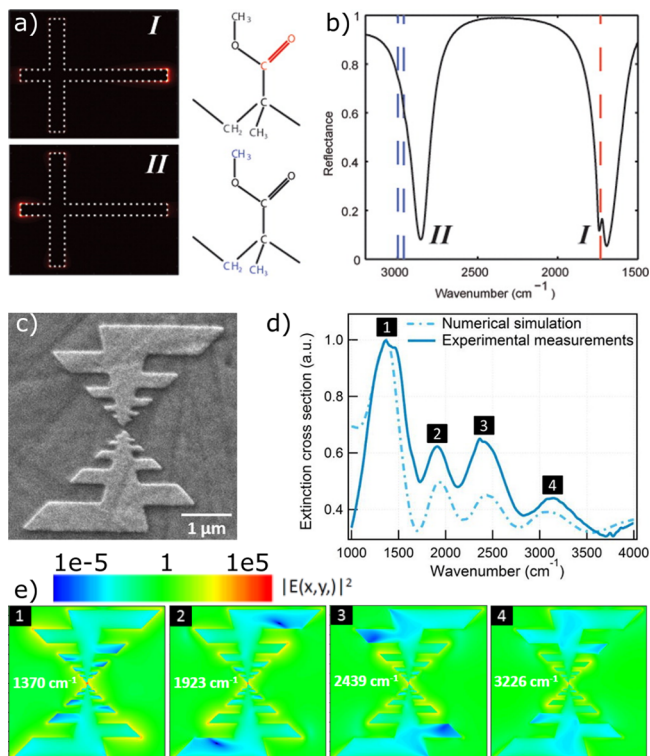


**Figure 16.** (a) Near-field distributions of two combined monopole nanoantennas at the two corresponding resonance frequencies. The two monopole antennas are used for dual-band resonant SEIRA, as depicted in (b) for enhanced vibrational signals of PMMA. (c) SEM image of a multiresonant log-periodic trapezoidal nanoantenna. (d) Corresponding far-field extinction and (e) near-field distributions at the respective resonance frequency. Reprinted with permission from refs 147 and 128. Copyright 2012 American Chemical Society and 2012 American Chemical Society.

Obviously, the nanostructure features two hot-spots with different resonance frequencies, which can be individually tuned to match two selected vibrational bands. The benefit of such a configuration for resonant SEIRA was demonstrated by simultaneously sensing two widely separated bands of thin (4 nm) PMMA layer, the C=O vibration located at  $1733\text{ cm}^{-1}$  and the C-H stretching vibration at  $2900\text{ cm}^{-1}$ .

Dual-band nanostructures have not only been designed for particle nanostructures, but have also been investigated for nanoapertures. For example, a design based on H-shaped nanoapertures with extended arms has been proposed by Cetin et al.<sup>189</sup> The dual-band resonant behavior of the aperture system originates from the individual spectral response of the constituting aperture elements, the H-shaped aperture and the rectangular parts forming the extended arms. Both resonances are excited with the same polarization, whereas a third resonance is supported for the perpendicular polarization.

The authors have proven that the resonances can be individually tuned and used to enhance the vibrational signal of thin protein layers. Another dual-resonant aperture is given by the geometry of a Jerusalem cross. Dual-band response is obtained by the superposition of the spectra of the constituting vertical and horizontal H-shaped apertures.<sup>189</sup>

Although the hitherto introduced concepts of dual-band nanostructures feature two resonances, which can be individually tuned to different resonance frequencies, they lack the possibility to enhance two spectrally separated vibrational bands of the very same molecule. The reason for this is that the above-mentioned concepts are based on the combination of two plasmonic constituents fabricated within one nanostructure. Therefore, the hot-spots of the different resonance frequencies are spatially separated, again requiring one to functionalize different hot-spots with the same molecular species. Routes to overcome this limitation are the use of higher order plasmonic excitations or broadband log-periodic trapezoidal antennas, already known from radio frequency technology.<sup>128</sup> The design is shown in Figure 16c together with the far-field extinction cross-section (shown in Figure 16d), which features four distinct resonances located in the mid-IR region. Each resonance is related to a pair of induced horizontal dipoles, which, in turn, induces a local vertical dipole.<sup>128,190</sup> The outstanding property of the log-periodic trapezoidal antenna is the near-field distribution, shown in Figure 16e, which concentrates the light at the same tip end for all resonances. Therefore, it is possible to enhance different vibrational modes of the very same molecules within a broad spectral range. This was demonstrated for AT-EG<sub>6</sub>-COOH self-assembled monolayers by evaluating five enhanced vibrational bands in a spectral window of  $3\text{ }\mu\text{m}$ , all showing enhancement factors exceeding  $10^5$ .<sup>128</sup> Furthermore, such log-periodic trapezoidal antennas enable simultaneous detection by surface-enhanced fluorescence, Raman spectroscopy, and infrared absorption, with relevant enhancement factors.<sup>128</sup>

**4.5.2. Post-Fabrication Tuning.** Another route to obtain broadband plasmonic enhancement is to tune the plasmonic resonances of particular nanostructures *in situ*. Recently, three different approaches for postfabrication tuning of plasmonic resonances have emerged. Plasmonic resonances can be tuned by, first, changing their geometry, second, changing the charge carrier density of the plasmonic material, and third, changing the refractive index of the surrounding material. Hereinafter, all three will be reviewed.

**4.5.2.1. Elastic Substrates.** Changing the geometry of plasmonic nanostructures is, for example, possible by fabricating them on compliant substrates, such as organic polymers. By applying tensile strain on the substrate, the arrangement and geometry of the structures thereon are slightly modified.<sup>131,191</sup> One example following this idea, introduced by Pryce et al.,<sup>131</sup> is illustrated in Figure 17a.

The authors fabricated double U-shaped split-ring resonators on top of a flexible polydimethylsiloxane (PDMS) substrate. This geometry is well-suited for tunable resonances, as the resonance frequency of the split-ring resonators strongly depends on their geometry. By applying strain, the outer SRR arms bend inward, increasing the coupling with the inner SRR, leading to a red-shift of the resonance. The spectral change together with SEM images depicting the change in geometry are shown in Figure 17b. Following this approach, it was possible to tune the resonance frequency over the C-H vibrational band provided by the PDMS substrate acting as a

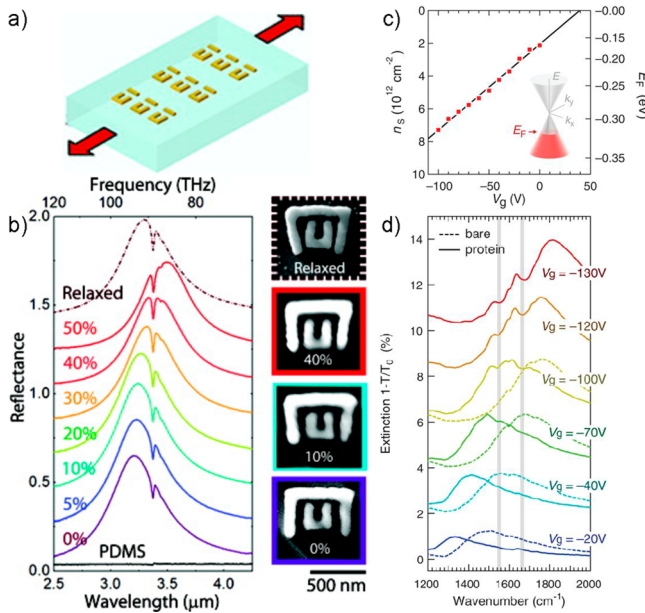


**Figure 17.** Postfabrication tuning of plasmonic nanostructures: (a) Illustration of tuning by stretchable substrates. The resonance frequency is tuned by applying tensile strain to the flexible PDMS substrate hosting double U-shaped split-ring resonators. (b) Reflectance spectra for tensile strains up to 50% together with corresponding SEM images visualizing geometrical changes. (c) Charge carrier concentration of graphene with dependence of the applied gate voltage. The plasmonic resonance frequency of graphene nanoribbons strongly depends on the charge carrier density as shown in (d) for several gate voltages. Fano-type line-shaped peaks on the plasmonic resonance are induced by a protein layer covering the graphene nanoribbons. The vertical gray stripes mark the amide 1 and amide 2 bands of the protein layer. (a) and (b) reprinted with permission from ref 191. Copyright 2010 American Chemical Society. (c) and (d) reprinted with permission from ref 171. Copyright 2015 AAAS.

SEIRA probe. Furthermore, the authors have shown that for up to 10% strain, the tuning is elastic in nature and becomes inelastic for higher values. However, inelastic deformation is also interesting for postfabrication tuning, as a bigger tuning range in the range of  $\Delta\lambda = 1 \mu\text{m}$  is accessible. In the experiments, strains as high as 50% without delamination or distortion of the metallic elements are observed.<sup>131,191</sup>

Whereas the above-mentioned experiment tunes the resonance frequency by employing near-field coupling, the same approach has been used by Aksu et al. to tune the resonance frequency by exploiting far-field coupling effects. By changing the periodicity of a nanoantenna array by applying tensile strain on a PDMS substrate, a slight shift of the resonance frequency of the collective excitation was observed. One drawback of this method is the use of elastic substrates (such as PDMS or parylene-C), which typically consist of organic polymers featuring vibrational excitations themselves. These vibrational lines might be difficult to distinguish from infrared excitations of target molecules.

**4.5.2.2. Graphene.** Another possibility to tune plasmonic resonances after fabrication is changing the properties of the plasmonic material. For example, graphene nanostructures fabricated on top of a silicon substrate covered with a  $\text{SiO}_2$ -layer can be used. By applying an electrostatic field across the  $\text{SiO}_2$  layer through a bias voltage, the Fermi level of the graphene is modified leading to a change in charge carrier

density, which linearly scales with the voltage (see Figure 17c). The experimental realization published by Rodrigo et al. is shown in Figure 17d.<sup>171</sup> By varying the voltage between 20 and 230 V, a resonance tuning between 1450 and 1800 cm<sup>-1</sup> was achieved and applied to sense the vibrational fingerprint of a thin protein layer. Together with the high spatial confinement and the high enhancement factor of graphene plasmons, this approach represents a promising SEIRA sensing platform, that is, for modulation spectroscopy.

**4.5.2.3. Phase Change Materials.** A change of the refractive index of the environment of plasmonic nanostructures can also be used for postfabrication tuning. Following this concept, a huge contrast in the refractive index within the IR spectral range, for example, provided by phase change materials, is required. A shift in resonance wavelength of 1  $\mu\text{m}$ , corresponding to a relative shift  $\Delta\lambda/\lambda = 10\%$ , has been reported by Kats et al. for nanostructures on top of a vanadium dioxide ( $\text{VO}_2$ ) layer.<sup>192</sup>  $\text{VO}_2$  provides a thermally driven insulator-to-metal phase transition at around 67 °C leading to significant changes in the refractive index.

Another interesting phase change material for plasmonic applications is germanium antimony telluride ( $\text{Ge}_3\text{Sb}_2\text{Te}_6$ , or short GST). It offers the possibility to optically, thermally, or electrically induce a phase-transition between an amorphous and a crystalline phase. This phase transition is related to a change in refractive index, allowing one to reversibly tune plasmonic resonances. Michel et al. have shown that this approach allows shifting the plasmonic resonance of aluminum nanoantennas for several hundred wavenumbers, corresponding to a tuning figure of merit (resonance shift over full width at half-maximum) of 1.03 by inducing the phase-transition by thermal annealing<sup>193</sup> with femtosecond laser pulses.<sup>194</sup> Thermally induced phase changes resulting in shifts of the resonance position of aluminum patches of more than 500 nm have also been demonstrated by Tittl et al.<sup>195</sup> However, even though the concept of phase change materials is promising for SEIRA applications, it has not been applied yet.

#### 4.6. Pushing the Detection Limit

The ultimate goal in resonant SEIRA is to spectroscopically detect and characterize single molecules attached to individual nanostructures. Besides a targeted delivery of molecules to the plasmonic hot-spots, this vision requires single particle spectroscopy, in particular, infrared microspectroscopy. However, already diffraction limited infrared microspectroscopy of single particles is challenging due to the low brilliance of thermal light sources (globar) commonly used in standard FTIR spectroscopy.<sup>196</sup> Consequently, the key to single molecule sensitivity is not only to maximize the SEIRA enhancement, but also to apply and develop advanced infrared light sources such as synchrotrons,<sup>197</sup> quantum cascade lasers (QCL),<sup>198</sup> or optical parametric light sources.<sup>199</sup> Combining plasmonic nanostructures with spatially resolved imaging techniques, such as s-SNOM,<sup>104,200,201</sup> photothermal induced resonance (PTIR),<sup>140,142</sup> or scanning tunneling microscopy (STM),<sup>202</sup> can help to overcome the targeted positioning of molecules in the antenna hotspot. Furthermore, SEIRA with nanometer resolution is enabled by the use of such techniques.

**4.6.1. Brilliant Light of Advanced Light Sources.** A good measure for the performance of a light source is the brilliance of the emitted radiation. As compared to typical thermal light sources for FTIR spectroscopy, IR synchrotron radiation is 3 orders of magnitude more brilliant, enabling

hyperspectral infrared chemical imaging at the diffraction limit as well as single particle spectroscopy.<sup>90,197</sup> Consequently, synchrotron radiation was applied to resonant SEIRA using single nanostructures. In early experiments, Neubrech et al. detected 100 000 ODT molecules (approximately 50 attograms) chemisorbed on a single gold nanowire.<sup>15</sup> Later, single nanorods and nanoslits functionalized with collagen-peptides and poly-L-lysine enabled the spectroscopic detection of approximately 5000 (~40 attograms) and approximately 7000 (~53 attograms) peptides, respectively. The latter experiments were performed in aqueous solution, maintaining the protein's physiological functionality and hence demonstrating the applicability of resonant SEIRA for studies of biological relevance.

The detection sensitivity can be further improved if highly brilliant radiation of an infrared laser is used as demonstrated by Steinle et al.<sup>203</sup> In the experiments, a fiber-feedback optical parametric oscillator (OPO) was coupled to a conventional FTIR spectrometer equipped with an infrared microscope. In comparison to thermal light sources, the femtosecond laser system emitted light with an approximately 4 orders of magnitude higher brilliance. Although the spectral bandwidth was limited (typically  $80\text{ cm}^{-1}$ ), it allowed for spectroscopy of single vibrational bands. Furthermore, the center wavelength was easily tunable in the spectral range between 2400 and 4700  $\text{cm}^{-1}$ . Employing such brilliant radiation, SEIRA studies of single gold nanostructures covered with an ODT monolayer were performed. As compared to infrared microspectroscopy utilizing synchrotron radiation, a significantly improved signal-to-noise in an approximately 10 faster acquisition time was achieved (Figure 18a–c). This superior performance enabled the detection of approximately 10 000 ODT molecules (~5 attograms) based on their enhanced  $\text{CH}_2$  vibrational bands.

In another study by Hasenkampf et al., a quantum cascade laser was applied to infrared spectroscopy and resonant SEIRA.<sup>205</sup> In contrast to the above-mentioned parametric concept, a QCL emits narrowband IR radiation (approximately  $1\text{ cm}^{-1}$ ) and hence requires a reliable and fast spectral tuning. As a demonstration, the authors acquired chemical maps of resonant nanoantennas as well as SEIRA spectra of nanoantennas covered with CBP. The spectroscopic data were recorded in a significantly reduced acquisition time as compared to studies with conventional thermal light sources, demonstrating the benefit of the QCL.

**4.6.2. Scattering Near-Field Optical Microscopy.** A further improvement of the SEIRA sensitivity in terms of localization can be achieved if nanostructures covered with molecules are investigated by infrared scattering near-field optical microscopy. Scattering SNOM allows for a laterally resolved infrared imaging with nanometer scale resolution and even near-field spectroscopy if broadband light sources are used.<sup>201,206</sup> Because of the possibility to distinguish different materials on the basis of their IR vibrations at wavelengths much smaller than the incident light, s-SNOM exhibits huge potential for applications. It was applied to near-field imaging of graphene plasmons,<sup>188</sup> chemical imaging of composition, domain morphologies, order/disorder, molecular orientation, or crystallographic phases,<sup>207</sup> and also resonant SEIRA by Hofmann et al.<sup>208</sup> By the use of a CO laser that emits narrowband IR radiation at distinct wavenumbers between 1650 and 1800  $\text{cm}^{-1}$ , near-field images of gold triangles covered with a poly(ethyl methacrylate) (PEMA) layer were acquired. Depending on the polarization of the incident light, different

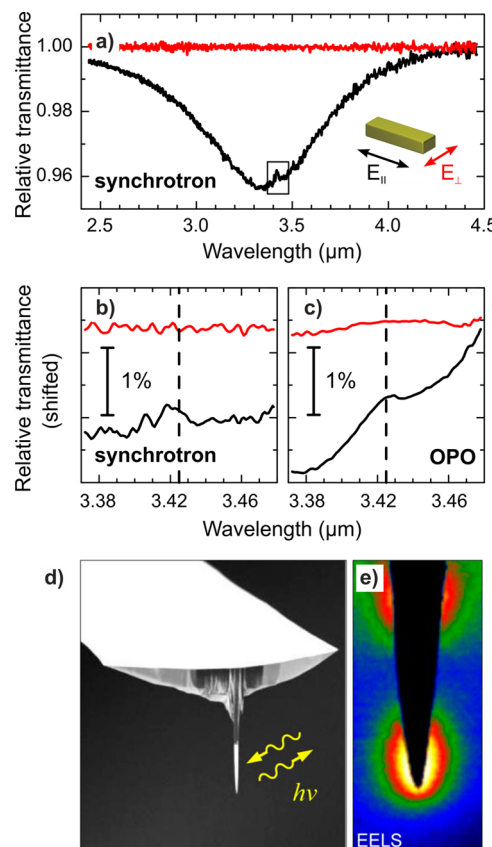


**Figure 18.** (a,b) Polarization-dependent SEIRA with a single ODT-covered nanoantenna illuminated by IR synchrotron radiation. The spectra close to the symmetric ODT vibration ( $3.425\text{ }\mu\text{m}$ , dashed line) acquired with the OPO (c,  $t = 17\text{ min}$ ) provide a significantly improved signal-to-noise ratio as compared to synchrotron studies (b,  $t = 170\text{ min}$ ). (d) A resonant gold tip is fabricated with focused ion beam milling and attached to the cantilever. (e) Electron energy loss spectroscopy (EELS) map of a FIB fabricated resonant antenna tip at the peak position in the energy loss spectrum. Adapted with permission from refs 203 and 204. Copyright 2015 Optical Society of America and 2012 American Chemical Society.

plasmonic hot-spots were generated. However, it should be noted that the plasmonic resonance is influenced by its interaction with the tip if no special detection schemes are applied, in particular if a metallized tip is used.<sup>209</sup> By tuning the laser over the enhanced  $\text{C=O}$  vibration of PEMA, a Fano-type line shape as a signature of resonant coupling was observed in analogy to far-field SEIRA spectroscopy. As compared to reference measurements on gold and other surfaces, the authors find only a slight increase of the vibrational signal strength, which may result from an imperfect tuning of the  $\text{C=O}$  vibration and the antenna resonance due to its interaction with the SNOM tip. According to the authors, also different orientation of the enhanced near-fields as compared to those predominantly probed by the tip may play a crucial role.

Even though s-SNOM enables near-field spectroscopy of nanometer-sized probes, a targeted delivery of molecules in plasmonic hot-spots remains a challenging task.<sup>210</sup> An elegant way to overcome this limitation is the use of metallic atomic force microscopy (AFM) tips with tailored resonant excitation instead of nanoantennas placed on a substrate (see Figure 18d and e). Following this approach introduced by Huth et al.,<sup>204</sup> the tip itself provides a plasmonic field enhancement required

for resonant SEIRA. Consequently, it allows for a flexible enhanced detection of molecules placed anywhere on the substrate and is not restricted to fixed hot-spots. Thus, a targeted delivery of molecules is no longer required. In good agreement with numerical simulations, the authors demonstrate an enhanced sensitivity as compared to nonresonant gold tips. An even higher sensitivity may be achieved if resonant tips are combined with a scheme such as that by Xu et al., where less than 1000 carbonyl groups were detected with s-SNOM operated by an optical parametric oscillator.<sup>211</sup> In such experiments, even single molecule sensitivity seems to be within reach.

In the aforementioned studies, tunable laser systems hamper broadband mid-IR spectroscopy. A combination of s-SNOM and synchrotron light sources, however, allows for accessing the entire infrared spectral range and consequently an unambiguous identification of molecular species.<sup>201,212</sup> Employing resonant nanoantennas in such advanced spectroscopic setups could enable broadband infrared spectroscopy on the nanometer scale with unprecedented sensitivity as preliminary studies indicate.<sup>207</sup>

## 5. FROM SEIRA TO STRONG COUPLING: PHONON POLARITONS

Resonant SEIRA is not restricted to sensing of organic or biologic molecules but offers also great potential for the detection of ultrathin layers of phononic materials. This was first demonstrated by Neubrech et al. by investigating nanoantennas fabricated on top of a 3 nm thick silicon dioxide ( $\text{SiO}_2$ ) layer supported by a silicon wafer.<sup>213</sup> The phononic  $\text{SiO}_2$  stretching vibration of the native  $\text{SiO}_2$  layer couples to the near-field of nanoantennas. In contrast to organic molecules, such as ODT, where the Fano-type peaks are detected at the molecular frequency (or transversal optical frequency, TO), the situation is more complex in case of ionic materials featuring strong oscillators with a negative real part of the dielectric function  $\epsilon(\omega)$ . The enhanced phononic signal of such materials was instead observed close to the longitudinal optical (LO) frequency, which is given by the maximum of the energy-loss function  $\text{Im}[-1/\epsilon(\omega)]$  and must be attributed to the excitation of a surface phonon polariton. This is in contrast to the simple idea of enhancing the signal of the  $\text{SiO}_2$  layer, because an excitation of the phonon polaritons under normal incidence is not possible without nanoantennas. Further experiments of antennas on  $\text{SiO}_2$ -substrates were carried out confirming this behavior.<sup>91,182</sup>

To gain deeper understanding of the interaction between plasmonic excitations of nanostructures and phononic excitations of thin ionic films, Huck et al. systematically studied plasmonic nanoantennas of different lengths located on  $\text{SiO}_2$  layers with various thicknesses.<sup>214</sup> First, the authors investigated nanoantenna arrays with different antenna lengths on top of an 8 nm  $\text{SiO}_2$  layer; experimental spectra are reprinted in Figure 19a.

Beside the antenna peak an additional peak close to the frequency of surface phonon polaritons (SPhPs) was found, which does not appear without the presence of nanoantennas. The appearance of this peak is explained by a hybridization of the antenna/ $\text{SiO}_2$  system, providing the momentum  $k_{\parallel}$  and the field component  $E_z$ , necessary for an excitation of phonon polaritons. For perfect agreement of plasmonic and phononic excitation energies, strong hybridization leads to the formation of a transparency window. This becomes more obvious in

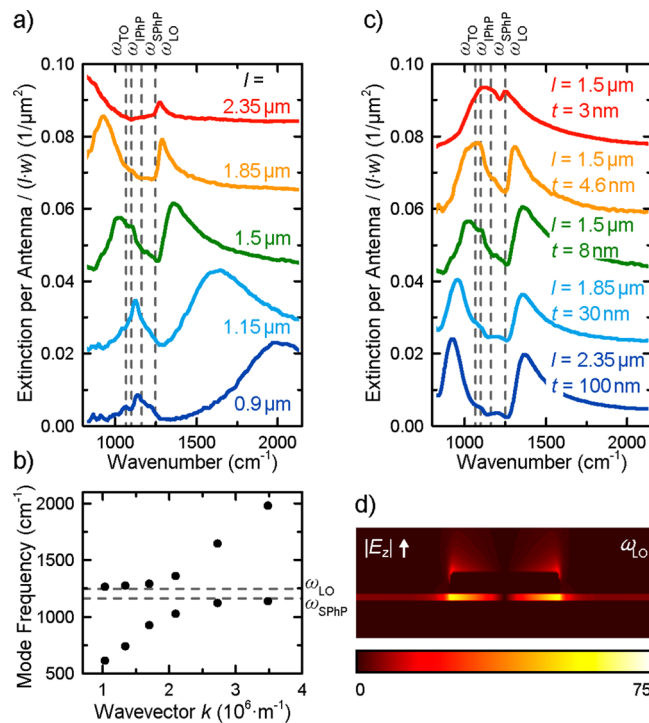


**Figure 19.** Strong coupling between phonon polaritons and plasmonic nanorods: (a) Extinction per antenna calculated from relative transmittance spectra of nanoantennas with different lengths  $l$  on top of a 8 nm thick  $\text{SiO}_2$  layer. (b) Resonance position of hybridized modes taken from (a) plotted versus the wavevector of the nanoantenna. (c) Extinction per antenna for different  $\text{SiO}_2$  layer thicknesses  $t$  as indicated in the figure. (d) The  $z$ -component of the simulated electromagnetic near-field of a resonantly excited nanoantenna on 30 nm  $\text{SiO}_2$ . The dashed lines in (a) and (c) indicate the spectral positions of the transversal optical (TO), longitudinal optical (LO), surface phonon polariton (SPhP), and interface phonon polariton (IPhP) frequency. Adapted with permission from ref 214. Copyright 2015 Optical Society of America.

Figure 19b, where the resonance positions of the hybridized system are plotted as a function of the wavevector of the nanoantennas. Furthermore, the evolution of this transparency window was investigated by fabricating nanoantennas coupled to  $\text{SiO}_2$  layers with increasing thickness. Thereby, a transition of a Fano-type peak for thin layers to a transparency window (strong coupling) starting at the LO frequency and extending to the SPhP frequency for thicker layers was observed (Figure 19c). The authors attribute the extension of the transparency window to the SPhP frequency to two reasons, the increased number of oscillators and the changes of the dispersion relation appearing for thicker layers. From a layer thickness of 30 nm on, a full transparency window is formed. Consequently, the antenna becomes invisible if it is coupled to an otherwise forbidden transition of  $\text{SiO}_2$  layer. This behavior can be comprehended by inspecting the near-field distribution of the hybridized system, shown in Figure 19d. At the LO frequency, where the transparency is reached first, the near-field is nearly completely confined inside of the  $\text{SiO}_2$  layer. The electromagnetic near-field is thus fully transferred to the phonon-polariton excitation, which cloaks the antenna.<sup>214</sup> A similar behavior was also reported by Shelton et al., using split-ring resonators coupled to a  $\text{SiO}_2$  layer.<sup>215</sup>

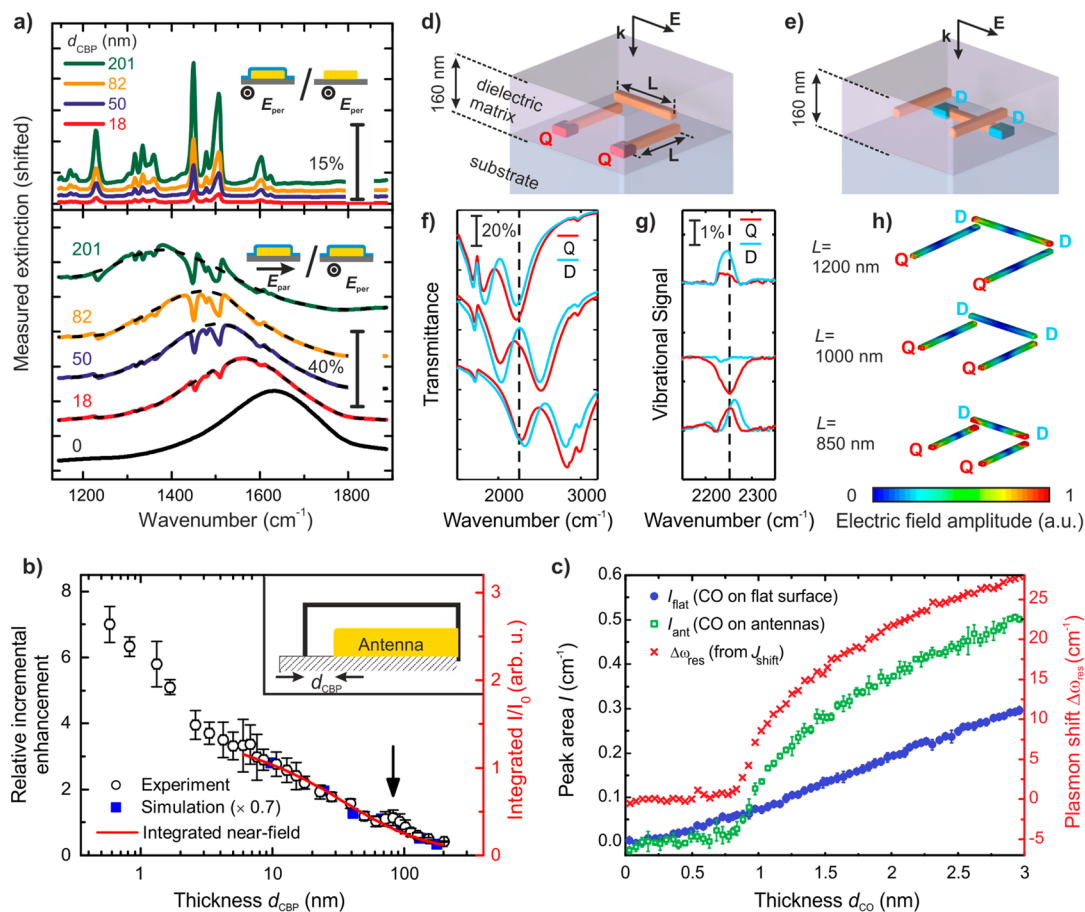


**Figure 20.** SEIRA for near-field mapping on the (a,b) nanoscale, (c) Ångström-scale, and of (d–h) buried plasmonic structures. (a) Measured extinction as deduced from the relative transmittance for selected thicknesses  $d_{\text{CBP}}$  given in nanometers (numbers, left). The inset (blue, CBP layer; orange, gold antennas; gray, substrate) indicates the respective normalization. Upper panel: For thick layers, several CBP vibrations are clearly visible in the spectra measured with light polarized perpendicular to the long wire axis and normalized to the bare substrate (see inset). Lower panel: To obtain the antenna-enhanced signal originating solely from molecules located in the plasmonic near-fields, the ratio of parallel ( $E_{\text{par}}$ ) and perpendicular ( $E_{\text{per}}$ ) transmittance is calculated (see inset). Besides the broadband antenna resonance, which shifts with thickness, enhanced vibrational CBP signals increasing with thickness are observed. The black dashed lines in the lower panel represent fits to the bare antenna resonance curves. Please note the different scales in the respective panels. (b) Relative incremental enhancement ( $(dI_{\text{enh}}/dd_{\text{CBP}})/(dI_{\text{ref}}/dd_{\text{CBP}})$ ) at a certain distance  $d_{\text{CBP}}$  from the antenna (the quotient of the derivatives of the enhanced ( $dI_{\text{enh}}/dd_{\text{CBP}}$ ) and unenhanced ( $dI_{\text{ref}}/dd_{\text{CBP}}$ ) for the C–H deformation vibration ( $\omega_{\text{vib}} = 1450 \text{ cm}^{-1}$ ) versus the layer thickness  $d_{\text{CBP}}$ . The simulated (blue symbols) data are normalized to the experimental ones (black symbols). The red curve represents the numerically calculated near-field intensity enhancement  $I/I_0$  summed over the surfaces of a cuboid defined by the antennas' geometry and the respective layer thickness at certain distance  $d_{\text{CBP}}$  (see inset). The inset depicts a cross-section, where the surface of the cuboid surface is sketched as a black line. The dashed area indicates the substrate. A good qualitative agreement between the decay of  $I/I_0$  and of the simulated and experimental increments is found from about 5 nm on with slight deviations around 80 nm (indicated by the black arrow). (c) Development of the carbon monoxide (CO) vibrational signal with growing layer thickness. Peak area (integrated from 2100 to  $2180 \text{ cm}^{-1}$ ) of the vibrational signal of CO on a flat gold surface ( $I_{\text{flat}}$ , blue), absolute peak area of the Fano-type signal of CO on the antennas ( $I_{\text{ant}}$ , green), and the shift of the plasmon resonance ( $\Delta\omega_{\text{res}}$ , red) are shown over the CO layer thickness  $d_{\text{CO}}$ . Please note the different ordinate offset. (d,e) Schematic view of the two-layer plasmonic structure embedded in a 160 nm thick dielectric matrix (PC403). Q (red) and D (blue) indicate the patch positions at the quadrupole and the dipole, respectively. (f) Transmittance spectra for increasing structure size (spectra shifted vertically) with the lower energy bright mode, the dark mode, and the higher energy bright mode tuned to the HSQ vibration, respectively. The spectral position of the HSQ vibration is indicated by the black dashed line. Red (blue) curve is the transmittance when the patches are positioned at the quadrupole (dipole). (g) Enhanced vibrational signals (baseline corrected) of HSQ for the three different modes with patches at the quadrupole (red curves) and dipole (blue curves), which is supported by the simulated electric field amplitude on the structure surface (h). Adapted with permission from refs 101 and 20. Copyright 2014 American Chemical Society and 2012 American Chemical Society. Adapted with permission from ref 18. Copyright 2013 Macmillan Publishers Ltd.: Nature Communications.

## 6. APPLICATIONS OF RESONANT SEIRA

Resonant SEIRA has great potential for applications, because it combines the specificity of infrared spectroscopy with the sensitivity provided by metal nanostructures. The improved sensitivity is of particular interest for applications in biology and biomedicine, where an identification of minute amounts of molecular species, sometimes laterally resolved, and a

monitoring of dynamic processes is required. However, resonant SEIRA is also applied to obtain information on plasmonic near-field distributions as discussed in the following.

### 6.1. Assessing Plasmonic Near-Fields

As discussed in section 3.4, the enhanced vibrational signal strength in resonant SEIRA scales with the squared electrical near-field of plasmonic structures. Knowing this relation,

infrared vibrations might be utilized as optical probes and thus offer an elegant way to obtain near-field distributions of plasmonic particles. While near-field distributions on the nanometer scale are easily accessible, for example, in s-SNOM studies,<sup>216,217</sup> field distributions of buried structures or in the Ångström-scale vicinity of metal particles are hardly accessible. Resonant SEIRA employing adequately chosen probe molecules can provide such information as will be discussed following. It should be noted that most of the experiments are performed with ensembles of nanoantennas resulting in averaged near-field properties of several nanostructures.

**6.1.1. Nanometer-Scale.** In 2014, the above-mentioned concept was applied to characterize plasmonic near-fields and SEIRA enhancements on the nanometer scale.<sup>101</sup> During the evaporation of the molecular probe CBP (approximate size:  $2 \times 1 \times 0.25 \text{ nm}^3$ ) on linear nanoantennas, *in situ* infrared spectroscopy was performed under high vacuum conditions. Polarization-dependent transmittance spectra were recorded for different average thicknesses ranging from 0 to 200 nm as exemplarily shown in Figure 20a.

For light polarized perpendicular to the long antenna axis, no plasmonic enhancement is present, and consequently a linear increase of vibrational signal strength with layer thickness is observed according to Lambert–Beer's law. For parallel polarization, however, a completely different behavior is found. First, the plasmonic resonance shifts toward lower energies with increasing layer thickness caused by the change of the polarizability of the antennas' surrounding. Second, the narrowband CBP vibrations are plasmonically enhanced and increase with layer thickness. To present this behavior in more detail, the incremental enhancement is calculated from the measured spectra (Figure 20b). It specifies the SEIRA enhancement at a certain distance, for example, at 10 nm away from the surface if no molecules are present at other distances. In agreement with numerical simulations, the experimental signal enhancement is strongest for the first nanometers and vanishes for distances larger than approximately 100 nm. With respect to sensing applications, this issue is of particular importance. Vibrations of larger molecules, such as proteins, bacteria or viruses, or molecules located far away from the antenna surface because of functional layers, will only be slightly enhanced.

Additionally, phononic excitations of  $\text{SiO}_2$  layers (see section 5) were used to probe the vertical near-field distribution of electrical fields produced by nanoantennas.<sup>218</sup> To demonstrate this, Nishimura et al. fabricated slot antennas on thin  $\text{SiO}_2$  films separated by  $\text{Al}_2\text{O}_3$  spacer layers with several thicknesses. As a result, the authors observed a decrease in  $\text{SiO}_2$ -signal with increasing  $\text{Al}_2\text{O}_3$  layer thickness, because the near-field overlap of the antennas with the  $\text{SiO}_2$  layer decreases.

**6.1.2. Ångström-Scale.** Molecular probes of smaller sizes provide a significantly improved spatial resolution. Using CO molecules (bond length of approximately 1.1 Å), Bochterle et al. investigated the distance dependence of electromagnetic fields normal to the antenna's surface with Ångström-scale resolution.<sup>20</sup> In the experiments, nanoantennas resonantly tuned to the CO stretching vibration at  $2139 \text{ cm}^{-1}$  were cooled to 20 K allowing for a cold condensation of CO. During the growth, *in situ* IR transmittance spectra were acquired, normalized to the bare antenna without any CO and corrected for the CO adsorbed on the substrate. Additionally, infrared reflection absorption spectroscopy (IRRAS) of CO adsorbed

on a flat gold film without any plasmonic enhancement was performed. From the transmittance and reflectance, respectively, the peak area of the CO vibration is extracted and plotted versus CO layer thickness in Figure 20c. As expected, a linear scaling is found for the IRRAS measurements according to Lambert–Beer's law. In contrast, the antenna-enhanced signals below 1 nm are suppressed and then rapidly increase for thicker layers. The authors relate this delayed absorption to quantum mechanical spill-out of the conduction electrons, suppressing the local near-field<sup>106</sup> and consequently the SEIRA enhancement on the first few Ångströms. The same behavior is found for the resonance shift with layer thickness, which is intrinsically connected to the signal enhancement via the plasmonic near-fields.

**6.1.3. 3D Mapping of Buried Nanostructures.** In the above-mentioned studies, only the field distribution normal to the surface is monitored. However, resonant SEIRA is also capable to access spatially resolved near-field distributions if selectively positioned molecular patches of nanometer dimensions are used.<sup>18</sup> Moreover, this approach is perfectly suited for accessing the near-field intensity of deeply buried plasmonic structures, which is a challenging task in s-SNOM due to the near-fields rapidly decaying with tip surface distance. As demonstration, Dregely et al. monitored the near-field intensity of a stacked EIT-plasmonic structure by positioning two patches of HSQ ( $200 \times 200 \times 30 \text{ nm}^3$ ) near the quadrupole (dipole) and a stacked dipole (quadrupole) on top of it (Figure 20d and e). Caused by the near-field coupling between the dipole and quadrupole, both excitations hybridize. Consequently, a low and a high energy mode (bright modes) with a transparency window between (dark mode) appear in the relative transmittance changing with length.<sup>219</sup> In Figure 20f, the red (blue) curve depicts the transmittance if molecular patches are placed on the dipole (quadrupole) acting as probe for the dipole (quadrupolar) near-fields. After a baseline-correction, the enhanced HSQ vibrational signal at  $2252 \text{ cm}^{-1}$  is obtained (Figure 20g). Obviously, the enhanced vibrations of the quadrupolar and dipolar fields are of equal strengths for the low energy bright mode. For the dark mode, a clear signal is found for the quadrupolar fields, whereas no signal is observed for the dipolar ones. Considering the high energy mode, the vibration enhanced by the quadrupolar fields is slightly stronger.

These experimental results are in good agreement with numerical near-field simulations of the plasmonic structure (Figure 20h). As is characteristic of the dark mode, the quadrupole is excited efficiently, whereas no dipolar mode is excited. As a consequence, stronger quadrupolar near-fields and hence stronger vibrational signal strengths are obtained. For the bright modes, stronger near-fields are found at the dipole as compared to the quadrupole, also in agreement with experimental observations. In summary, the incorporation of molecular probes in 3D buried nanostructures enables the mapping of plasmonic near-fields in all dimensions.

## 6.2. Hyperspectral Infrared Chemical Imaging

Hyperspectral imaging is also known as chemical or spectroscopic imaging. It combines conventional imaging (e.g., at a fixed wavenumber) and spectroscopy to attain both spatial and spectral information from an object.<sup>220,221</sup> Particularly, hyperspectral infrared chemical imaging is ideally suited for label-free and spatially resolved characterization of molecular species. Often, this approach is combined with FTIR

microspectroscopy and focal plane array (FPA) detectors to assess inhomogeneous material distributions on the micrometer scale with diffraction limited resolution.<sup>196</sup> The method is applied in biology and medicine to distinguish between healthy tissues and tumors of unstained biological tissue sections.<sup>6,205</sup> However, due to the intrinsically low infrared absorption cross-sections, hyperspectral infrared chemical imaging of nanometer-thick samples is out of reach. On the one hand, the use of a more brilliant laser light source, for example, quantum cascade lasers, is beneficial with respect to sensitivity, but on the other hand suffers from narrowband emission preventing hyperspectral imaging.<sup>222–225</sup>

In contrast, resonant SEIRA provides broadband enhancement, for example, in the molecular fingerprint region, and enables hyperspectral infrared chemical imaging as first demonstrated by Chen et al.<sup>16</sup> Using a FPA detector, the authors imaged vibrational bands of poly(methyl methacrylate) (PMMA) and in another experiment human cervical cancer cells attached to resonant plasmonic nanostructures. Kühner et al. extended this concept to detect different vibrational bands of various materials, which are enhanced by single or multi-resonant structures.<sup>17</sup> As schematically depicted in Figure 21a, micropatterns of C<sub>60</sub> and pentacene with 30 nm thickness were prepared on tailored gold nanostructures by stencil mask lithography.

Spatially resolved infrared spectra of the microstructured sample were acquired with an FPA detector ( $64 \times 64$  pixels) attached to an infrared microscope. Figure 21b shows such representative relative transmittance spectra of areas with bare nanostructures and areas of antennas covered with C<sub>60</sub> and pentacene. Because of the adsorption of the molecules on nanoantennas, the polarizability of the surrounding media changes, which can be utilized for refractive index sensing.<sup>8,105</sup> Hence, the plasmon resonance is shifted toward lower energies. A spatially resolved plot of this shift is shown in Figure 21c (plasmon image or refractive index image). Dark areas indicate a red-shifted plasmon resonance and correspond to C<sub>60</sub> and pentacene covered areas, respectively. The positions of the respective micropatterns obtained in this way are in perfect agreement with results from visible microscopy depicted by dotted lines. However, even though refractive index imaging allows for a localization of molecules, the detection is material-unspecific, meaning that C<sub>60</sub> and pentacene cannot be distinguished.

In contrast, SEIRA enables a material-specific discrimination between materials based on the specific vibrational bands as demonstrated for pentacene and C<sub>60</sub>. Upon inspection of Figure 21b, the enhanced vibrational bands of the respective molecules appear as modulation on the plasmon resonance. After a baseline correction, the enhanced signal strengths are extracted and spatially plotted, resulting in the infrared chemical images shown in Figure 21d and f for C<sub>60</sub> (1430 cm<sup>-1</sup>) and pentacene (1300 cm<sup>-1</sup>). Obviously, the pentacene (C<sub>60</sub>) microstructures are clearly visible if the signal strengths are evaluated at 1300 cm<sup>-1</sup> (1430 cm<sup>-1</sup>), whereas no C<sub>60</sub> (pentacene) micropatterns appear if the signal strengths are evaluated at 1300 cm<sup>-1</sup> (1430 cm<sup>-1</sup>). In contrast, no molecular signature and consequently no micropatterns are visible in the chemical images extracted from reference measurements without any plasmonic enhancement (perpendicular polarization) as shown exemplarily for pentacene in Figure 21e. Both results clearly demonstrate the significant advantage of resonant SEIRA over conventional hyperspectral infrared chemical

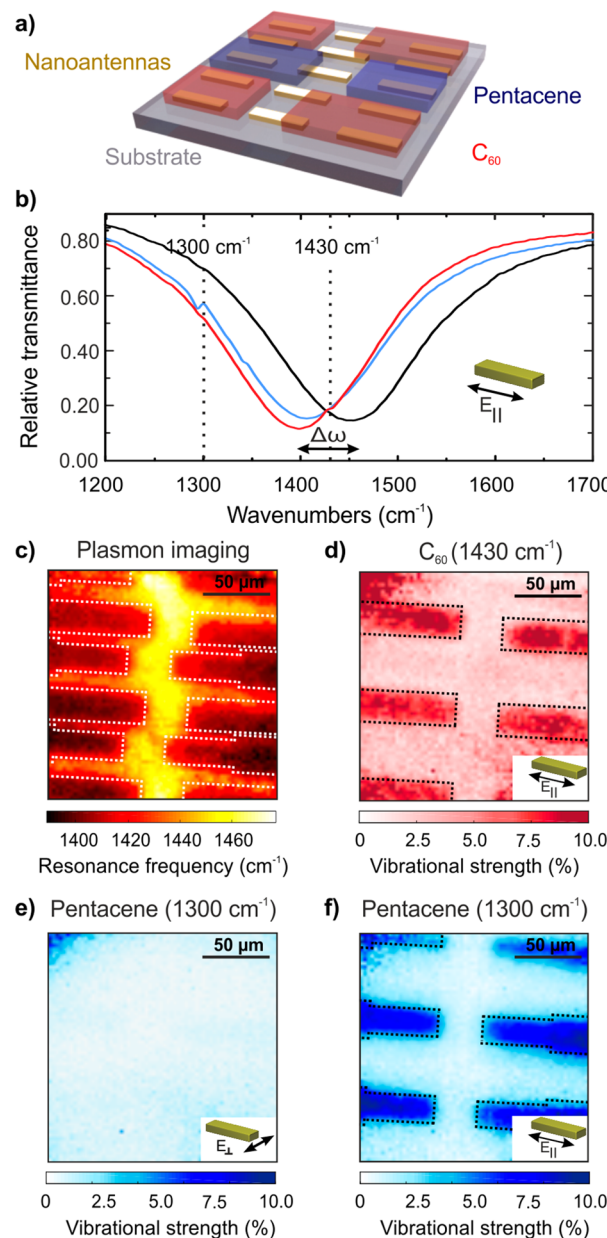


**Figure 21.** (a) Schematic illustration of nanoantennas covered with pentacene and C<sub>60</sub>. (b) Representative plasmon resonances of bare nanoantennas (black curve) are shifted ( $\Delta\omega$ ) with respect to nanostructures covered with 30 nm of pentacene (blue) and C<sub>60</sub> (red), respectively. The molecular vibrations of pentacene (1300 cm<sup>-1</sup>) and C<sub>60</sub> (1430 cm<sup>-1</sup>) are enhanced if the electrical field is polarized parallel to the long antenna axis ( $E_{||}$ , see inset). The dashed lines indicate the strongest molecular vibrations used for chemical imaging. (c) Plasmon imaging: The plasmonic resonance frequency is plotted for each detector pixel. Uncovered areas appear bright and can be distinguished from covered ones. However, a material-specific identification of pentacene and C<sub>60</sub> is not possible. Chemical imaging of (d) C<sub>60</sub> and (f) pentacene: Vibrational signal strength at 1430 cm<sup>-1</sup> (1300 cm<sup>-1</sup>) for parallel polarization plotted for each detector element. Only if the vibrational signals are enhanced (parallel polarization) can the C<sub>60</sub> and pentacene areas be identified. (e) For perpendicular polarization, no signals are found as was exemplarily shown for pentacene. Dashed lines in (c), (d), and (f) indicate the positions of the microstructured pentacene and C<sub>60</sub> areas, which can be clearly distinguished in the chemical images.

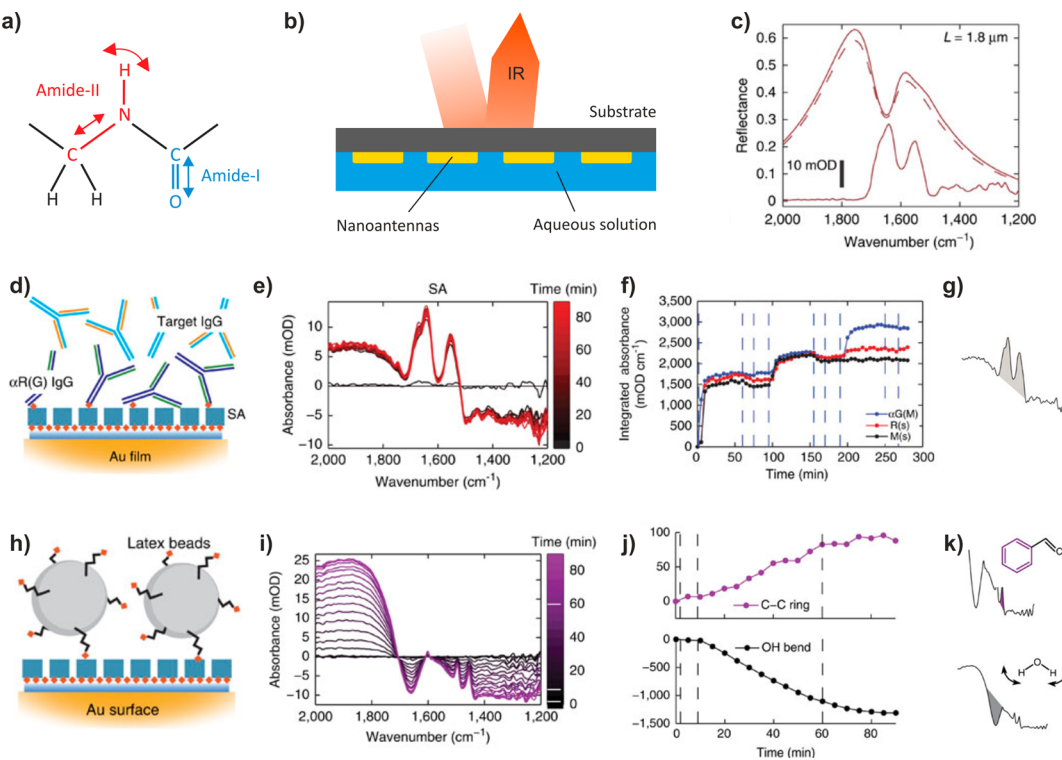


**Figure 22.** (a) Molecular structure of the amide group and vibrational modes as indicated by arrows. (b) Schematic illustration of the plasmon internal reflection (PIR) (not to scale). (c) Reflectance spectra before (dashed) and after (solid) streptavidin (SA) binding for the  $L = 2.2 \mu\text{m}$  antenna array sampled in an aqueous media. The absorbance is displayed at the bottom of the panel (solid line) with units indicated by the scale bar. (d) Schematic of protein-binding interactions measured. The gold antennas (Au film) are covered with a self-assembled monolayer of a biotin-labeled alkanethiol (blue and red dots), to which SA binds. They are further functionalized with  $\alpha\text{G(M)}$  IgG, which allows for a selective adsorption of the respective target IgG (see text). (e) Time series of spectra taken during SA. (f) Peak integral (integrated absorbance) evolution over time during the protein-binding measurements for the three samples. Abbreviations are as follows:  $\alpha\text{G(M)}$ , antigoat (mouse host) IgG; R(s), rabbit IgG; M(s), mouse IgG. Vertical lines indicate the rinsing process. In all experiments, for each step the protein solution is introduced and allowed to flow for 60 min (first horizontal line). Each step is followed by a 15 min rinse with a detergent (second vertical line), then pure buffer (third vertical line). (g) Amide band peak integral used to assess protein binding. (h) Schematic of the biotin-labeled latex bead ((b)LB)–SA binding (compare labeling in (d)). (i) Time-series absorbance spectra during the (b)LB-binding steps. The vibrational features at  $1450$  and  $1490 \text{ cm}^{-1}$  are associated with the benzene ring; the vibrational feature at  $1650 \text{ cm}^{-1}$  originates from the OH vibration in  $\text{H}_2\text{O}$  (see also (k)). (j) Evolution of the peak integrals (integrated absorbance, units of mOD ( $\text{optical density}$ )  $\text{cm}^{-1}$ ) over time during (b)LB-binding steps. Vertical dashed lines indicate the rinsing process. For details, see ref 22. (k) Specific chemical structures and their corresponding infrared fingerprints (peak integrals) used to monitor their presence during the flow experiments. Reprinted with permission from ref 22. Copyright 2013 Macmillan Publishers Ltd.: Nature Communications.

imaging in terms of sensitivity and over refractive index imaging in terms of specificity. Kühner et al. further improved this approach by employing nanocrosses with dual band plasmonic enhancement.<sup>17</sup> The use of such tailored structure enables infrared chemical imaging in the fingerprint region and simultaneously in the region between  $2500$  and  $4000 \text{ cm}^{-1}$ , where mainly stretching vibrations of single and double bonds are located.

### 6.3. Sensing of Proteins

Besides an unambiguous and material-specific identification of molecular substances, infrared spectroscopy and thus resonant SEIRA allow for a label-free structural investigation of chemical compounds. This is of particular interest in biology and biomedicine for a detailed analysis of protein binding events or for the determination of their conformational states, which are crucial for the protein functionality.<sup>7</sup> Incorrectly folded proteins may lose their functionality and are suspected to cause neurodegenerative diseases such as Alzheimer's or Creutzfeldt–Jakob disease.<sup>226</sup> In typical IR studies, the identification and structural analysis of the respective proteins are predominantly carried out on the basis of the amide I (mainly

C–O stretch) and amide II (combination of C–N stretch and N–H wagging) vibrations located around  $1650$  and  $1450 \text{ cm}^{-1}$  (see Figure 22a). Consequently, proteins are often applied as model systems in resonant SEIRA to demonstrate the capability of resonant SEIRA for ultrasensitive detection and monitoring of binding events.

**6.3.1. Detection of Proteins.** Minute quantities of silk fibroin<sup>83</sup> and bovine serum albumin,<sup>227,141</sup> often used as a protein concentration standard in lab experiments, were detected on the basis of their enhanced amide bands. In other experiments, layers of streptavidin and specially designed peptides,<sup>228,229</sup> bilayers of protein (A/G) and immunoglobulin (IgG),<sup>87,152,158,171,230</sup> and low quantities of ferritin,<sup>129</sup> a spherical protein complex that has its main function in cellular iron storage, were adsorbed on nanostructures and identified using resonant SEIRA. Beyond the detection of proteins itself in most of the above-mentioned experiments, the proteins act as molecular probes to characterize properties of the SEIRA structure in use. In further experiments, the formation of a bilayer consisting of protein and immunoglobulin on resonant nanoantennas was detected, demonstrating the capability of SEIRA to identify binding events of proteins ex situ.<sup>22</sup>

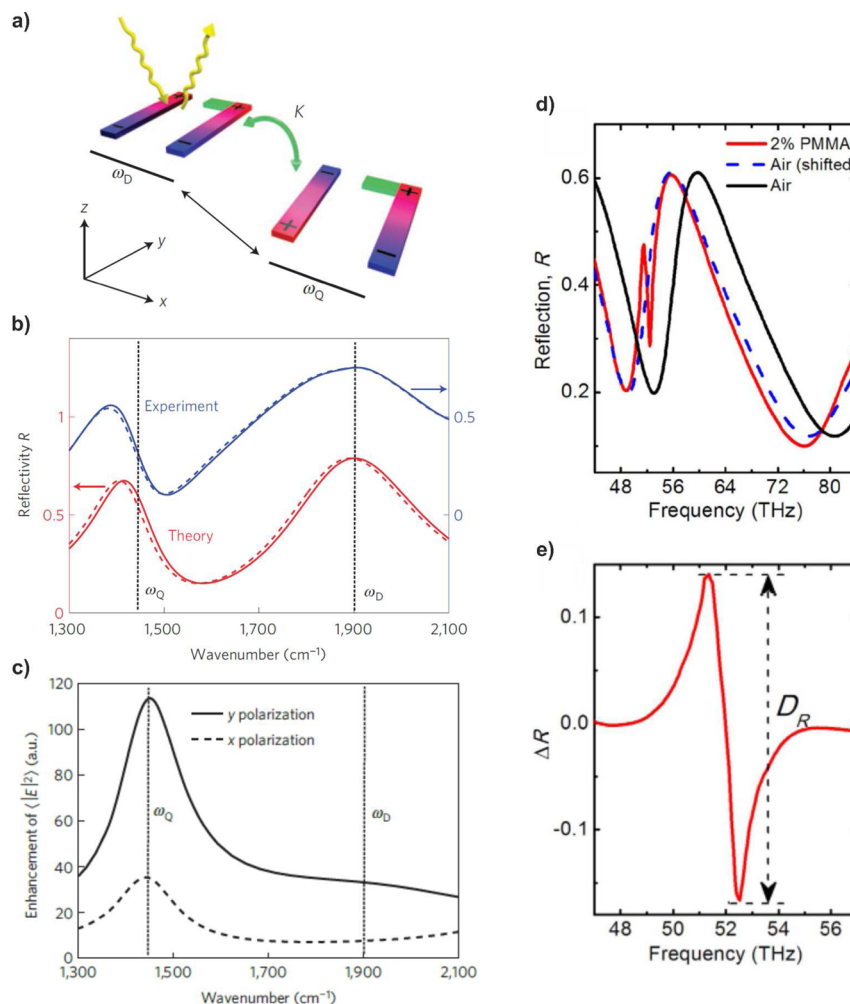


**Figure 23.** (a) Schematic illustration of Fano-coupling in a plasmonic metamaterial. The superradiant dipolar mode with resonance frequency  $\omega_D$  gets excited by incident light and couples to the subradiant quadrupole mode at  $\omega_Q$  with the coupling constant  $k$  via the plasmonic near-fields. (b) Typical experimental and theoretical reflectivity spectra of a FRAMM before and after functionalization with a protein A/G monolayer. (c) Near-field enhancement in a theoretical 10 nm thick layer on the FRAMM obtained from numerical (finite-element) simulations for  $x$ - and  $y$ -polarization of the light. (d) Reflectance spectra of a Babinet-inverse FRAMM structure (slits in a 25 nm thick Au layer) before (black) and after coating of PMMA molecule layer (blue, red) in a frequency range from 1467 to 2802 cm<sup>-1</sup>. (e) Difference of reflectivity  $\Delta R$  of the spectra shown in (d) with indicated signal strength  $D_R$  in the frequency range from 1568 to 1901 cm<sup>-1</sup>. Reprinted with permission from refs 230 and 237. Copyright 2012 Macmillan Publishers Ltd.: Nature Materials and 2015 Macmillan Publishers Ltd.: Nature Materials.

**6.3.2. Fano-Resonant Asymmetric Metamaterials.** In 2011, Wu et al. utilized a combination of refractive index sensing and resonant SEIRA to detect proteins.<sup>230</sup> Because of the dependence of plasmons on the dielectric function of the surrounding medium, refractive index sensing is another promising application of plasmonic metamaterials.<sup>154,231,232</sup> In 2011, Pryce et al. used coupled split-ring resonators as substrates for SEIRA and refractive index sensing, demonstrating how both applications can be combined on the same substrate.<sup>131</sup> In other studies, nanoporous gold disks were used.<sup>233</sup> In refractive index sensing, the shift of the plasmonic resonance is monitored, which makes its sensitivity directly dependent on the used line width. In addition, a narrow resonance corresponds to low damping and long plasmon lifetimes resulting in high near-field intensities required in resonant SEIRA. Thus, spectrally narrow line widths are desirable for both applications. One approach to obtain such narrow band resonances providing high near-fields is the use of so-called Fano-resonant asymmetric metamaterials (FRAMMs).<sup>234–236</sup> Fano-type resonances have already been

described in section 3.3 for a coupled system consisting of a plasmon resonance and a molecular excitation. However, they also appear in merely plasmonic metamaterials when coupling a bright (superradiant) to a dark (subradiant) mode of the plasmonic system. Figure 23a illustrates this for a structure of two parallel antennas oriented along the  $y$ -axis, coupled via a third antenna, oriented along the  $x$ -axis. Such a structure exhibits no in-plane inversion or reflection symmetry, making it an asymmetric metamaterial.

Such FRAMMs were used in 2011 by Wu et al. as a biosensor.<sup>230</sup> In Figure 23b are plotted typical reflectance spectra of the used FRAMMs before and after functionalization with 3 nm-thick protein A/G monolayer. The resonance of the superradiant mode  $\omega_D$  is located around 1900 cm<sup>-1</sup>. Going to lower frequencies, a well-pronounced dip is visible, which is a signature of the destructive interference between the two coupled modes. After functionalization with a monolayer of a material with a permittivity  $\epsilon > 1$ , the Fano-resonance shifts toward lower energies. Using temporal coupled mode theory for the analysis of this shift, the authors precisely determined

the thickness of the monolayer and draw conclusions regarding the protein orientation by taking the anisotropy of the permittivity into account. For these experiments, the narrow nonradiative resonance of the quadrupole mode located at  $\omega_Q$  (see Figure 23b) has to be detuned from any vibrational modes of the molecules as the permittivity is highly dispersive in their spectral vicinity. However, by matching  $\omega_Q$  to the vibrational modes, FRAMMs can be used for SERA because the highest near-field intensities are present at the quadrupole resonance as shown in Figure 23c. In a similar study, Cheng et al. found enhancement factors of  $10^5$  using Babinet-inverted FRAMM structures, which impressively prove the potential of this approach.<sup>237</sup> In other studies, FRAMMs were employed to successfully distinguish between a monolayer of vertically and horizontally aligned helical peptides based on their amide I and amide II bands.<sup>228,229</sup>

**6.3.3. In Situ Monitoring of Protein Binding Dynamics.** Resonant SEIRA spectroscopy in all of the above-mentioned studies was performed under atmospheric conditions outside the proteins native environment. As a consequence, the proteins often change their structural properties or lose their physiological functionality hampering applications of resonant SEIRA to biological relevant systems at that stage. Consequently, SEIRA spectroscopy in aqueous solution is essential but hindered by the strong absorption of water in the infrared, particularly at the amide vibrations. Adato et al. overcame this obstacle by leveraging tailored arrays of nanostructures not only to enhance the proteins vibrations but also to redirect far-field radiation.<sup>25</sup> This concept, referred to as plasmonic internal reflection (PIR, see Figure 22b), has similarities to attenuated total reflection (ATR), which is conventionally applied to reduce the water absorption in IR spectroscopy.<sup>196</sup> In this traditional approach, IR radiation is totally reflected at the ATR crystal–water interface, and only molecules located in the evanescent field (with micrometers spatial extent) are probed. In contrast, resonantly excited nanoantennas as used in PIR provide a much stronger confinement of the electromagnetic fields (only 100 nm), as discussed previously.<sup>101</sup> Consequently, the water absorption is further reduced if the protein is located in the confined near fields. Importantly, this approach requires a tailored design of the scattering cross-sections of the resonant nanoantennas to efficiently redirect the far-field radiation to the detector.<sup>187</sup>

Adato et al. utilized this advanced geometry to measure in real-time molecular interactions between proteins as well as chemically distinct particles. In a first series of experiments, the authors studied the protein interaction as schematically illustrated in Figure 22d. First, the nanostructures were functionalized with a layer of streptavidin (SA). Figure 22c shows a typical infrared reflection spectrum measured in PIR geometry of nanoantennas before and after adsorption of SA. The infrared optical response is dominated by the broadband plasmonic response and the remaining water absorption present in both spectra. The enhanced amide vibrations, however, are hardly visible but clearly appear in the differential absorbance spectra shown in Figure 22e. For each time step, the respective spectrum is referenced to the spectrum taken directly before the protein solution is introduced to the system. Obviously, the signal strength of the amide vibrations increases with time and saturates at a certain step, indicating the full coverage of the antennas with the SA layer. The saturation is also seen in Figure 22f (between 0 and 90 min), where the integrated absorption of the amide vibrations in units of milli

optical density times wavenumber ( $\text{mOD cm}^{-1}$ ) is plotted versus time.

For the demonstration of protein–protein binding, experiments with three different IgGs (antigoat (mouse host) ( $\alpha\text{G(M)}$ )), rabbit IgG (R(s)), and mouse IgG (M(s))) were performed. In all three experiments, first, a second layer consisting of biotin-labeled antirabbit (goat host) ( $\alpha\text{R(G)}$ ) was attached to the SA (at time step 90 min), acting as a receptor for  $\alpha\text{G(M)}$  and R(s). Because of the amide vibrations of the  $\alpha\text{R(G)}$ , the integrated absorption increases in all experiments. At a time step of 190 min  $\alpha\text{G(M)}$ , R(s) or M(s) was added to the respective samples.<sup>25</sup> By monitoring the integrated absorbance over the material-specific vibrational bands found in the respective differential absorbance spectra (see Figure 22f), the binding events were tracked. In the study, the absorbance of amide I and II vibrations can be used as proxy for protein accumulation. Consequently, the trace shows the successful binding of  $\alpha\text{G(M)}$  to  $\alpha\text{R(G)}$  in situ monitored with resonant SEIRA (blue curve in Figure 22f). As expected, if other target IgGs are added to the system (at time step 190 min), the binding is hindered (rabbit IgG (R(s)), red curve in Figure 22f) or completely suppressed (mouse IgG (M(s)), black curve in Figure 22f).

In a second series of experiments, Adato et al. monitored the binding interactions between two chemically distinct species, proteins and biotin labeled latex beads (Figure 22h). While both materials, latex beads and proteins, have similar refractive indices in the visible and near-infrared, making them indistinguishable in refractive index sensing studies, their molecular constitution is completely different. In contrast to the protein streptavidin, styrene contains no amide bonds but narrow vibrational bands at 1490 and  $1450 \text{ cm}^{-1}$  associated with the benzene ring (Figure 22h). After introducing biotin labeled latex beads into the system, such benzene vibrations appear in the differential absorption recorded in PIR geometry (Figure 22i). The localization of the latex-beads in the enhanced electromagnetic near-fields of the resonant nanoantennas covered with streptavidin is mediated by the biotin–streptavidin binding. Similar to the above-mentioned results, the integrated absorbance of the benzene vibrational band is calculated enabling an in situ monitoring of the biotin–streptavidin binding. Additionally, a broad feature at  $1650 \text{ cm}^{-1}$  is found in the differential absorption spectra, which decreases with time (see also integrated absorbance in Figure 22j, lower panel). The authors relate the reduction in intensity to the water displacement as the beads bind at the nanoantennas surface.

These results clearly highlight the capability of resonant SEIRA in PIR geometry to distinguish and track chemically distinct substances on the basis of the bond specific binding.

#### 6.4. Real-Time Monitoring of Lipid Membranes

For a full understanding of biological systems, it is essential to monitor their dynamics under varying conditions. In a first study, Bagheri et al. demonstrated that resonant SEIRA is suitable to trace such dynamic processes. In the experiments, the degradation of a polymer was monitored by detecting the decrease of its characteristic SEIRA signal after certain periods of UV exposure.<sup>86</sup>

In a recent work of more biological relevance by Limaj et al., this concept was applied to a biological testing system, the so-called lipid membranes.<sup>21</sup> Bilayers of these membranes constitute the surface of all living cells. As such they mediate

between the environment inside and outside of the cell<sup>238</sup> and therefore play an important role in any organism. As illustrated in Figure 24a, the authors used a biosensor based on resonant SEIRA, consisting of gold nanoantennas covered with a layer of silica ( $\text{SiO}_2$ ).

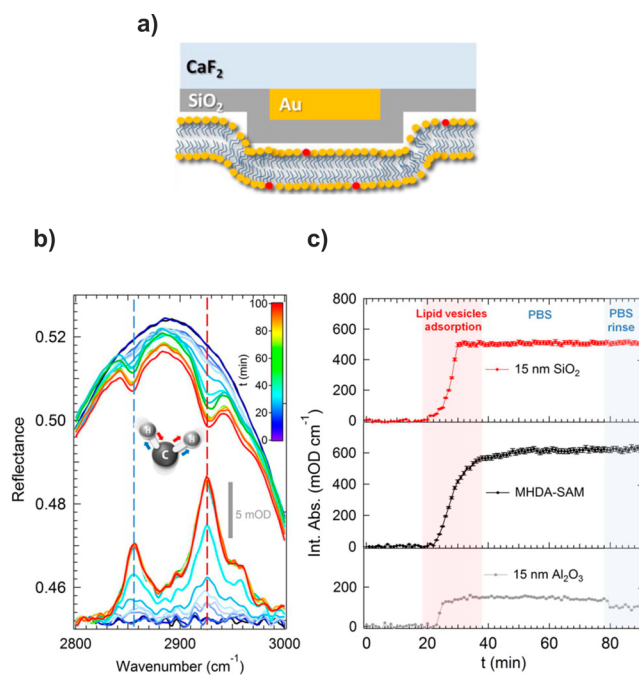


**Figure 24.** (a) Schematics of measurement configuration for monitoring supported lipid bilayers (SLB) formation. (b) Reflectance (top) and corresponding absorbance (bottom) spectra for different times during SLB formation. Inset illustrates the symmetric (blue) and antisymmetric (red)  $\text{CH}_2$  stretch modes of the lipids. Their spectral position is indicated by the dashed lines of respective color. (c) Integrated absorbance over  $\text{CH}_2$  modes as a function of time for nanoantennas covered with a 15 nm thick  $\text{SiO}_2$  layer (top), a self-assembled monolayer of 16-mercapto hexadecanoic acid (MHDA) (middle), and a 15 nm thick  $\text{Al}_2\text{O}_3$  layer (bottom). Differently colored regions indicate injection of lipid vesicles, injection of phosphate buffer saline (PBS), and rinse with PBS at a higher flow rate. Reprinted with permission from ref 21. Copyright 2016 American Chemical Society.

This layer was necessary to enable a homogeneous formation of the supported lipid bilayers (SLB) on the sensor surface. The measurements were performed *in situ* in the aqueous environment inside of a fluidic cell. Lipid vesicles were injected into the cell and adsorbed to the biosensors surface until a critical coverage was reached upon which they ruptured and formed the SLB. This formation was monitored by observing the two  $\text{CH}_2$  absorption bands of the lipids located at 2855 and 2927  $\text{cm}^{-1}$ . Figure 24b shows reflectance spectra and vibrational signals for different times after the lipid vesicle injection. It is clearly visible how the vibrational signals increase over time, which can be associated with the formation of the SLB. To better analyze the kinetics, the authors integrated the absorbance of these two bands and plotted them as a function of time. As seen in Figure 24c for three different surface materials, distinctly different profiles were recorded. For a self-assembled monolayer of 16-mercapto hexadecanoic acid (MHDA), the formation dynamics exhibit a decelerating profile (Figure 24c, middle panel), which the authors attributed to the strong interaction between lipid vesicles and the MHDA. This

interaction results in a reduced mobility and therefore decreasing coverage speed, as more sites on the surface become occupied. For  $\text{Al}_2\text{O}_3$  a profile similar to that for  $\text{SiO}_2$  was found, however, with a distinctly lower SEIRA signal (Figure 24c, bottom panel). In addition, the signal is not stable over time and decreases upon rinsing with phosphate buffer saline (PBS). Those two effects are expected due to the low adhesion energy of the vesicles on  $\text{Al}_2\text{O}_3$ . A stable bilayer can therefore not be formed on this surface as the biosensor was able to correctly detect. This demonstrates impressively the capability of biosensors based on resonant SEIRA to trace the formation kinetics of biological processes in real time and thus its applicability to further analyze structure, functions, and interactions of cellular membranes.

## 7. CONCLUSION AND OUTLOOK

Surface-enhanced infrared spectroscopy using resonant metal nanoantennas has grown in scientific and technological relevance from a fundamental effect to practical applications. From the first demonstration of resonant SEIRA to elaborated studies of the vibrational signal enhancement and the underlying resonant coupling between molecular and plasmonic excitations, the understanding has increased substantially. As a result of these experimental and theoretical efforts, a foundation has evolved that provides an intuitive physical insight into resonant SEIRA and gives design rules for metal nanostructures used in SEIRA applications.

On the basis of this fundamental knowledge, several routes for an optimization of the signal enhancement have been developed. It turned out that a careful design of the nonradiative plasmonic losses (given by the nanostructure materials) and the radiative plasmonic losses (given by the nanostructure shapes and arrangements) is crucial for the enhancement. These parameters, together with the antennas' nanoscopic properties, provide versatile possibilities for an optimized design of nanostructures that can be adapted to any given experimental requirement. Such optimized nanoantennas are likely to serve as substrates for surface-enhanced infrared spectroscopy with single molecule sensitivity if highly brilliant light of advanced light sources or combinations with near-field optical microscopy are employed.

Even though single molecule sensitivity has not been reached yet, resonant SEIRA has huge potential for applications in several fields of research and industry. For instance, dynamic processes such as the formation of planar biomimetic membranes have been monitored, or biomolecules and proteins have been detected without any chemical functionalization, demonstrating the capability for label-free and nondestructive material identification with unprecedented sensitivity. Combinations of resonant SEIRA with refractive index sensing and other field-enhanced techniques, such as enhanced fluorescence or SERS, have led to the design of nanoscale sensing platforms providing complementary chemical information.

In conclusion, while in the past a fundamental understanding of the physics underlying resonant SEIRA was gained and first applications were demonstrated, resonant SEIRA is now developing toward a standard technique for the detection of molecular vibrations with improved sensitivity. In the future, the challenge remains to detect gases, protein folding events in their native liquid environment, as well as single molecules, ideally in an intracellular fashion. The latter one could be achieved with nanoparticles or core–shell nanoparticles in an aqueous environment, which can be tuned toward the mid-IR,

particularly if they are made from materials other than gold, for example, titanium nitride, and so can semiconductor nanoparticles. This should aid resonant plasmonic SEIRA enhancement also in cells with typical sizes of several tens of micrometers.

## AUTHOR INFORMATION

### Corresponding Author

\*E-mail: neubrech@kip.uni-heidelberg.de.

### ORCID

Frank Neubrech: 0000-0002-5437-4118

Ksenia Weber: 0000-0002-9836-8457

Annemarie Pucci: 0000-0002-9038-4110

### Notes

The authors declare no competing financial interest.

### Biographies

Frank Neubrech is a postdoctoral research associate working with Professor Harald Giessen at the 4th Physics Institute at Stuttgart University, Germany, and since 2016 with Professor Na Liu at the Kirchhoff Institute for Physics at the University Heidelberg, Germany. He received his Ph.D. in Physics from Heidelberg University in 2008 under the supervision of Professor Annemarie Pucci. In 2012 he joined Professor Harald Giessen's group after a postdoctoral position at Heidelberg University. His main research interests include surface-enhanced infrared spectroscopy, infrared spectroscopy, and plasmonics.

Christian Huck is a postdoctoral researcher working in Prof. Pucci's group at the Kirchhoff Institute for Physics at Heidelberg University. He received his Ph.D. in Physics from Heidelberg University in 2015 under the supervision of Professor Annemarie Pucci. His main research interests include the fabrication and numerical simulation of plasmonic nanoparticles and their application for surface-enhanced infrared spectroscopy.

Ksenia Weber is a M.Sc. candidate in the research group of Professor Harald Giessen at the 4th Physics Institute at the University of Stuttgart. Her main research interests include surface-enhanced infrared spectroscopy and direct laser writing lithography.

Annemarie Pucci, with a Ph.D. in theoretical physics, became associate professor for experimental physics at the Heidelberg University in 1995. Her research is dedicated to studies of excitations of surface, nanostructures, and thin layers in the infrared energy range. She was the first who explained SEIRA as a Fano-type effect related to plasmonic excitations.

Harald Giessen is full professor since 2005 and holds the Chair for Ultrafast Nano optics in the Department of Physics at the University of Stuttgart. He is also cochair of the Stuttgart Center of Photonics Engineering, SCoPE. He received an ERC Advanced Grant in 2012 for his work on complex nanoplasmatics. He is on the advisory board of the journals "Advanced Optical Materials", "Nanophotonics: The Journal", and "ACS Photonics". He is a topical editor for ultrafast nano optics, plasmonics, and ultrafast lasers and pulse generation of the journal "Light: Science & Applications" of the Nature Publishing Group. He is a Fellow of the Optical Society of America. His research interests include Ultrafast Nano-Optics, Plasmonics, Metamaterials, 3D Printed Micro- and Nano-Optics, Novel mid-IR Ultrafast Laser Sources, Applications in Microscopy, Biology, and Sensing.

## ACKNOWLEDGMENTS

We thank Nikolai Strohfeldt for the TOC and figure artwork. F.N., K.W., and H.G. gratefully acknowledge financial support by the ERC (Advanced Grant COMPLEXPLAS), BMBF, GIF, DFG, Alexander von Humboldt-Stiftung, Carl-Zeiss-Stiftung, and the Baden-Württemberg Stiftung (PROTEINSENS). C.H. and A.P. acknowledge funding by the DFG (DFG Pu 193/9).

## REFERENCES

- (1) Meier, R. In *Handbook of Vibrational Spectroscopy*; Chalmers, J., Griffiths, P. R., Eds.; John Wiley & Sons Ltd.: Chichester, UK, 2003.
- (2) Stuart, B. H. *Spectral Analysis*; John Wiley & Sons Ltd.: Chichester, UK, 2005.
- (3) Bakulin, A.; Lovrincic, R.; Yu, X.; Selig, O.; Bakker, H. J.; Rezus, Y. L. a.; Nayak, P. K.; Fonari, A.; Coropceanu, V.; Brédas, J.-L.; et al. Mode-Selective Vibrational Modulation of Charge Transport in Organic Electronic Devices. *Nat. Commun.* **2015**, *6*, 7880.
- (4) Keller, L. P.; Bajt, S.; Baratta, G. A.; Borg, J.; Bradley, J. P.; Brownlee, D. E.; Busemann, H.; Brucato, J. R.; Burchell, M.; Colangeli, L. Infrared Spectroscopy of Comet 81P/Wild 2 Samples Returned by Stardust. *Science* **2006**, *314*, 1728–1731.
- (5) Ragai, J. The Scientific Detection of Forgery in Paintings. *Proc. Am. Philos. Soc.* **2013**, *157*, 164–175.
- (6) Petibois, C.; Délier, G. Chemical Mapping of Tumor Progression by FT-IR Imaging: Towards Molecular Histopathology. *Trends Biotechnol.* **2016**, *24*, 455–462.
- (7) Barth, A. Infrared Spectroscopy of Proteins. *Biochim. Biophys. Acta, Bioenerg.* **2007**, *1767*, 1073–1101.
- (8) Maier, S. A. *Plasmonics: Fundamentals and Applications*; Springer Science & Business Media: New York, 2007.
- (9) Schmidt, F.-P.; Ditzbacher, H.; Hohenester, U.; Hohenau, A.; Hofer, F.; Krenn, J. R. Universal Dispersion of Surface Plasmons in Flat Nanostructures. *Nat. Commun.* **2014**, *5*, 3604.
- (10) Schlücker, S. Surface-Enhanced Raman Spectroscopy: Concepts and Chemical Applications. *Angew. Chem., Int. Ed.* **2014**, *53*, 4756–4795.
- (11) Bauch, M.; Toma, K.; Toma, M.; Zhang, Q.; Dostalek, J. Plasmon-Enhanced Fluorescence Biosensors: A Review. *Plasmonics* **2014**, *9*, 781–799.
- (12) Hartstein, A.; Kirtley, J. R.; Tsang, J. C. Enhancement of the Infrared Absorption from Molecular Monolayers with Thin Metal Overlays. *Phys. Rev. Lett.* **1980**, *45*, 201–204.
- (13) Osawa, M. Surface-Enhanced Infrared Absorption. In *Near-Field Optics and Surface Plasmon Polaritons*; Kawata, S., Ed.; Springer Berlin Heidelberg: Heidelberg, DE, 2001.
- (14) Aroca, R. F.; Ross, D. J.; Domingo, C. Surface-Enhanced Infrared Spectroscopy. *Appl. Spectrosc.* **2004**, *58*, 9325–9330.
- (15) Neubrech, F.; Pucci, A.; Cornelius, T. W.; Karim, S.; Garcia-Etxarri, A.; Aizpurua, J. Resonant Plasmonic and Vibrational Coupling in a Tailored Nanoantenna for Infrared Detection. *Phys. Rev. Lett.* **2008**, *101*, 157403.
- (16) Chen, C. K.; Chang, M. H.; Wu, H. T.; Lee, Y. C.; Yen, T. J. Enhanced Vibrational Spectroscopy, Intracellular Refractive Indexing for Label-Free Biosensing and Bioimaging by Multiband Plasmonic-Antenna Array. *Biosens. Bioelectron.* **2014**, *60*, 343–350.
- (17) Kühner, L.; Hentschel, M.; Zschieschang, U.; Klauk, H.; Vogt, J.; Huck, C.; Giessen, H.; Neubrech, F. Nanoantenna-Enhanced Hyperspectral Infrared Chemical Imaging, submitted.
- (18) Dregely, D.; Neubrech, F.; Duan, H.; Vogelgesang, R.; Giessen, H. Vibrational near-Field Mapping of Planar and Buried Three-Dimensional Plasmonic Nanostructures. *Nat. Commun.* **2013**, *4*, 2237.
- (19) Vogt, J.; Zimmermann, S.; Huck, C.; Tzschoppe, M.; Neubrech, F.; Fatikow, S.; Pucci, A. Chemical Identification of Individual Fine Dust Particles with Resonant Plasmonic Enhancement of Nanoslits in the Infrared. *ACS Photonics* **2017**, *4*, 560.
- (20) Bochterle, J.; Neubrech, F.; Nagao, T.; Pucci, A. Ångström-Scale Distance Dependence of Antenna-Enhanced Vibrational Signals. *ACS Nano* **2012**, *6*, 10917–10923.

- (21) Limaj, O.; Etezadi, D.; Wittenberg, N. J.; Rodrigo, D.; Yoo, D.; Oh, S. H.; Altug, H. Infrared Plasmonic Biosensor for Real-Time and Label-Free Monitoring of Lipid Membranes. *Nano Lett.* **2016**, *16*, 1502–1508.
- (22) Adato, R.; Altug, H. In-Situ Ultra-Sensitive Infrared Absorption Spectroscopy of Biomolecule Interactions in Real Time with Plasmonic Nanoantennas. *Nat. Commun.* **2013**, *4*, 2154.
- (23) Weis, P.; Garcia-Pomar, J. L.; Beigang, R.; Rahm, M. Hybridization Induced Transparency in Composites of Metamaterials and Atomic Media. *Opt. Express* **2011**, *19*, 23573–23580.
- (24) Toma, A.; Tuccio, S.; Prato, M.; De Donato, F.; Perucchi, A.; Di Pietro, P.; Marras, S.; Liberale, C.; Zaccaria, R. P.; De Angelis, F.; et al. Squeezing Terahertz Light into Nanovolumes: Nanoantenna Enhanced Terahertz Spectroscopy (NETS) of Semiconductor Quantum Dots. *Nano Lett.* **2015**, *15*, 386–391.
- (25) Park, H.-R.; Ahn, K. J.; Han, S.; Bahk, Y.-M.; Park, N.; Kim, D.-S. Colossal Absorption of Molecules Inside Single Terahertz Nanoantennas. *Nano Lett.* **2013**, *13*, 1782–1786.
- (26) Jensen, T. R.; Van Duyne, R. P.; Johnson, S. A.; Maroni, V. A. Surface-Enhanced Infrared Spectroscopy: A Comparison of Metal Island Films with Discrete and Nondiscrete Surface Plasmons. *Appl. Spectrosc.* **2000**, *54*, 371–377.
- (27) Anderson, M. S. Enhanced Infrared Absorption with Dielectric Nanoparticles. *Appl. Phys. Lett.* **2003**, *83*, 2964–2966.
- (28) Anderson, M. S. Surface Enhanced Infrared Absorption by Coupling Phonon and Plasma Resonance. *Appl. Phys. Lett.* **2005**, *87*, 144102.
- (29) Kundu, J.; Le, F.; Nordlander, P.; Halas, N. J. Surface Enhanced Infrared Absorption (SEIRA) Spectroscopy on Nanoshell Aggregate Substrates. *Chem. Phys. Lett.* **2008**, *452*, 115–119.
- (30) Lal, S.; Grady, N. K.; Kundu, J.; Levin, C. S.; Lassiter, J. B.; Halas, N. J. Tailoring Plasmonic Substrates for Surface Enhanced Spectroscopies. *Chem. Soc. Rev.* **2008**, *37*, 898–911.
- (31) Le, F.; Brandl, D. W.; Urzhumov, Y. A.; Wang, H.; Kundu, J.; Halas, N. J.; Aizpurua, J.; Nordlander, P. Metallic Nanoparticle Arrays: A Common Substrate for Both Surface-Enhanced Raman Scattering and Surface-Enhanced Infrared Absorption. *ACS Nano* **2008**, *2*, 707–718.
- (32) Aroca, R.; Price, B. A New Surface for Surface-Enhanced Infrared Spectroscopy: Tin Island Films. *J. Phys. Chem. B* **1997**, *101*, 6537–6540.
- (33) Albrecht, M. G.; Creighton, J. A. Anomalously Intense Raman Spectra of Pyridine at a Silver Electrode. *J. Am. Chem. Soc.* **1977**, *99*, 5215–5217.
- (34) Jeanmaire, D. L.; Van Duyne, R. P. Surface Raman Spectroelectrochemistry: Part I. Heterocyclic, Aromatic, and Aliphatic Amines Adsorbed on the Anodized Silver Electrode. *J. Electroanal. Chem. Interfacial Electrochem.* **1977**, *84*, 1–20.
- (35) Bradshaw, A. M.; Pritchard, J. Infrared Spectra of Carbon Monoxide Chemisorbed on Metal Films: A Comparative Study of Copper, Silver, Gold, Iron, Cobalt and Nickel. *Proceedings of the Royal Society of London A: Mathematical, Physical and Engineering Sciences*; The Royal Society: UK, 1970; Vol. 316, pp 169–183.
- (36) Fasasi, A.; Griffiths, P. R.; Scudiero, L. Surface-Enhanced Infrared Absorption (SEIRA) of Adsorbates on Copper Nanoparticles Synthesized by Galvanic Displacement. *Appl. Spectrosc.* **2011**, *65*, 750–755.
- (37) Nishikawa, Y.; Nagasawa, T.; Fujiwara, K.; Osawa, M. Silver Island Films for Surface-Enhanced Infrared Absorption Spectroscopy: Effect of Island Morphology on the Absorption Enhancement. *Vib. Spectrosc.* **1993**, *6*, 43–53.
- (38) Osawa, M. Dynamic Processes in Electrochemical Reactions Studied by Surface-Enhanced Infrared Absorption Spectroscopy (SEIRAS). *Bull. Chem. Soc. Jpn.* **1997**, *70*, 2861–2880.
- (39) Verger, F.; Pain, T.; Nazabal, V.; Boussard-Plédel, C.; Bureau, B.; Colas, F.; Rinnert, E.; Boukerma, K.; Compère, C.; Guilloux-Viry, M.; et al. Surface Enhanced Infrared Absorption (SEIRA) Spectroscopy Using Gold Nanoparticles on As<sub>2</sub>S<sub>3</sub> Glass. *Sens. Actuators, B* **2012**, *175*, 142–148.
- (40) Yang, J.; Griffiths, P. R. Preparation and Characterization by Surface-Enhanced Infrared Absorption Spectroscopy of Silver Nanoparticles Formed on Germanium Substrates by Electroless Displacement. *Anal. Bioanal. Chem.* **2007**, *388*, 109–119.
- (41) Wanzenböck, H. D.; Mizaikoff, B.; Weissenbacher, N.; Kellner, R. Multiple Internal Reflection in Surface Enhanced Infrared Absorption Spectroscopy (SEIRA) and Its Significance for Various Analyte Groups. *J. Mol. Struct.* **1997**, *410*, 535–538.
- (42) Miki, A.; Ye, S.; Osawa, M. Surface-Enhanced IR Absorption on Platinum Nanoparticles: An Application to Real-Time Monitoring of Electrocatalytic Reactions. *Chem. Commun.* **2002**, *14*, 1500–1501.
- (43) Osawa, M.; Ikeda, M. Surface-Enhanced Infrared Absorption of P-Nitrobenzoic Acid Deposited on Silver Island Films: Contributions of Electromagnetic and Chemical Mechanisms. *J. Phys. Chem.* **1991**, *95*, 9914–9919.
- (44) Bjerke, A. E.; Griffiths, P. R.; Theiss, W. Surface-Enhanced Infrared Absorption of CO on Platinized Platinum. *Anal. Chem.* **1999**, *71*, 1967–1974.
- (45) Zheng, M.-S.; Sun, S.-G.; Chen, S.-P. Abnormal Infrared Effects and Electrocatalytic Properties of Nanometer Scale Thin Film of PtRu Alloys for CO Adsorption and Oxidation. *J. Appl. Electrochem.* **2001**, *31*, 749–757.
- (46) Hahn, F.; Melendres, C. Anodic Oxidation of Methane at Noble Metal Electrodes: An “in Situ” Surface Enhanced Infrared Spectroelectrochemical Study. *Electrochim. Acta* **2001**, *46*, 3525–3534.
- (47) Priebe, A.; Sinther, M.; Fahsold, G.; Pucci, A. The Correlation between Film Thickness and Adsorbate Line Shape in Surface Enhanced Infrared Absorption. *J. Chem. Phys.* **2003**, *119*, 4887–4890.
- (48) Priebe, A.; Fahsold, G.; Pucci, A. Strong Pyramidal Growth of Metal Films Studied with IR Transmittance and Surface Enhanced IR Absorption of CO. *J. Phys. Chem. B* **2004**, *108*, 18174–18178.
- (49) Ross, D.; Aroca, R. Effective Medium Theories in Surface Enhanced Infrared Spectroscopy: The Pentacene Example. *J. Chem. Phys.* **2002**, *117*, 8095–8103.
- (50) Abelès, F. *Optical Properties of Solids*; North-Holland Publ. Co.: New York, 1972.
- (51) Silin, V. I.; Voronov, S. A.; Yakovlev, V. A.; Zhizhin, G. N. IR Surface Plasmon (Polariton) Phase Spectroscopy. *Int. J. Infrared Millimeter Waves* **1989**, *10*, 101–120.
- (52) Sernelius, B. E. *Surface Modes in Physics*; John Wiley & Sons: Chichester, UK, 2011.
- (53) Osawa, M. Surface-Enhanced Infrared Absorption. *Top. Appl. Phys.* **2001**, *81*, 163–187.
- (54) Lovrinčić, R.; Pucci, A. Infrared Optical Properties of Chromium Nanoscale Films with a Phase Transition. *Phys. Rev. B: Condens. Matter Mater. Phys.* **2009**, *80*, 205404.
- (55) Pucci, A.; Kost, F.; Fahsold, G.; Jalochowski, M. Infrared Spectroscopy of Pb Layer Growth on Si(111). *Phys. Rev. B: Condens. Matter Mater. Phys.* **2006**, *74*, 125428.
- (56) Fahsold, G.; Bartel, A.; Krauth, O.; Magg, N.; Pucci, A. Infrared Optical Properties of Ultrathin Fe Films on MgO(001) beyond the Percolation Threshold. *Phys. Rev. B: Condens. Matter Mater. Phys.* **2000**, *61*, 14108–14113.
- (57) Meng, F.; Pucci, A. Growth of Silver on MgO(001) and Infrared Optical Properties. *Phys. Status Solidi B* **2007**, *244*, 3739–3749.
- (58) Lovrinčić, R.; Noebel, S.; Pucci, A. Infrared Monitoring of Diamond Metalization. *Appl. Spectrosc.* **2011**, *65*, 105–107.
- (59) Priebe, A. Oberflächenverstärkte Infrarotabsorption von CO Auf Ultradünnen Metallfilmen. Ph.D. Thesis, Heidelberg University, 2002.
- (60) Fahsold, G.; Pucci, A.; Rieder, K.-H. Growth of Fe on MgO(001) Studied by He-Atom Scattering. *Phys. Rev. B: Condens. Matter Mater. Phys.* **2000**, *61*, 8475–8483.
- (61) Berthier, S.; Peiro, J. Anomalous Infra-Red Absorption of Nanocermets in the Percolation Range. *J. Phys.: Condens. Matter* **1998**, *10*, 3679–3694.
- (62) Chettiar, U. K.; Nyga, P.; Thoreson, M. D.; Kildishev, A. V.; Drachev, V. P.; Shalaev, V. M. FDTD Modeling of Realistic Semicontinuous Metal Films. *Appl. Phys. B: Lasers Opt.* **2010**, *100*, 159–168.

- (63) Neuman, T.; Huck, C.; Vogt, J.; Neubrech, F.; Hillenbrand, R.; Aizpurua, J.; Pucci, A. Importance of Plasmonic Scattering for an Optimal Enhancement of Vibrational Absorption in SEIRA with Linear Metallic Antennas. *J. Phys. Chem. C* **2015**, *119*, 26652–26662.
- (64) Enders, D.; Nagao, T.; Pucci, A.; Nakayama, T.; Aono, M. Surface-Enhanced ATR-IR Spectroscopy with Interface-Grown Plasmonic Gold-Island Films near the Percolation Threshold. *Phys. Chem. Chem. Phys.* **2011**, *13*, 4935–4941.
- (65) Wang, H.; Kundu, J.; Halas, N. J. Plasmonic Nanoshell Arrays Combine Surface-Enhanced Vibrational Spectroscopies on a Single Substrate. *Angew. Chem., Int. Ed.* **2007**, *46*, 9040–9044.
- (66) Halas, N. J.; Lal, S.; Chang, W. S.; Link, S.; Nordlander, P. Plasmons in Strongly Coupled Metallic Nanostructures. *Chem. Rev.* **2011**, *111*, 3913–3961.
- (67) Zhang, Y.; Manjavacas, A.; Hogan, N. J.; Zhou, L.; Ayala-Orozco, C.; Dong, L.; Day, J. K.; Nordlander, P.; Halas, N. J. Toward Surface Plasmon-Enhanced Optical Parametric Amplification (SPOPA) with Engineered Nanoparticles: A Nanoscale Tunable Infrared Source. *Nano Lett.* **2016**, *16*, 3373–3378.
- (68) Kocer, H.; Butun, S.; Banar, B.; Wang, K.; Tongay, S.; Wu, J.; Aydin, K. Thermal Tuning of Infrared Resonant Absorbers Based on Hybrid Gold-VO<sub>2</sub> Nanostructures. *Appl. Phys. Lett.* **2015**, *106*, 161104.
- (69) Hatta, A.; Ohshima, T.; Suētaka, W. Observation of the Enhanced Infrared Absorption of P-Nitrobenzoate on Ag Island Films with an ATR Technique. *Appl. Phys. A: Solids Surf.* **1982**, *29*, 71–75.
- (70) Ataka, K.; Stripp, S. T.; Heberle, J. Surface-Enhanced Infrared Absorption Spectroscopy (SEIRAS) to Probe Monolayers of Membrane Proteins. *Biochim. Biophys. Acta, Biomembr.* **2013**, *1828*, 2283–2293.
- (71) Schwaighofer, A.; Steininger, C.; Hildenbrandt, D. M.; Srajer, J.; Nowak, C.; Knoll, W.; Naumann, R. L. C. Time-Resolved Surface-Enhanced IR-Absorption Spectroscopy of Direct Electron Transfer to Cytochrome c Oxidase from *R. Sphaeroides*. *Biophys. J.* **2013**, *105*, 2706–2713.
- (72) Hoang, C. V.; Oyama, M.; Saito, O.; Aono, M.; Nagao, T. Monitoring the Presence of Ionic Mercury in Environmental Water by Plasmon-Enhanced Infrared Spectroscopy. *Sci. Rep.* **2013**, *3*, 1175.
- (73) Goutev, N.; Futamata, M. A. Attenuated Total Reflection Surface-Enhanced Infrared Absorption Spectroscopy of Carboxyl Terminated Self-Assembled Monolayers on Gold. *Appl. Spectrosc.* **2003**, *57*, 506–513.
- (74) Wandlowski, T.; Ataka, K.; Pronkin, S.; Diesing, D. Surface Enhanced Infrared Spectroscopy - Au(111–20nm)/sulphuric Acid - New Aspects and Challenges. *Electrochim. Acta* **2004**, *49*, 1233–1247.
- (75) Skibbe, O.; Binder, M.; Otto, A.; Pucci, A. Electronic Contributions to Infrared Spectra of Adsorbate Molecules on Metal Surfaces: Ethene on Cu(111). *J. Chem. Phys.* **2008**, *128*, 194703.
- (76) Sinther, M.; Pucci, A.; Otto, A.; Priebe, A.; Diez, S.; Fahsold, G. Enhanced Infrared Absorption of SERS-Active Lines of Ethylene on Cu. *Phys. status solidi* **2001**, *188*, 1471–1476.
- (77) Wadayama, T.; Takada, M.; Sugiyama, K.; Hatta, A. Infrared Absorption Enhancement of C<sub>60</sub> on Silver Islands: Contribution of Charge Transfer and Collective Electron Resonance. *Phys. Rev. B: Condens. Matter Mater. Phys.* **2002**, *66*, 193401.
- (78) Panek, J. J.; Jezierska-Mazzarello, A.; Koll, A.; Dovbeshko, G.; Fesenko, O. P-Nitrobenzoic Acid Adsorption on Nanostructured Gold Surfaces Investigated by Combined Experimental and Computational Approaches. *ChemPhysChem* **2011**, *12*, 2485–2495.
- (79) Langreth, D. C. Energy Transfer at Surfaces: Asymmetric Line Shapes and the Electron-Hole-Pair Mechanism. *Phys. Rev. Lett.* **1985**, *54*, 126–129.
- (80) Hein, M.; Dumas, P.; Sinther, M.; Priebe, A.; Lilie, P.; Bruckbauer, A.; Pucci, A.; Otto, A. Relation between Surface Resistance, Infrared-, Surface Enhanced Infrared- and Surface Enhanced Raman-Spectroscopy's of C<sub>2</sub>H<sub>4</sub> and CO on Copper. *Surf. Sci.* **2006**, *600*, 1017–1025.
- (81) Priebe, A.; Pucci, A.; Otto, A. Infrared Reflection–Absorption Spectra of C<sub>2</sub>H<sub>4</sub> and C<sub>2</sub>H<sub>6</sub> on Cu: Effect of Surface Roughness. *J. Phys. Chem. B* **2006**, *110*, 1673–1679.
- (82) Klinkova, A.; Choueiri, R. M.; Kumacheva, E. Self-Assembled Plasmonic Nanostructures. *Chem. Soc. Rev.* **2014**, *43*, 3976–3991.
- (83) Adato, R.; Yanik, A. A.; Amsden, J. J.; Kaplan, D. L.; Omenetto, F. G.; Hong, M. K.; Erramilli, S.; Altug, H. Ultra-Sensitive Vibrational Spectroscopy of Protein Monolayers with Plasmonic Nanoantenna Arrays. *Proc. Natl. Acad. Sci. U. S. A.* **2009**, *106*, 19227–19232.
- (84) Bagheri, S.; Weber, K.; Gissibl, T.; Weiss, T.; Neubrech, F.; Giessen, H. Fabrication of Square-Centimeter Plasmonic Nanoantenna Arrays by Femtosecond Direct Laser Writing Lithography: Effects of Collective Excitations on SEIRA Enhancement. *ACS Photonics* **2015**, *2*, 779–786.
- (85) Cataldo, S.; Zhao, J.; Neubrech, F.; Frank, B.; Zhang, C.; Braun, P. V.; Giessen, H. Hole-Mask Colloidal Nanolithography for Large-Area Low-Cost Metamaterials and Antenna-Assisted Surface-Enhanced Infrared Absorption Substrates. *ACS Nano* **2012**, *6*, 979–985.
- (86) Bagheri, S.; Giessen, H.; Neubrech, F. Large-Area Antenna-Assisted SEIRA Substrates by Laser Interference Lithography. *Adv. Opt. Mater.* **2014**, *2*, 1050–1056.
- (87) Aksu, S.; Cetin, A. E.; Adato, R.; Altug, H. Plasmonically Enhanced Vibrational Biospectroscopy Using Low-Cost Infrared Antenna Arrays by Nanostencil Lithography. *Adv. Opt. Mater.* **2013**, *1*, 798–803.
- (88) Aksu, S.; Yanik, A. A.; Adato, R.; Artar, A.; Huang, M.; Altug, H. High-Throughput Nanofabrication of Infrared Plasmonic Nanoantenna Arrays for Vibrational Nanospectroscopy. *Nano Lett.* **2010**, *10*, 2511–2518.
- (89) Schubert, I.; Huck, C.; Kröber, P.; Neubrech, F.; Pucci, A.; Toimil-Molares, M. E.; Trautmann, C.; Vogt, J. Porous Gold Nanowires: Plasmonic Response and Surface-Enhanced Infrared Absorption. *Adv. Opt. Mater.* **2016**, *4*, 1838–1845.
- (90) Neubrech, F.; Kolb, T.; Lovrincic, R.; Fahsold, G.; Pucci, A.; Aizpurua, J.; Cornelius, T. W.; Toimil-Molares, M. E.; Neumann, R.; Karim, S. Resonances of Individual Metal Nanowires in the Infrared. *Appl. Phys. Lett.* **2006**, *89*, 253104.
- (91) Hoffmann, J. M.; Janssen, H.; Chigrin, D. N.; Taubner, T. Enhanced Infrared Spectroscopy Using Small-Gap Antennas Prepared with Two-Step Evaporation Nanosphere Lithography. *Opt. Express* **2014**, *22*, 14425–14432.
- (92) Hoffmann, J. M.; Yin, X.; Richter, J.; Hartung, A.; Maß, T. W. W.; Taubner, T. Low-Cost Infrared Resonant Structures for Surface-Enhanced Infrared Absorption Spectroscopy in the Fingerprint Region from 3 to 13 μm. *J. Phys. Chem. C* **2013**, *117*, 11311–11316.
- (93) Chang, Y.-C.; Lu, S.-C.; Chung, H.-C.; Wang, S.-M.; Tsai, T.-D.; Guo, T.-F. High-Throughput Nanofabrication of Infra-Red and Chiral Metamaterials Using Nanospherical-Lens Lithography. *Sci. Rep.* **2013**, *3*, 3339.
- (94) Wang, T.; Nguyen, V. H.; Buchenauer, A.; Schnakenberg, U.; Taubner, T. Surface Enhanced Infrared Spectroscopy with Gold Strip Gratings. *Opt. Express* **2013**, *21*, 9005–9010.
- (95) Huck, C.; Neubrech, F.; Vogt, J.; Toma, A.; Gerbert, D.; Katzmann, J.; Härtling, T.; Pucci, A. Surface-Enhanced Infrared Spectroscopy Using Nanometer-Sized Gaps. *ACS Nano* **2014**, *8*, 4908–4914.
- (96) Crozier, K. B.; Sundaramurthy, A.; Kino, G. S.; Quate, C. F. Optical Antennas: Resonators for Local Field Enhancement. *J. Appl. Phys.* **2003**, *94*, 4632–4642.
- (97) Novotny, L. Effective Wavelength Scaling for Optical Antennas. *Phys. Rev. Lett.* **2007**, *98*, 266802.
- (98) Sönnichsen, C.; Franzl, T.; Wilk, T.; von Plessen, G.; Feldmann, J.; Wilson, O.; Mulvaney, P. Drastic Reduction of Plasmon Damping in Gold Nanorods. *Phys. Rev. Lett.* **2002**, *88*, 77402.
- (99) Neubrech, F.; Weber, D.; Lovrincic, R.; Pucci, A.; Lopes, M.; Touy, T.; De La Chapelle, M. L. Resonances of Individual Lithographic Gold Nanowires in the Infrared. *Appl. Phys. Lett.* **2008**, *93*, 4–6.
- (100) Neuman, T.; Alonso-González, P.; García-Etxarri, A.; Schnell, M.; Hillenbrand, R.; Aizpurua, J. Mapping the near Fields of Plasmonic Nanoantennas by Scattering-Type Scanning near-Field Optical Microscopy. *Laser Photonics Rev.* **2015**, *9*, 637–649.

- (101) Neubrech, F.; Beck, S.; Glaser, T.; Hentschel, M.; Giessen, H.; Pucci, A. Spatial Extent of Plasmonic Enhancement of Vibrational Signals in the Infrared. *ACS Nano* **2014**, *8*, 6250–6258.
- (102) Aizpurua, J.; Bryant, G. W.; Richter, L. J.; Garcia de Abajo, F. J.; Kelley, B. K.; Mallouk, T. Optical Properties of Coupled Metallic Nanorods for Field-Enhanced Spectroscopy. *Phys. Rev. B: Condens. Matter Mater. Phys.* **2005**, *71*, 235420.
- (103) Olmon, R. L.; Krenz, P. M.; Jones, A. C.; Boreman, G. D.; Raschke, M. B. Near-Field Imaging of Optical Antenna Modes in the Mid-Infrared. *Opt. Express* **2008**, *16*, 20295–20305.
- (104) Alonso-González, P.; Albella, P.; Neubrech, F.; Huck, C.; Chen, J.; Golmar, F.; Casanova, F.; Hueso, L. E.; Pucci, A.; Aizpurua, J.; et al. Experimental Verification of the Spectral Shift between Near- and Far-Field Peak Intensities of Plasmonic Infrared Nanoantennas. *Phys. Rev. Lett.* **2013**, *110*, 203902.
- (105) Ament, I.; Prasad, J.; Henkel, A.; Schmachtel, S.; Sönnichsen, C. Single Unlabeled Protein Detection on Individual Plasmonic Nanoparticles. *Nano Lett.* **2012**, *12*, 1092–1095.
- (106) Zuloaga, J.; Prodan, E.; Nordlander, P. Quantum Plasmonics: Optical Properties and Tunability of Metallic Nanorods. *ACS Nano* **2010**, *4*, 5269–5276.
- (107) Neubrech, F.; Garcia-Etxarri, A.; Weber, D.; Bochterle, J.; Shen, H.; de la Chapelle, M. L.; Bryant, G. W.; Aizpurua, J.; Pucci, A. Defect-Induced Activation of Symmetry Forbidden Infrared Resonances in Individual Metallic Nanorods. *Appl. Phys. Lett.* **2010**, *96*, 17–19.
- (108) Adato, R.; Aksu, S.; Altug, H. Engineering Mid-Infrared Nanoantennas for Surface Enhanced Infrared Absorption Spectroscopy. *Mater. Today* **2015**, *18*, 436–446.
- (109) Giannini, V.; Francescato, Y.; Amrani, H.; Phillips, C. C.; Maier, S. A. Fano Resonances in Nanoscale Plasmonic Systems: A Parameter-Free Modeling Approach. *Nano Lett.* **2011**, *11*, 2835–2840.
- (110) Osley, E. J.; Biris, C. G.; Thompson, P. G.; Jahromi, R. R. F.; Warburton, P. A.; Panouli, N. C. Fano Resonance Resulting from a Tunable Interaction between Molecular Vibrational Modes and a Double Continuum of a Plasmonic Metamolecule. *Phys. Rev. Lett.* **2013**, *110*, 1–5.
- (111) Vogt, J.; Huck, C.; Neubrech, F.; Toma, A.; Gerbert, D.; Pucci, A. Impact of the Plasmonic Near- and Far-Field Resonance-Energy Shift on the Enhancement of Infrared Vibrational Signals. *Phys. Chem. Chem. Phys.* **2015**, *17*, 21169–21175.
- (112) Gallinet, B.; Martin, O. J. F. Ab Initio Theory of Fano Resonances in Plasmonic Nanostructures and Metamaterials. *Phys. Rev. B: Condens. Matter Mater. Phys.* **2011**, *83*, 1–6.
- (113) Rezus, Y. L. A.; Selig, O. Impact of Local-Field Effects on the Plasmonic Enhancement of Vibrational Signals by Infrared Nanoantennas. *Opt. Express* **2016**, *24*, 12202–12227.
- (114) Eilers, P. H. C. A Perfect Smoother. *Anal. Chem.* **2003**, *75*, 3631–3636.
- (115) Fano, U. Effects of Configuration Interaction on Intensities and Phase Shifts. *Phys. Rev.* **1961**, *124*, 1866–1878.
- (116) Luk'yanchuk, B.; Zheludev, N. I.; Maier, S. A.; Halas, N. J.; Nordlander, P.; Giessen, H.; Chong, C. T. The Fano Resonance in Plasmonic Nanostructures and Metamaterials. *Nat. Mater.* **2010**, *9*, 707–715.
- (117) Miroshnichenko, A. E.; Flach, S.; Kivshar, Y. S. Fano Resonances in Nanoscale Structures. *Rev. Mod. Phys.* **2010**, *82*, 2257–2298.
- (118) Adato, R.; Artar, A.; Erramilli, S.; Altug, H. Engineered Absorption Enhancement and Induced Transparency in Coupled Molecular and Plasmonic Resonator Systems. *Nano Lett.* **2013**, *13*, 2584–2591.
- (119) Fan, S.; Suh, W.; Joannopoulos, J. D. Temporal Coupled-Mode Theory for the Fano Resonance in Optical Resonators. *J. Opt. Soc. Am. A* **2003**, *20*, 569–572.
- (120) Verslegers, L.; Yu, Z.; Catrysse, P. B.; Fan, S. Temporal Coupled-Mode Theory for Resonant Apertures. *J. Opt. Soc. Am. B* **2010**, *27*, 1947–1956.
- (121) Verslegers, L.; Yu, Z.; Ruan, Z.; Catrysse, P. B.; Fan, S. From Electromagnetically Induced Transparency to Superscattering with a Single Structure: A Coupled-Mode Theory for Doubly Resonant Structures. *Phys. Rev. Lett.* **2012**, *108*, 1–5.
- (122) Haus, H. *Waves and Fields in Optoelectronics*; Prentice-Hall: Englewood Cliffs, NJ, 1985.
- (123) Taubert, R.; Hentschel, M.; Kästel, J.; Giessen, H. Classical Analog of Electromagnetically Induced Absorption in Plasmonics. *Nano Lett.* **2012**, *12*, 1367–1371.
- (124) Moskovits, M. Surface-Enhanced Spectroscopy. *Rev. Mod. Phys.* **1985**, *57*, 783–826.
- (125) Le Ru, E. C.; Etchegoin, P. G. Rigorous Justification of the  $|E|^4$  Enhancement Factor in Surface Enhanced Raman Spectroscopy. *Chem. Phys. Lett.* **2006**, *423*, 63–66.
- (126) Brown, L. V.; Zhao, K.; King, N. S.; Sobhani, H.; Nordlander, P.; Halas, N. J. Surface-Enhanced Infrared Absorption Using Individual Cross Antennas Tailored to Chemical Moieties. *J. Am. Chem. Soc.* **2013**, *135*, 3688–3695.
- (127) Cubukcu, E.; Zhang, S.; Park, Y.-S.; Bartal, G.; Zhang, X. Split Ring Resonator Sensors for Infrared Detection of Single Molecular Monolayers. *Appl. Phys. Lett.* **2009**, *95*, 43113.
- (128) Aouani, H.; Šípová, H.; Rahmani, M.; Navarro-Cia, M.; Hegnerová, K.; Homola, J.; Hong, M.; Maier, S. A. Ultrasensitive Broadband Probing of Molecular Vibrational Modes with Multi-frequency Optical Antennas. *ACS Nano* **2012**, *7*, 669–675.
- (129) De Ninno, A.; Ciasca, G.; Gerardino, A.; Calandri, E.; Papi, M.; Spirito, M.; De Nucara, A.; Ortolani, M.; Businaro, L.; Baldassare, L. An Integrated Superhydrophobic-Plasmonic Biosensor for Mid-Infrared Protein Detection at the Femtomole Level. *Phys. Chem. Chem. Phys.* **2015**, *17*, 21337–21342.
- (130) D'Andrea, C.; Bochterle, J.; Toma, A.; Huck, C.; Neubrech, F.; Messina, E.; Fazio, B.; Marag, O. M.; Di Fabrizio, E.; de la Chapelle, M. L.; et al. Optical Nanoantennas for Multiband Surface-Enhanced Infrared and Raman Spectroscopy. *ACS Nano* **2013**, *7*, 3522–3531.
- (131) Pryce, I. M.; Kelaita, Y. A.; Aydin, K.; Atwater, H. A. Compliant Metamaterials for Resonantly Enhanced Infrared Absorption Spectroscopy and Refractive Index Sensing. *ACS Nano* **2011**, *5*, 8167–8174.
- (132) Bukasov, R.; Ali, T. A.; Nordlander, P.; Shumaker-Parry, J. S. Probing the Plasmonic Near-Field of Gold Nanocrescent Antennas. *ACS Nano* **2010**, *4*, 6639–6650.
- (133) Sandu, T. Near-Field and Extinction Spectra of Rod-Shaped Nanoantenna Dimers. *Proceedings of the Romanian Academy, Series A*; **2014**; Vol. 15, p 338–345.
- (134) Weber, K.; Nesterov, M. L.; Weiss, T.; Scherer, M.; Hentschel, M.; Vogt, J.; Huck, C.; Li, W.; Dressel, M.; Giessen, H.; et al. Wavelength Scaling in Antenna-Enhanced Infrared Spectroscopy: Toward the Far-IR and THz Region. *ACS Photonics* **2017**, *4*, 45–51.
- (135) Orfanidis, S. J. *Electromagnetic Waves and Antennas*; Rutgers University: New Brunswick, NJ, 2003.
- (136) Balanis, C. A. *Antenna Theory: Analysis and Design*; John Wiley & Sons: Chichester, UK, 2016.
- (137) Adato, R.; Yanik, A. A.; Altug, H. On Chip Plasmonic Monopole Nano-Antennas and Circuits. *Nano Lett.* **2011**, *11*, 5219–5226.
- (138) Wan, W.; Yang, X.; Gao, J. Strong Coupling between Mid-Infrared Localized Plasmons and Phonons. *Opt. Express* **2016**, *24*, 12367.
- (139) Bukasov, R.; Shumaker-Parry, J. S. Silver Nanocrescents with Infrared Plasmonic Properties as Tunable Substrates for Surface Enhanced Infrared Absorption Spectroscopy. *Anal. Chem.* **2009**, *81*, 4531–4535.
- (140) Lahiri, B.; Holland, G.; Aksyuk, V.; Centrone, A. Nanoscale Imaging of Plasmonic Hot Spots and Dark Modes with the Photothermal-Induced Resonance Technique. *Nano Lett.* **2013**, *13*, 3218–3224.
- (141) Paul, J.; De La Rue, R. M.; Johnson, N. P. Gold Asymmetric-Split Ring Resonators (A-SRRs) for Proteins Sensing. *Proceedings of the*

- SPIE; SPIE Phototonics Europe: Metamaterials X: Brussels, Belgium, 2016.
- (142) Chae, J.; Lahiri, B.; Kohoutek, J.; Holland, G.; Lezec, H.; Centrone, A. Metal-Dielectric-Metal Resonators with Deep Subwavelength Dielectric Layers Increase the near-Field SEIRA Enhancement. *Opt. Express* **2015**, *23*, 25912–25922.
- (143) Hulteen, J. C.; Treichel, D. A.; Smith, M. T.; Duval, M. L.; Jensen, T. R.; van Duyne, R. P. Nanosphere Lithography: Size Tunable Silver Nanoparticle and Surface Cluster Arrays. *J. Phys. Chem. B* **1999**, *103*, 3854–3863.
- (144) Fischer, U. C. Submicroscopic Pattern Replication with Visible Light. *J. Vac. Sci. Technol.* **1981**, *19*, 881–885.
- (145) Shumaker-Parry, J. S.; Rochholz, H.; Kreiter, M. Fabrication of Crescent-Shaped Optical Antennas. *Adv. Mater.* **2005**, *17*, 2131–2134.
- (146) Ra'di, Y.; Simovski, C. R.; Tretyakov, S. A. Thin Perfect Absorbers for Electromagnetic Waves: Theory, Design, and Realizations. *Phys. Rev. Appl.* **2015**, *3*, 37001.
- (147) Chen, K.; Adato, R.; Altug, H. Dual-Band Perfect Absorber for Infrared Spectroscopy. *ACS Nano* **2012**, *6*, 7998–8006.
- (148) Li, Y.; Su, L.; Shou, C.; Yu, C.; Deng, J.; Fang, Y. Surface-Enhanced Molecular Spectroscopy (SEMS) Based on Perfect-Absorber Metamaterials in the Mid-Infrared. *Sci. Rep.* **2013**, *3*, 2865.
- (149) Srayer, J.; Schwaighofer, A.; Ramer, G.; Rotter, S.; Guenay, B.; Kriegner, A.; Knoll, W.; Lendl, B.; Nowak, C. Double-Layered Nanoparticle Stacks for Surface Enhanced Infrared Absorption Spectroscopy. *Nanoscale* **2014**, *6*, 127–131.
- (150) Brown, L. V.; Yang, X.; Zhao, K.; Zheng, B. Y.; Nordlander, P.; Halas, N. J. Fan-Shaped Gold Nanoantennas above Reflective Substrates for Surface-Enhanced Infrared Absorption (SEIRA). *Nano Lett.* **2015**, *15*, 1272–1280.
- (151) Huck, C.; Vogt, J.; Sendner, M.; Hengstler, D.; Neubrech, F.; Pucci, A. Plasmonic Enhancement of Infrared Vibrational Signals: Nanoslits versus Nanorods. *ACS Photonics* **2015**, *2*, 1489–1497.
- (152) Cetin, A. E.; Etezadi, D.; Altug, H. Accessible Nearfields by Nanoantennas on Nanopedestals for Ultrasensitive Vibrational Spectroscopy. *Adv. Opt. Mater.* **2014**, *2*, 866–872.
- (153) Hentschel, M.; Weiss, T.; Bagheri, S.; Giessen, H. Babinet to the Half: Coupling of Solid and Inverse Plasmonic Structures. *Nano Lett.* **2013**, *13*, 4428–4433.
- (154) Liu, N.; Weiss, T.; Mesch, M.; Langguth, L.; Eigenthaler, U.; Hirscher, M.; Sönnichsen, C.; Giessen, H. Planar Metamaterial Analogue of Electromagnetically Induced Transparency for Plasmonic Sensing. *Nano Lett.* **2010**, *10*, 1103–1107.
- (155) Yang, H. U.; Olmon, R. L.; Deryckx, K. S.; Xu, X. G.; Bechtel, H. A.; Xu, Y.; Lail, B. A.; Raschke, M. B. Accessing the Optical Magnetic Near-Field through Babinet's Principle. *ACS Photonics* **2014**, *1*, 894–899.
- (156) Ögüt, B.; Vogelgesang, R.; Sigle, W.; Talebi, N.; Koch, C. T.; Van Aken, P. A. Hybridized Metal Slit Eigenmodes as an Illustration of Babinet's Principle. *ACS Nano* **2011**, *5*, 6701–6706.
- (157) Kim, M. K.; Sim, H.; Yoon, S. J.; Gong, S. H.; Ahn, C. W.; Cho, Y. H.; Lee, Y. H. Squeezing Photons into a Point-Like Space. *Nano Lett.* **2015**, *15*, 4102–4107.
- (158) Cetin, A. E.; Aksu, S.; Turkmen, M.; Etezadi, D.; Altug, H. Theoretical and Experimental Analysis of Subwavelength Bowtie-Shaped Antennas. *J. Electromagn. Waves Appl.* **2015**, *29*, 1686–1698.
- (159) Cetin, A. E.; Kaya, S.; Mertiri, A.; Aslan, E.; Erramilli, S.; Altug, H.; Turkmen, M. Dual-Band Plasmonic Resonator Based on Jerusalem Cross-Shaped Nanoapertures. *Photonics Nanostructures - Fundam. Appl.* **2014**, *15*, 73–80.
- (160) Mayerhöfer, T. G.; Knipper, R.; Hübner, U.; Cialla-May, D.; Weber, K.; Meyer, H. G.; Popp, J. Ultra Sensing by Combining Extraordinary Optical Transmission with Perfect Absorption. *ACS Photonics* **2015**, *2*, 1567–1575.
- (161) Muller, E. A.; Pollard, B.; Bechtel, H. A.; Adato, R.; Yang, H. U.; Martin, M. C.; Altug, H.; Raschke, M. B. Infrared Vibrational Molecular Hybridization with a Single Optical Antenna. *Lasers and Electro-Optics (CLEO), 2015 Conference; IEEE, 2015*; pp 1–2.
- (162) Ordal, M. A.; Long, L. L.; Bell, R. J.; Bell, S. E.; Bell, R. R.; Alexander, R. W.; Ward, C. A. Optical Properties of the Metals Al, Co, Cu, Au, Fe, Pb, Ni, Pd, Pt, Ag, Ti, and W in the Infrared and Far Infrared. *Appl. Opt.* **1983**, *22*, 1099–1119.
- (163) Cerjan, B.; Yang, X.; Nordlander, P.; Halas, N. J. Asymmetric Aluminum Antennas for Self-Calibrating Surface-Enhanced Infrared Absorption Spectroscopy. *ACS Photonics* **2016**, *3*, 354–360.
- (164) Abb, M.; Wang, Y.; Papasimakis, N.; de Groot, C. H.; Muskens, O. L. Surface-Enhanced Infrared Spectroscopy Using Metal Oxide Plasmonic Antenna Arrays. *Nano Lett.* **2014**, *14*, 346–352.
- (165) Li, Y.; Yan, H.; Farmer, D. B.; Meng, X.; Osgood, R. M.; Heinz, T. F.; Avouris, P. Graphene Plasmon Enhanced Vibrational Sensing of Surface- Adsorbed Layers Graphene Plasmon Enhanced Vibrational Sensing of Surface- Adsorbed Layers. *Nano Lett.* **2014**, *14*, 1573–1577.
- (166) Law, S.; Podolskiy, V.; Wasserman, D. Towards Nano-Scale Photonics with Micro-Scale Photons: The Opportunities and Challenges of Mid-Infrared Plasmonics. *Nanophotonics* **2013**, *2*, 103–130.
- (167) Kalusniak, S.; Sadofev, S.; Schäfer, P.; Henneberger, F. Heavily N-Type ZnO: A Plasmonic Material at Telecommunication Wavelengths. *Phys. status solidi* **2014**, *11*, 1357–1360.
- (168) Baldassarre, L.; Sakat, E.; Frigerio, J.; Samarelli, A.; Gallacher, K.; Calandrini, E.; Isella, G.; Paul, D. J.; Ortolani, M.; Biagioni, P. Midinfrared Plasmon-Enhanced Spectroscopy with Germanium Antennas on Silicon Substrates. *Nano Lett.* **2015**, *15*, 7225–7231.
- (169) Giannini, V.; Berrier, A.; Maier, S. a; Sánchez-Gil, J. A.; Rivas, J. G. Scattering Efficiency and near Field Enhancement of Active Semiconductor Plasmonic Antennas at Terahertz Frequencies. *Opt. Express* **2010**, *18*, 2797–2807.
- (170) Marini, A.; Silveiro, I.; García de Abajo, F. J. Molecular Sensing with Tunable Graphene Plasmons. *ACS Photonics* **2015**, *2*, 876–882.
- (171) Rodrigo, D.; Limaj, O.; Janner, D.; Etezadi, D.; Garcia de Abajo, F. J.; Pruneri, V.; Altug, H. Mid-Infrared Plasmonic Biosensing with Graphene. *Science* **2015**, *349*, 165–168.
- (172) Luxmoore, I. J.; Liu, P. Q.; Li, P.; Nash, G. R. Graphene-Metamaterial Photodetectors for Integrated Infrared Sensing. *ACS Photonics* **2016**, *3*, 936–941.
- (173) Chabal, Y. J. Surface Infrared Spectroscopy. *Surf. Sci. Rep.* **1988**, *8*, 211–357.
- (174) Gagner, J. E.; Lopez, M. D.; Dordick, J. S.; Siegel, R. W. Effect of Gold Nanoparticle Morphology on Adsorbed Protein Structure and Function. *Biomaterials* **2011**, *32*, 7241–7252.
- (175) Iwasa, T.; Takenaka, M.; Taketsugu, T. Generalized Theoretical Method for the Interaction between Arbitrary Nonuniform Electric Field and Molecular Vibrations: Toward near-Field Infrared Spectroscopy and Microscopy. *J. Chem. Phys.* **2016**, *144*, 124116.
- (176) Alber, I.; Sigle, W.; Müller, S.; Neumann, R.; Picht, O.; Rauber, M.; Van Aken, P. A.; Toimil-Molares, M. E. Visualization of Multipolar Longitudinal and Transversal Surface Plasmon Modes in Nanowire Dimers. *ACS Nano* **2011**, *5*, 9845–9853.
- (177) Prats-Alfonso, E.; Albericio, F. Functionalization of Gold Surfaces: Recent Developments and Applications. *J. Mater. Sci.* **2011**, *46*, 7643–7648.
- (178) Neubrech, F.; Weber, D.; Katzmüller, J.; Huck, C.; Toma, A.; Di Fabrizio, E.; Pucci, A.; Härtling, T. Infrared Optical Properties of Nanoantenna Dimers with Photochemically Narrowed Gaps in the Smm Regime. *ACS Nano* **2012**, *6*, 7326–7332.
- (179) Chen, X.; Ciraci, C.; Smith, D. R.; Oh, S. H. Nanogap-Enhanced Infrared Spectroscopy with Template-Stripped Wafer-Scale Arrays of Buried Plasmonic Cavities. *Nano Lett.* **2015**, *15*, 107–113.
- (180) Adato, R.; Yanik, A. A.; Wu, C.-H.; Shvets, G.; Altug, H. Radiative Engineering of Plasmon Lifetimes in Embedded Nanoantenna Arrays. *Opt. Express* **2010**, *18*, 4526–4537.
- (181) Giannini, V.; Vecchi, G.; Gómez Rivas, J. Lighting up Multipolar Surface Plasmon Polaritons by Collective Resonances in Arrays of Nanoantennas. *Phys. Rev. Lett.* **2010**, *105*, 266801.
- (182) Weber, D.; Albella, P.; Alonso-González, P.; Neubrech, F.; Gui, H.; Nagao, T.; Hillenbrand, R.; Aizpurua, J.; Pucci, A. Longitudinal and

- Transverse Coupling in Infrared Gold Nanoantenna Arrays: Long Range versus Short Range Interaction Regimes. *Opt. Express* **2011**, *19*, 15047–15061.
- (183) De Marcellis, A.; Palange, E.; Janneh, M.; Rizza, C.; Ciattoni, A.; Mengali, S. Design Optimisation of Plasmonic Metasurfaces for Mid-Infrared High-Sensitivity Chemical Sensing. *Plasmonics* **2017**, *12*, 1–6.
- (184) Maß, T. W. W.; Taubner, T. Incident Angle-Tuning of Infrared Antenna Array Resonances for Molecular Sensing. *ACS Photonics* **2015**, *2*, 1498–1504.
- (185) Ishikawa, A.; Tanaka, T. Metamaterial Absorbers for Infrared Detection of Molecular Self-Assembled Monolayers. *Sci. Rep.* **2015**, *5*, 12570.
- (186) Coe, J. V.; Rodriguez, K. R.; Teeters-Kennedy, S.; Cilwa, K.; Heer, J.; Tian, H.; Williams, S. M. Metal Films with Arrays of Tiny Holes: Spectroscopy with Infrared Plasmonic Scaffolding. *J. Phys. Chem. C* **2007**, *111*, 17459–17472.
- (187) Liberman, V.; Adato, R.; Jeys, T. H.; Saar, B. G.; Erramilli, S.; Altug, H. Rational Design and Optimization of Plasmonic Nanoarrays for Surface Enhanced Infrared Spectroscopy. *Opt. Express* **2012**, *20*, 11953–11966.
- (188) Chen, J.; Badioli, M.; Alonso-González, P.; Thongrattanasiri, S.; Huth, F.; Osmond, J.; Spasenović, M.; Centeno, A.; Pesquera, A.; Godignon, P.; et al. Optical Nano-Imaging of Gate-Tunable Graphene Plasmons. *Nature* **2012**, *487*, 77–81.
- (189) Cetin, A. E.; Turkmen, M.; Aksu, S.; Etezadi, D.; Altug, H. Multi-Resonant Compact Nanoaperture with Accessible Large Near-fields. *Appl. Phys. B: Lasers Opt.* **2015**, *118*, 29–38.
- (190) Navarro-Cia, M.; Maier, S. A. Broad-Band near-Infrared Plasmonic Nanoantennas for Higher Harmonic Generation. *ACS Nano* **2012**, *6*, 3537–3544.
- (191) Pryce, I. M.; Aydin, K.; Kelaita, Y. A.; Briggs, R. M.; Atwater, H. A. Highly Strained Compliant Optical Metamaterials with Large Frequency Tunability. *Nano Lett.* **2010**, *10*, 4222–4227.
- (192) Kats, M. A.; Blanchard, R.; Genevet, P.; Yang, Z.; Qazilbash, M. M.; Basov, D. N.; Ramanathan, S.; Capasso, F. Thermal Tuning of Mid-Infrared Plasmonic Antenna Arrays Using a Phase Change Material. *Opt. Lett.* **2013**, *38*, 368–370.
- (193) Michel, A.-K. U.; Chigrin, D. N.; Maß, T. W. W.; Schönauer, K.; Salanga, M.; Wuttig, M.; Taubner, T. Using Low-Loss Phase-Change Materials for Mid-Infrared Antenna Resonance Tuning. *Nano Lett.* **2013**, *13*, 3470–3475.
- (194) Michel, A.-K. U.; Zalden, P.; Chigrin, D. N.; Wuttig, M.; Lindenberg, A. M.; Taubner, T. Reversible Optical Switching of Infrared Antenna Resonances with Ultrathin Phase-Change Layers Using Femtosecond Laser Pulses. *ACS Photonics* **2014**, *1*, 833–839.
- (195) Tittl, A.; Michel, A. K. U.; Schäferling, M.; Yin, X.; Gholipour, B.; Cui, L.; Wuttig, M.; Taubner, T.; Neubrech, F.; Giessen, H. A Switchable Mid-Infrared Plasmonic Perfect Absorber with Multispectral Thermal Imaging Capability. *Adv. Mater.* **2015**, *27*, 4597–4603.
- (196) Griffiths, P. R.; De Haseth, J. A. *Fourier Transform Infrared Spectrometry*; John Wiley & Sons: Chichester, UK, 2007.
- (197) Petibois, C.; Délérès, G.; Piccinini, M.; Cestelli-Guidi, M.; Marcelli, A. A Bright Future for Synchrotron Imaging. *Nat. Photonics* **2009**, *3*, 179–179.
- (198) Yao, Y.; Hoffman, A. J.; Gmachl, C. F. Mid-Infrared Quantum Cascade Lasers. *Nat. Photonics* **2012**, *6*, 432–439.
- (199) Mörz, F.; Steinle, T.; Steinmann, A.; Giessen, H. Multi-Watt Femtosecond Optical Parametric Master Oscillator Power Amplifier at 43 MHz. *Opt. Express* **2015**, *23*, 23960–23967.
- (200) Muller, E. A.; Pollard, B.; Bechtel, H. A.; Adato, R.; Yang, H. U.; Martin, M. C.; Altug, H.; Raschke, M. B. Infrared Vibrational Molecular Hybridization with a Single Optical Antenna. *CLEO - Conference on Lasers and Electro-Optics*; 2015.
- (201) Bechtel, H. A.; Muller, E. A.; Olmon, R. L.; Martin, M. C.; Raschke, M. B. Ultrabroadband Infrared Nanospectroscopic Imaging. *Proc. Natl. Acad. Sci. U. S. A.* **2014**, *111*, 7191–7196.
- (202) Pechenezhskiy, I. V.; Hong, X.; Nguyen, G. D.; Dahl, J. E. P.; Carlson, R. M. K.; Wang, F.; Crommie, M. F. Infrared Spectroscopy of Molecular Submonolayers on Surfaces by Infrared Scanning Tunneling Microscopy: Tetramantane on Au(111). *Phys. Rev. Lett.* **2013**, *111*, 126101.
- (203) Steinle, T.; Neubrech, F.; Steinmann, A.; Yin, X.; Giessen, H. Mid-Infrared Fourier-Transform Spectroscopy with a High-Brilliance Tunable Laser Source: Investigating Sample Areas down to 5 μm Diameter. *Opt. Express* **2015**, *23*, 11105–11113.
- (204) Huth, F.; Chuvalin, A.; Schnell, M.; Amenabar, I.; Krutokhrostov, R.; Lopatin, S.; Hillenbrand, R. Resonant Antenna Probes for Tip-Enhanced Infrared near-Field Microscopy. *Nano Lett.* **2013**, *13*, 1065–1072.
- (205) Hasenkampf, A.; Kröger, N.; Schönhals, A.; Petrich, W.; Pucci, A. Surface-Enhanced Mid-Infrared Spectroscopy Using a Quantum Cascade Laser. *Opt. Express* **2015**, *23*, 5670–5680.
- (206) Amenabar, I.; Poly, S.; Nuansing, W.; Hubrich, E. H.; Goyadinov, A. A.; Huth, F.; Krutokhrostov, R.; Zhang, L.; Knez, M.; Heberle, J.; et al. Structural Analysis and Mapping of Individual Protein Complexes by Infrared Nanospectroscopy. *Nat. Commun.* **2013**, *4*, 2890.
- (207) Muller, E. A.; Pollard, B.; Raschke, M. B. Infrared Chemical Nano-Imaging: Accessing Structure, Coupling, and Dynamics on Molecular Length Scales. *J. Phys. Chem. Lett.* **2015**, *6*, 1275–1284.
- (208) Hoffmann, J. M.; Hauer, B.; Taubner, T. Antenna-Enhanced Infrared near-Field Nanospectroscopy of a Polymer. *Appl. Phys. Lett.* **2012**, *101*, 193105.
- (209) Alonso-González, P.; Albella, P.; Schnell, M.; Chen, J.; Huth, F.; García-Etxarri, A.; Casanova, F.; Golmar, F.; Arzubiaga, L.; Hueso, L. E.; et al. Resolving the Electromagnetic Mechanism of Surface-Enhanced Light Scattering at Single Hot Spots. *Nat. Commun.* **2012**, *3*, 684.
- (210) De Angelis, F.; Gentile, F.; Mecarini, F.; Das, G.; Moretti, M.; Candeloro, P.; Coluccio, M. L.; Cojoc, G.; Accardo, A.; Liberale, C.; et al. Breaking the Diffusion Limit with Super-Hydrophobic Delivery of Molecules to Plasmonic Nanofocusing SERS Structures. *Nat. Photonics* **2011**, *5*, 682–687.
- (211) Xu, X. G.; Rang, M.; Craig, I. M.; Raschke, M. B. Pushing the Sample-Size Limit of Infrared Vibrational Nanospectroscopy: From Monolayer toward Single Molecule Sensitivity. *J. Phys. Chem. Lett.* **2012**, *3*, 1836–1841.
- (212) Hermanna, P.; Patoka, P.; Huth, F.; Rtihl, E.; Virna, G.; Universität, F. Near-Field Imaging and Nano-Fourier-Transform Infrared Spectroscopy Using Broadband Synchrotron Radiation. *Opt. Express* **2013**, *21*, 2913–2919.
- (213) Neubrech, F.; Weber, D.; Enders, D.; Nagao, T.; Pucci, A. Antenna Sensing of Surface Phonon Polaritons. *J. Phys. Chem. C* **2010**, *114*, 7299–7301.
- (214) Huck, C.; Vogt, J.; Neuman, T.; Nagao, T.; Hillenbrand, R.; Aizpurua, J.; Pucci, A.; Neubrech, F. Strong Coupling between Phonon-Polaritons and Plasmonic Nanorods. *Opt. Express* **2016**, *24*, 23573–23580.
- (215) Shelton, D. J.; Brener, I.; Ginn, J. C.; Sinclair, M. B.; Peters, D. W.; Coffey, K. R.; Boreman, G. D. Strong Coupling between Nanoscale Metamaterials and Phonons. *Nano Lett.* **2011**, *11*, 2104–2108.
- (216) Krutokhrostov, R.; Goyadinov, A.; Stiegler, J. M.; Huth, F.; Chuvalin, A.; Carney, P. S.; Hillenbrand, R. Enhanced Resolution in Subsurface Near-Field Optical Microscopy. *Opt. Express* **2012**, *20*, 593–600.
- (217) Goyadinov, A. A.; Mastel, S.; Golmar, F.; Chuvalin, A.; Carney, P. S.; Hillenbrand, R. Recovery of Permittivity and Depth from Near-Field Data as a Step toward Infrared Nanotomography. *ACS Nano* **2014**, *8*, 6911–6921.
- (218) Nishimura, Y.; Kawano, T.; Kunichika, Y.; Kasahara, K.; Yaji, T.; Ikeda, N.; Oosato, H. Observation of the Enhancement of Electric Fields Normal to the Surface Using Mid-Infrared Slot Antennas and an Atomic Layer Deposition Technique Au/Ti ALD-Made. *Opt. Commun.* **2015**, *349*, 98–104.

- (219) Liu, N.; Langguth, L.; Weiss, T.; Kästel, J.; Fleischhauer, M.; Pfau, T.; Giessen, H. Plasmonic EIT at the Drude Damping Limit. *Conf. Proc. - Lasers Electro-Optics Soc. Annu. Meet.* **2009**, *8*, 94–95.
- (220) Gowen, A. A.; O'Donnell, C.; Cullen, P. J.; Downey, G.; Frias, J. M. Hyperspectral Imaging—an Emerging Process Analytical Tool for Food Quality and Safety Control. *Trends Food Sci. Technol.* **2007**, *18*, 590–598.
- (221) Griffiths, P. R. *Infrared and Raman Instrumentation for Mapping and Imaging*; Wiley-VCH Verlag GmbH & Co. KGaA: Weinheim, DE, 2009.
- (222) Diem, M.; Romeo, M.; Boydston-White, S.; Miljković, M.; Matthäus, C. A Decade of Vibrational Micro-Spectroscopy of Human Cells and Tissue (1994–2004). *Analyst* **2004**, *129*, 880–885.
- (223) Childs, D. T. D.; Hogg, R. A.; Revin, D. G.; Rehman, I. U.; Cockburn, J. W.; Matcher, S. J. Sensitivity Advantage of QCL Tunable-Laser Mid-Infrared Spectroscopy Over FTIR Spectroscopy. *Appl. Spectrosc. Rev.* **2015**, *50*, 822–839.
- (224) Yeh, K.; Kenkel, S.; Liu, J. N.; Bhargava, R. Fast Infrared Chemical Imaging with a Quantum Cascade Laser. *Anal. Chem.* **2015**, *87*, 485–493.
- (225) Bassan, P.; Weida, M. J.; Rowlette, J.; Gardner, P. Large Scale Infrared Imaging of Tissue Micro Arrays (TMAs) Using a Tunable Quantum Cascade Laser (QCL) Based Microscope. *Analyst* **2014**, *139*, 3856–3859.
- (226) Fry, M. *Essential Biochemistry for Medicine*; John Wiley & Sons, Ltd: Chichester, UK, 2011.
- (227) Chen, K.; Dao, T. D.; Ishii, S.; Aono, M.; Nagao, T. Infrared Aluminum Metamaterial Perfect Absorbers for Plasmon-Enhanced Infrared Spectroscopy. *Adv. Funct. Mater.* **2015**, *25*, 6637–6643.
- (228) Alici, K. B. Hybridization of Fano and Vibrational Resonances in Surface-Enhanced Infrared Absorption Spectroscopy of Streptavidin Monolayers on Metamaterial Substrates. *IEEE Trans. Nanotechnol.* **2014**, *13*, 216–221.
- (229) Alici, K. B.; Gallardo, I. F. Detecting Secondary Structure and Surface Orientation of Helical Peptide Monolayers from Resonant Hybridization Signals. *Sci. Rep.* **2013**, *3*, 2956.
- (230) Wu, C.; Khanikaev, A. B.; Adato, R.; Arju, N.; Yanik, A. A.; Altug, H.; Shvets, G. Fano-Resonant Asymmetric Metamaterials for Ultrasensitive Spectroscopy and Identification of Molecular Monolayers. *Nat. Mater.* **2011**, *11*, 69–75.
- (231) Underwood, S.; Mulvaney, P. Effect of the Solution Refractive Index on the Color of Gold Colloids. *Langmuir* **1994**, *10*, 3427–3430.
- (232) Dong, Z. G.; Liu, H.; Cao, J. X.; Li, T.; Wang, S. M.; Zhu, S. N.; Zhang, X. Enhanced Sensing Performance by the Plasmonic Analog of Electromagnetically Induced Transparency in Active Metamaterials. *Appl. Phys. Lett.* **2010**, *97*, 114101.
- (233) Shih, W.-C.; Santos, G. M.; Zhao, F.; Zenasni, O.; Arnob, M. M. P. Simultaneous Chemical and Refractive Index Sensing in 1–2.5 $\mu$ m Near-Infrared Wavelength Range on Nanoporous Gold Disks. *Nano Lett.* **2016**, *16*, 4641–4647.
- (234) Christ, A.; Ekinci, Y.; Solak, H. H.; Gippius, N. A.; Tikhodeev, S. G.; Martin, O. J. F. Controlling the Fano Interference in a Plasmonic Lattice. *Phys. Rev. B: Condens. Matter Mater. Phys.* **2007**, *76*, 201405.
- (235) Zhang, S.; Genov, D. A.; Wang, Y.; Liu, M.; Zhang, X. Plasmon-Induced Transparency in Metamaterials. *Phys. Rev. Lett.* **2008**, *101*, 47401.
- (236) Papasimakis, N.; Fedotov, V. A.; Zheludev, N. I.; Prosvirnin, S. L. Metamaterial Analog of Electromagnetically Induced Transparency. *Phys. Rev. Lett.* **2008**, *101*, 253903.
- (237) Cheng, F.; Yang, X.; Gao, J. Ultrasensitive Detection and Characterization of Molecules with Infrared Plasmonic Metamaterials. *Sci. Rep.* **2015**, *5*, 14327.
- (238) Allen, J. A.; Halverson-Tamboli, R. A.; Rasenick, M. Lipid Raft Microdomains and Neurotransmitter Signalling. *Nat. Rev. Neurosci.* **2007**, *8*, 128–140.